Jet Energy Measurements with the ZEUS Prototype Calorimeter

by

W. Kröger

Jet Energy Measurements with the ZEUS Prototype Calorimeter

DISSERTATION

zur Erlangung des Doktorgrades
des Fachbereichs Physik
der Universität Hamburg

vorgelegt von
Wilko Kröger
aus Hamburg

Hamburg
1993

Gutachter der Dissertation	Prof. Dr. E. Lohrmann
	Prof. Dr. P. Schmüser
Gutachter der Disputation	Prof. Dr. E. Lohrmann
	Prof. Dr. B. Naroska
Datum der Disputation	19.01.1993

Sprecher des
Fachbereichs Physik und
Vorsitzender des
Promotionsausschusses: Prof. Dr. G. Mack

Abstract

The uranium scintillator calorimeter of the ZEUS detector is designed to achieve an excellent energy calibration and the best possible energy resolution for jets. Therefore the response of the prototype calorimeter to jets has been measured using an interaction trigger. The mean response and energy resolution was measured for jets of 50 GeV - 100 GeV and compared to the one for pions.

Within the ZEUS detector dead material is placed in front of the calorimeter. The influence of 4 cm and 10 cm thick aluminum absorbers in front of the calorimeter was measured. The charged multiplicity was measured in front and behind the aluminum absorber. With these multiplicities the energy loss in the absorber is corrected. The correction has been done so that the mean response with absorber is equal to the mean response without absorber. The improvement of the energy resolution is investigated. The measured results are compared with Monte Carlo simulations.

Zusammenfassung

Das Uran-Szintillator Kalorimeter des ZEUS-Detektors ist auf eine exzellente Energieeichung und die beste mögliche Energieauflösung für Jets ausgelegt worden. Deshalb wurde das Verhalten des Prototype Kalorimeters für Jets mit einem Wechselwirkungstrigger untersucht. Die mittlere Antwort und die Energieauflösung wurde für 50 GeV - 100 GeV Jets gemessen und diese Ergebnisse werden mit denen für Pionen verglichen.

Im ZEUS-Detektor befindet sich totes Material vor dem Kalorimeter. Deshalb wurde der Einfluß von 4 cm und 10 cm Aluminiumplatten auf die Energieeichung und Energieauflösung untersucht. Die geladenen Multiplizitäten wurden vor und hinter den Aluminiumplatten gemessen und der Energieverlust wird mit diesen Multiplizitäten korrigiert. Die Korrekturen werden so durchgeführt, daß die mittlere Kalorimeterantwort mit Aluminium genau so groß ist wie die ohne Aluminium. Die Verbesserung der Energieauflösung durch Korrekturen wird untersucht. Monte Carlo Simulationen wurden durchgeführt und mit den experimentellen Ergebnissen verglichen.

Contents

List of Figures

List of Tables

Chapter 1

Introduction

Since April 1992 the first electron-proton collisions have been observed at the HERA collider, located at DESY in Hamburg. The HERA collider [14,16,22] consists of two rings: one for electrons with a beam energy of 30 GeV, and one for protons with a beam energy of 820 GeV. The center of mass energy is 314 GeV and hence one order of magnitude larger than the highest c.m. energies achieved at present-day lepton-hadron experiments. The momentum transfer possible in an electron-proton interaction ($Q^2_{max} \approx 10^5$ GeV^2) makes HERA first and foremost an electron-quark collider.

The physical potential of HERA is quite impressive. It ranges from testing the sector of strong interaction physics (proton structure function, QCD test) and electroweak physics to "exotic" physics like the substructure of leptons and quarks, new weak vector bosons, excited leptons and SUSY theories. A detailed description of the physics possibilities can be found in [15,16,19].

In lowest order the interaction of an electron and proton is described by the exchange of a γ or Z^0 for neutral current (NC) events and a $W^\pm$ for charged current (CC) events. For NC events the scattered lepton is an electron and for CC events a neutrino. On the proton side jets emerge from the interaction. For a single vector boson exchange two jets are created: the current jet from the struck quark and the target jet from the proton remnant. The overall event kinematics are described by the kinematical variables (e.g. momentum transfer Q^2, Bjorken x, y).

In order to exploit the physics potential of HERA it is essential to get a good reconstruction of the kinematical variables [8]. The differential cross section can be measured by the event rates in bins of the $Q^2 - x$ plane. However the observed event rate in a given bin is not the true event rate. Due to measurement errors a fraction of the events migrates out of the bin while another fraction migrates into this bin from adjacent bins. By this migrations the event rate in a given bin can change significantly, leading to potential errors in the measurement.

The accessible range in the $Q^2 - x$ plane where the differential cross section can be safely measured is defined by that range where the migration is less than 10 %. If the measurement of the variables is more precise the accessible range increases [4,8,17].

Other physical processes are detected by a peak in the distribution of a variable e.g. Leptoquarks show up by a peak in the x-distribution. This requires a precise measurement of x in order to get a well separated signal from the background. Also it has to be ensured that this peak is not due to some peculiarity of the x measurement.

The kinematical variables are calculated from the calorimeter measurement of the scattered electron (for NC events) or from the measurement of the final hadronic system (necessary for CC events). Therefore their range and precision depends on the calorimeter per-

1

formance. In various studies the effect of the energy measurement on the determination of the differential cross section has been investigated. Depending on the $Q^2 - x$ region which is considered different schemes for the reconstruction have been proposed [4]. It has been shown that the best results can be achieved when the information of the scattered electron is combined with the information of the final hadronic system. For CC events, of course, the reconstruction can only be done from the hadronic system and it is important to understand the response of the calorimeter to jets. Three main questions are:

- How does the energy calibration changes for jets compared to single hadrons, is the calorimeter response linear?

- Does the energy resolution change?

- Is the energy distribution for jets still gaussian, as for single particles, or do tails exist?

For the ZEUS detector one has to achieve an absolute energy calibration of about 1 %. This requires a very good understanding of the calorimeter response to jets. In particular the contribution of low energy hadronic particles ($E < 5GeV$) to the energy signal is important because the calorimeter response is not linear for these particles [2,10,21].

A crucial rule for the understanding are the tails of the calorimeter response that occur in the energy distribution for monoenergetic particles or jets.

An important effect which is strongly connected with the energy measurement of the calorimeter is the influence of passive material in front of the calorimeter. In the ZEUS detector the inner tracking chambers and the solenoid are surrounded by the calorimeter. A particle on its way to the calorimeter may interact in the passive material in front of the calorimeter and a fraction of its initial energy is lost. This energy loss results in a systematic shift of the measured energy and also deteriorates the energy resolution. Therefore it is important that the energy loss in the passive material is well known and correctly described in the detector simulation. In beam tests the influence of passive material on the energy calibration and energy resolution has been measured [10,18].

In order to study these problems, a prototype of the ZEUS forward calorimeter [1,20] has been constructed. It followed close to the design of the final calorimeter modules except for the reduced height. In testbeam experiments the calorimeter response to electrons and pions with an energy from 0.5 - 100 GeV was extensively tested. The detailed results of these test are summarized in [2,3].

As already mentioned above in ep-scattering the calorimeter measures jets and not a single particle. Therefore an interaction trigger was designed to test the prototype calorimeter response to jets.

With this interaction trigger setup the calorimeter response was measured for different jet energies (50 GeV - 100 GeV) and the results are compared with the response of single pions.

Aluminum absorbers of different thickness were placed in front of the calorimeter and the effect of the energy calibration and energy resolution was investigated. The charged multiplicity was measured in front of the aluminum absorber and also behind. The possibilities to correct for the energy that is lost in the aluminum is also investigated.

In the first chapter the experimental setup is described. In the second chapter the experimental results are discussed. The experimental test setup was simulated by a Monte Carlo. In the third chapter the results from the simulation and from the experiment are compared.

In addition properties of the jets e.g. energy spectrum, particle composition are shown. The last chapter summarizes the results.

Chapter 2

Experimental Setup

2.1   The Calorimeter

2.1.1   Mechanical Construction

The prototype calorimeter consisted of four identical modules. They were constructed as prototype modules for the ZEUS forward calorimeter [1,20,23] following the same mechanical design as the final modules, except for a reduced height. Each module consisted of four 20 × 20 cm^2 towers and was segmented longitudinally into an electromagnetic part (EMC, $1\lambda^1$ thick) and two hadronic sections (HAC1 and HAC2, each 3λ thick). The EMC part was further segmented into four 5 × 20 cm^2 sections in the transverse direction. A view of the calorimeter is shown in fig.2.1.

The sandwich structure of the calorimeter consisted of 3.3 mm thick depleted uranium plates (DU) interleaved with 2.6 mm thick scintillator tiles (SCI) of the SCSN-38 type. The DU plates were clad with 0.2 and 0.4 mm of stainless steel in the EMC and HAC sections respectively. The SCI tiles were wrapped in Tyvek paper with a printed black pattern, to achieve a good readout uniformity. The first EMC layer was an aluminum plate, 15 mm thick, followed by a SCI plate and 25 DU-SCI layers. After DU plates 3 and 6 a 10 mm deep gap was instrumented with arrays of 10 cm^2 silicon diode detectors in order to improve the electron-hadron separation. Each of the two HAC sections consisted of 80 DU-SCI layers. The total thickness of a DU-SCI layer was 7.6 mm in the EMC and 8.0 mm in the HAC. In order to avoid any pressure on the scintillator, the DU plates were kept at distance by tungsten-carbide spacers located at the corners of the 20×20 cm^2 towers. Their cross-section was 5×6 mm^2 in the EMC and 5×10 mm^2 in the HAC.

Each section was read out on the left and right side by wave length shifter plates (WLS), light guides (LG) and photomultipliers (PMT). The WLS plates were 2 mm thick and consisted of PMMA doped with Y7 in a concentration of 45 ppm or 30 ppm for EMC or HAC sections, respectively. The uniformity of the WLS response was achieved with end and back reflectors. The PMTs were of the type XP2972 and XP2081 from Valvo for EMC and HAC sections respectively. A view of a tower is shown in fig.2.2.

These four modules formed a calorimeter of 80×80 cm^2 cross-section and 7λ thickness (see fig.2.1). Between module 2 and module 3 a 3 mm thick lead foil was placed. The main calorimeter parameters are summarized in table 2.1. More details about the mechanical structure of the calorimeter can be found in [3].

---

[1] λ is the effective nuclear interaction length
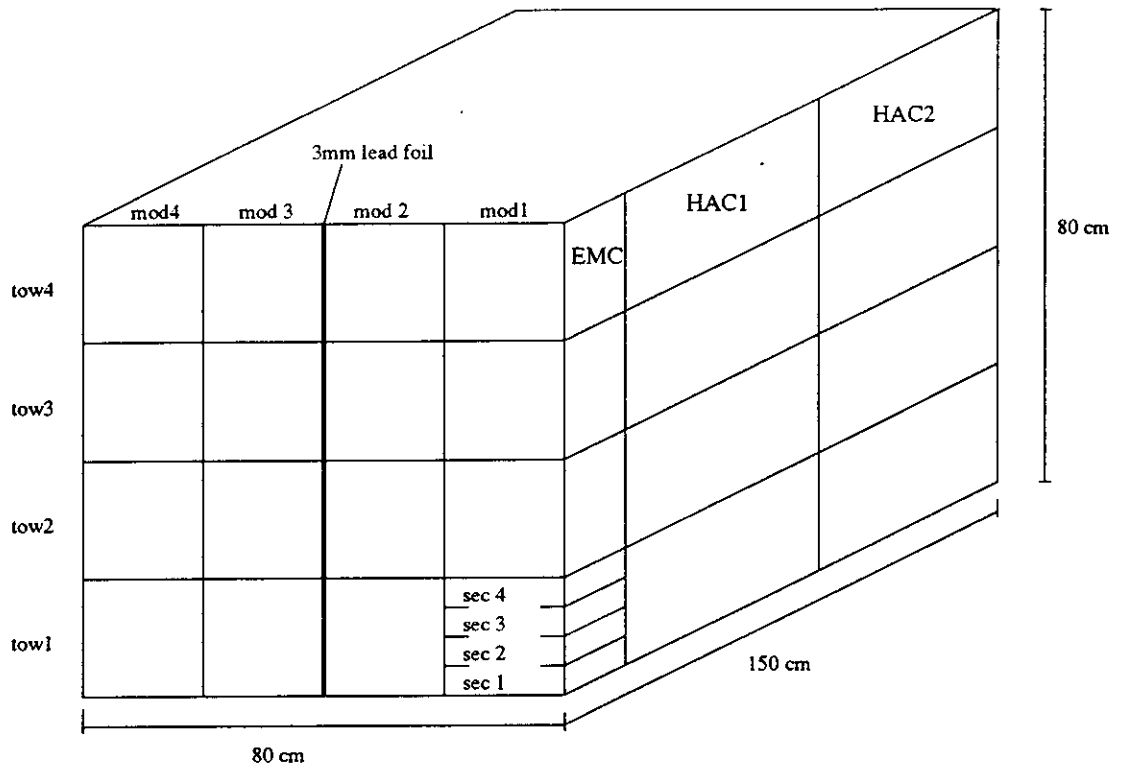
Figure 2.1: View of the ZEUS-FCAL prototype calorimeter.
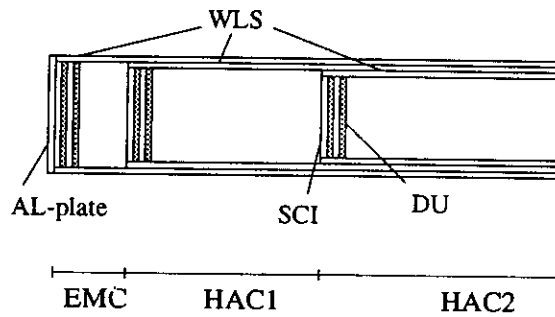
Figure 2.2: Structure of a tower.

	EMC	HAC
DU thickness	3.3 mm	3.3 mm
Cladding thickness	0.2 mm	0.4 mm
SCI thickness	2.6 mm	2.6 mm
Number of sampling layers	25	80 (HAC1) 80 (HAC2)
Effective X_0	7.4 mm	7.6 mm
Effective λ	210 mm	207 mm
Effective R_M	20.2 mm	20.0 mm
Effective density	8.7 g/cm^3	8.7 g/cm^3
Transverse segmentation	5 × 20 cm^2	20 × 20 cm^2
Longitudinal segmentation	25.9 X_0 (0.96λ)	3.09λ (HAC1) 3.09λ (HAC2)
readout channels	128	64

Table 2.1: Parameters of the prototype calorimeter.

2.1.2 Readout

The electronics used in this test was similar to the final electronics of the ZEUS calorimeter and has already been described in detail in [7]. The main elements are summarized below and in fig.2.3 the readout chain is shown.
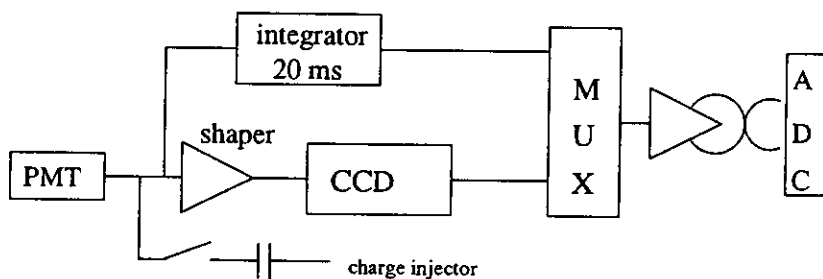
Figure 2.3: Readout of the calorimeter.

The PMT signals were connected to:

- - a DC coupled integrator used to measure the current induced by the uranium natural radioactivity (UNO signal),

- - an AC coupled shaper whose output was sampled 5 times every 96 ns, corresponding to the frequency of the HERA bunch crossing (see fig.2.4). The samples were pipelined by LeCroy MVV200 CCDs[2].

---

[2]The CCDs are replaced by a switched capacitor delay line in the final version of the electronics.

Integrators, shapers and CCDs were mounted on front end cards (analog cards) containing 12 channels each. These analog cards, installed just behind the calorimeter, were connected to the PMTs by 2 m long cables. Both the UNO signals and the pulse samples were multiplexed and digitized by 12 bits VME ADCs (digital cards) connected to the analog cards via 40 m flat twisted-pair cables. The ADCs were read out by a transputer (2TP board) and a main computer (SGI 4D/25) connected to the 2TP board.

The pulse shape after the shaper and the positions where the pulse is sampled, is shown in fig.2.4. The 5 pulse samples, H_0 to H_4, were used to reconstruct the charge deposited in each
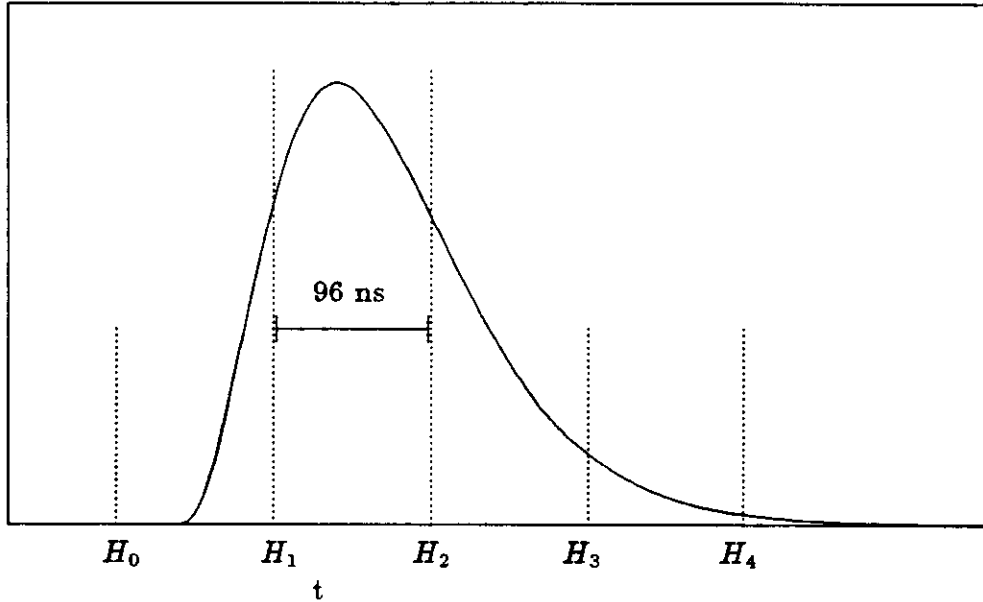
Figure 2.4: Pulse shape and sampling positions.

calorimeter channel and also the time of the signal. The time t=0 was defined as the time at which $H_1 = H_2$. At HERA the readout will be synchronized with the beam crossing so all events arrive at $t = 0$. This was of course not possible during the test since events arrived randomly in time relative to the CCD sampling clock. The charge reconstruction used the quantity:

$$H = (H_1 - H_0) + C(H_2 - H_0) \qquad \text{with} \quad C = -\frac{(\mathrm{d}H/\mathrm{d}t)_1}{(\mathrm{d}H/\mathrm{d}t)_2}.$$

The constant C is the ratio of slopes at the position of samples 1 and 2 for events arriving at $t = 0$. The quantity H defined in this way is insensitive to small time variations around $t = 0$. In fact, only 2 samples, H_1 and H_2, were used to reconstruct the charge. The first sample, H_0, was used as a pedestal. The reconstructed charge Q was a nonlinear function $f = aH^b$ of H since the response of the CCDs was nonlinear. The parameters a, b of the function f were determined by charge injection at the input of the shaper (see fig.2.3) and was used to correct H and the individual samples:

$$Q = f(H) \qquad \text{and} \qquad Q_i = f(H_i - H_0) \quad (i = 1...4).$$

The time T for each channel was reconstructed from the first sample and Q:

$$T = \tau(Q_1 - C_1 Q)/Q.$$

The constant C_1 was adjusted so that $T = 0$ for $t = 0$ and τ was used to adjust the time scale. The constants C, C_1 and τ were obtained from charge injection runs.

The energy weighted time (T_{WE}) of an event was calculated by:

$$T_{WE} = \frac{\sum Q_k^2 T_k}{Q_k^2}$$

where Q_k is the charge measured by each PMT and T_k is the corresponding time. The sum runs over all 192 PMT channels.

The formulae described before for Q and T are valid only for events around $t = 0$. Therefore an additional correction was performed depending on the reconstructed time T_{WE} of the event. The charge of an individual PMT was corrected by:

$$Q = \frac{Q}{1 + \sum_{i=1}^{4} a_i T_{WE}^i}$$

And the time of an individual PMT was corrected by:

$$T = \sum_{i=1}^{4} b_i T^i$$

also the energy weighted time (T_{WE}) was corrected by:

$$T_{WE} = \sum_{i=1}^{4} b_i T_{WE}^i$$

The total calorimeter r.m.s. noise (192 channels) was measured with random triggers and amounted to 0.84 pC (600 MeV electron equivalent energy). This noise is dominated by the electronics because of the low amplification of the photomultipliers.

2.1.3 Calibration

The calibration of the calorimeter channels was achieved with the help of:

- charge injection measurements performed every 24 hours,

- uranium radioactivity measurements performed every 8 hours,

- an electron calibration cycle performed at the beginning of the test.

The aim of the charge injection runs was to correct for the nonlinearities in the response of the CCDs, to calibrate the pipeline part of the readout and finally to determine the constants C, C_1 and τ introduced in the previous section.

The calibration of the EMC channels was obtained from a scan with the 30 GeV/c electron beam incident at the center of all EMC sections. It was shown in [3] that the current induced by the uranium natural radioactivity (UNO signal measured via integrators) can be used to trace PMT gain variations within 1% and therefore keep the quality of the initial electron calibration during all the test. It was also shown that the UNO signal also provides a relative calibration of the HAC channels with 1% precision.

The intercalibration between EMC and HAC channels was obtained by choosing the intercalibration parameter α defined by :

$$E = E_{EMC} + \alpha \cdot E_{HAC}$$

which gives $\epsilon/\pi = 1$ for p $= 30$ GeV/c. The value of α obtained in this way provides also an optimum energy resolution for hadrons. It was shown in [2,3] that e/π is independent of momentum at the level of 1% in the range 10 - 100 GeV/c, as expected for a compensating calorimeter.

2.2   The Interaction Trigger

2.2.1   Mechanical Construction

The interaction trigger consisted of a target, a trigger system and a veto system. In addition a presampler was placed in front of the calorimeter. A schematic view of the set up is shown in fig.2.5.
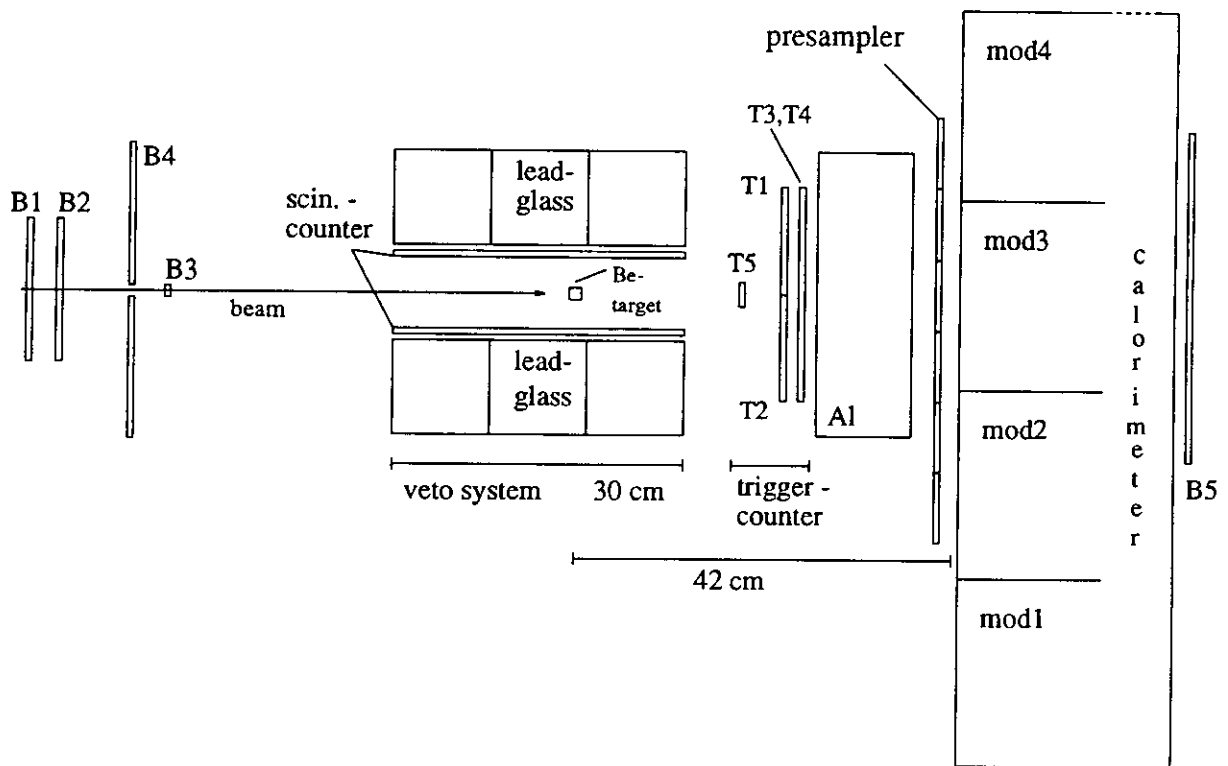
Figure 2.5: Setup of the interaction trigger.

For the target a beryllium block of 20 × 20 × 13 mm^3 was chosen. In longitudinal direction the target length corresponds to 0.03 λ [6] and the probability for an inelastic interaction is about 3 %. A thin target was chosen in order to reduce the energy losses within the target. As an energy measurement with a precision of approximately 1 % is possible, the target losses

should be in the same order to reduce systematic uncertainties. Due to the thin target it was achieved that the energy loss fluctuations were lower than the inherent resolution of the calorimeter. The low interaction probability, on the other hand, requires good filter properties of the trigger system.

The trigger system consisted of four 12.5×25 cm^2 scintillation counters $T_1....T_4$ and one 4×4 cm^2 scintillation counter T_5 shown in fig.2.6 and 2.5. The thickness of each counter
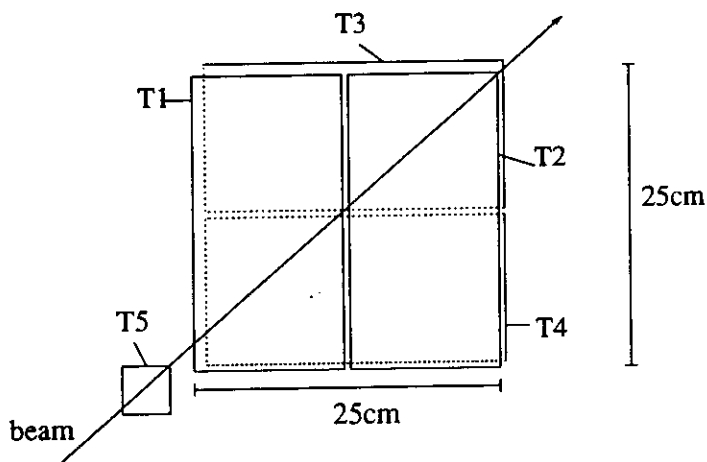
Figure 2.6: The five trigger counters.

was 2 mm corresponding to 0.0025 λ. The counters $T_1..T_4$ were arranged into two planes each 25×25 cm^2. The first plane consisted of counter T_1 and T_2. The gap between both counters was in vertical direction. The counters measured the left-right difference of the charged multiplicity. The gap of the second plane, consisted of T_3 and T_4, was in horizontal direction. The counters measured the up-down difference. The width of the gap was 1-2 mm and was due to the aluminum and plastic wrapping of the counters. The distance between both planes was 2 mm. The first plane was fixed 21.5 cm downstream the beryllium target, the second plane was fixed at 21.7 cm respectively. Trigger counter T_5 was placed 3.5 cm in front of the first trigger plane.

In fig.2.7 a sketch of the veto system is shown. The veto system consisted of eight lead glass counters and four scintillation counters. The lead glass counters were made out of SF5 glass. They are of trapezoidal shape, 30 cm long and 10×10 cm^2 at one end and 10×8 cm^2 at the other end. A PMT was glued to the 10×10 cm^2 side. They formed a $10 \times 10 \times 30$ cm^3 rectangular tube. In this tube the scintillation counters were placed. Two of the scintillation counters were $8 \times 0.4 \times 30$ cm^3 and the other two $10 \times 0.4 \times 30$ cm^3. In this tube the target was fixed by a 1 cm thick styropor frame. The center of the target was 12.4 cm in front of the rear side of the veto system.

Each trigger scintillation counter and each veto scintillation counter was read out by a light guide connected to a PMT. Due to mechanical reasons the light guide was bent. The bending angle was 90°.

The whole setup was mounted on a table. This table was put on another table so that the whole setup could be moved parallel to the beam line. For horizontal movements the whole
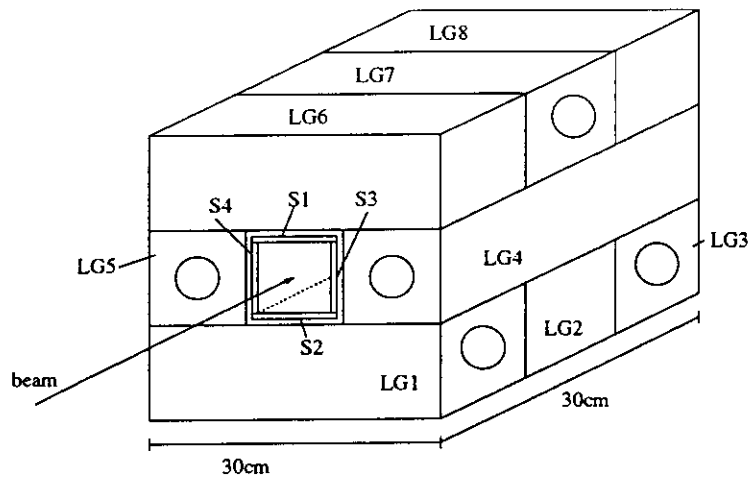
Figure 2.7: The veto system.

setup had to be moved by hand. In the vertical direction it could be lifted by revolving feet. The position of the interaction trigger setup relative to the beam line was adjusted by moving it until the rates measured in the four trigger counters $T_1...T_4$ were almost equal ($\pm 20\%$ from half of the total counting rate in a trigger plane).

The presampler consisted of six identical scintillation counters. Each of these counters has a dimension of $8 \times 80 \times 0.5$ cm^3. In fig.2.8 the position of the presampler counters relative to the calorimeter are shown.
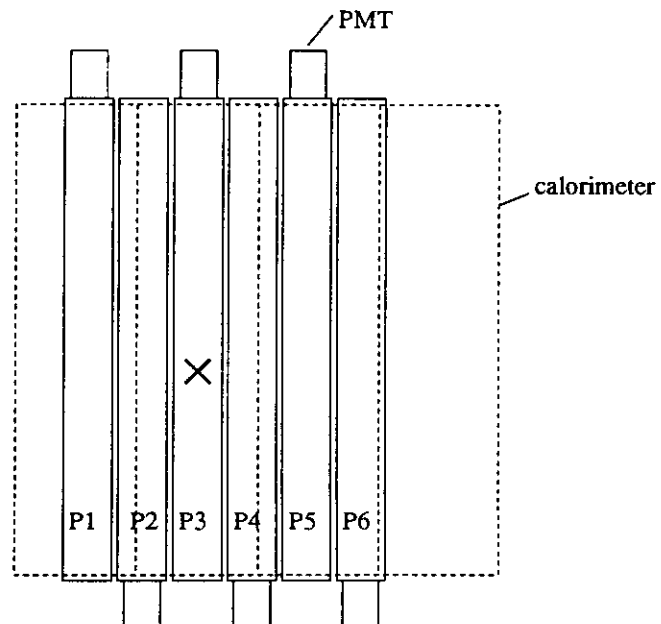
Figure 2.8: The presampler counters. The cross indicates the beam position.

2.3 Readout

The PMT outputs of the trigger counters were connected via 20 m long coaxial cables to passive signal splitters. The signal of each trigger counter was split into three signals with a ratio of 1 : 0.5 : 0.05. The highest signal was connected to a discriminator providing a signal for the trigger logic. The other two signals were connected to a CAMAC based LeCroy 2245a ADC. These two signals have a relative ratio of 1 : 10 so that the whole dynamic range of a trigger counter signal was covered and a good separation between the signal of a single particle and the ADC-pedestel was achieved ($ADC_{ped} - ADC_{mip} \approx 100$ ADC-channels).

One output signal from each trigger counter was connected to a discriminator with an adjustable threshold. The five logical signals from the discriminators were used for a trigger signal. A coincidence (fivefold AND) was chosen. The mean pulse height for a single beam particle at the discriminator input was adjusted to 100 mV. The discriminator threshold for the trigger counters $T_1..T_4$ was adjusted to 30 mV and the threshold for the trigger counter T_5 was adjusted to 200 mV.

The signals of the veto lead glass counters and veto scintillation counters were only digitized by LeCroy 2245a ADCs.

The output of the presampler was also digitized by LeCroy 2245a ADCs. The large dynamic range, at least of the central counter required a splitting of the signal. As in the case of the trigger counter a 1 : 10 splitter was chosen.

The gate width for the ADCs was 200 ns.

2.3.1 Calibration

After the interaction trigger setup was positioned relative to the beamline, the trigger counters were calibrated. The coincidence rate for each trigger counter with the beam counters (see fig.2.5) was measured for different gains of the trigger counter PMTs. The threshold of the discriminator was set to 100 mV. For high voltages (and/or low threshold) the rates saturated. The gain for each PMT was set, so that the measured rate was half of the saturation rate. This means that the mean pulse height of a single particle penetrating a trigger counter is 100 mV.

As the veto counters could not be exposed to the beam the high voltages were set somehow arbitrarily. They were set so that the signal of each counter was well separated from the ADC-pedestel. In addition only a few per cent of the events should saturate the ADC. This adjustment was done with jet events. At the end of the run period each veto counter was removed from the setup and calibrated by the 100 GeV hadron beam. The incident position of the beam was in the middle of a counter. The track length of the particles was 9 cm in the lead glass counters and 0.4 cm in the veto scintillation counters respectively.

The presampler counters were also calibrated with single particles. The incident position of the beam was in the middle of each counter. The attenuation length of each counter was measured by a vertical scan, ± 30 cm around the center position.

For the trigger counters, veto counters and presampler, the transformation of the measured ADC-channel number into the calibrated signal was done by:

$$N = \frac{ADC - ADC_{ped}}{ADC_\pi - ADC_{ped}}$$

where N is the calibrated signal, ADC is the measured ADC-channel number, ADC_{ped} is

the pedestel of the ADC and ADC_π is the mean ADC-channel number determined by the calibration runs. The pedestel values were measured every 8 hours.

2.4 Beam Line Setup

The experiment has been done at the CERN SPS X5 testbeam. The tertiary beam was produced by particles resulting from 120 GeV π^- interactions with Cu or Pb targets. The particles from this interaction were momentum selected by a spectrometer. The particle type composition of the beam was determined by the choice of the target and of the absorber following the target. For hadrons a copper target followed by a 5 mm thick lead absorber was used. In the absorber the produced electrons are absorbed. For electrons a lead target without an absorber was used. Acceptable beam rates could be obtained from 10 to 110 GeV. However, for measurements with the interaction trigger an acceptable rate was obtained for beam energies above 50 GeV. At these energies the beam containes π^- as well as μ^-. At 100 GeV the beam contained about 40 % pions and 60 % muons. With decreasing energy the muon content was decreasing.

The momentum bite of the beam was determined by the collimator setting. The pion content of the beam relative to the muons is enriched by a wide opening of the collimator. A collimator setting of ±25 mm was used. The dependence of the momentum acceptance versus collimator opening is about 1 % / 5 mm.

The experimental setup is shown in fig.2.5. The beam was defined by a coincidence of four scintillation counters $B_1...B_4$. The size of B_1 and B_2 was 10 × 10 cm^2. The fingercounter B_3, a 4 mm × 2 cm scintillation counter, was used to get a well focused electron beam. For hadrons this counter was not used because of the reduced rate. B_4 was a 80 × 80 cm^2 scintillation counter with a 3 cm diameter hole in the center and was used as a veto to reject beam halo events. Behind the calorimeter a 80 × 80 cm^2 scintillation counter was placed to record energy leakage and in particular muons penetrating the calorimeter. It was not used in the trigger. The signals of all the beam counters were digitized by LeCroy 2248a ADC's.

Trigger conditions From the logical signals of the beam counters the following trigger signals were obtained:

$$beam = B_1 \cdot B_2 \cdot \overline{B_4}$$

$$electron = beam \cdot B_3$$

$$hadron = beam$$

The trigger defined by the five trigger counters of the interaction trigger is:

$$trigger = T_1 \cdot T_2 \cdot T_3 \cdot T_4 \cdot T_5$$

As the mean pulse height of a single particle was 100 mV the threshold for $T_1..T_4$ was set to 30 mV and for T_5 the threshold was set to 200 mV. The trigger that finally indicated a jet event was defined by:

$$interaction = hadron \cdot trigger$$

Chapter 3

Measurements

In this chapter the results of the measurements with the prototype calorimeter using the interaction trigger are presented. In the following sections the term 'jet' will be used for the multiparticle system created by an inelastic pion-target interaction. However it should be noted that in regard to multiplicities, energy spectrum of the jet particles, particles types etc. these jets are different from those originating in inelastic electron-proton scattering at HERA. This complicates the application of the test results for the calorimetry at ZEUS.

The first two sections present common properties of the jet signals measured by the interaction trigger counters and the calorimeter. In Section 3 the energy measurement for jets are discussed. The influence of the vetocounter to determine the jet energy that actually enters the calorimeter is discussed. The energy calibration and energy resolution for jets is compared with those for pions.

The effects of passive material placed in front of the calorimeter are discussed in Section 4. Correction methods are investigated by using the charged multiplicities in front and behind the passive material to correct for the energy loss within this material.

3.1 Charged Particle Multiplicities

A measure of the number of charged particles in the beam can be obtained (1) from the pulse height of the trigger counters and (2) from the presampler.

1) Trigger Counters The trigger counters, described in Chapter 2.2.1, measured the charged multiplicity in the forward direction within a solid angle of about three steradians. The charged multiplicity is measured in two planes. The first plane consists of counters T_1 and T_2 and is just in front of the second plane, that consists of counters T_3 and T_4. The correlation of both planes is shown in fig.3.1. The r.m.s. of the relative difference of the charged multiplicity measurement by the two planes is approximately 40 %. It has been calculated by the difference of the two planes divided by the sum of the two planes.

The charged multiplicity N_{trig} is the average pulse height of both trigger planes, normalized to the mean pulse height for single particles. In fig.3.2 the distributions for jets and pions are shown. For pions the distribution is Landau like with a full width half maximum (fwhm) of about 1.7 particles.

The distribution for jets has two maxima. The first one is found at low values with a most probable value around 2 particles, and is most likely due to pions making no nuclear interaction in the target and producing only a few secondary particles like δ-electrons and

14

trigger plane 2 [*char.par.*]
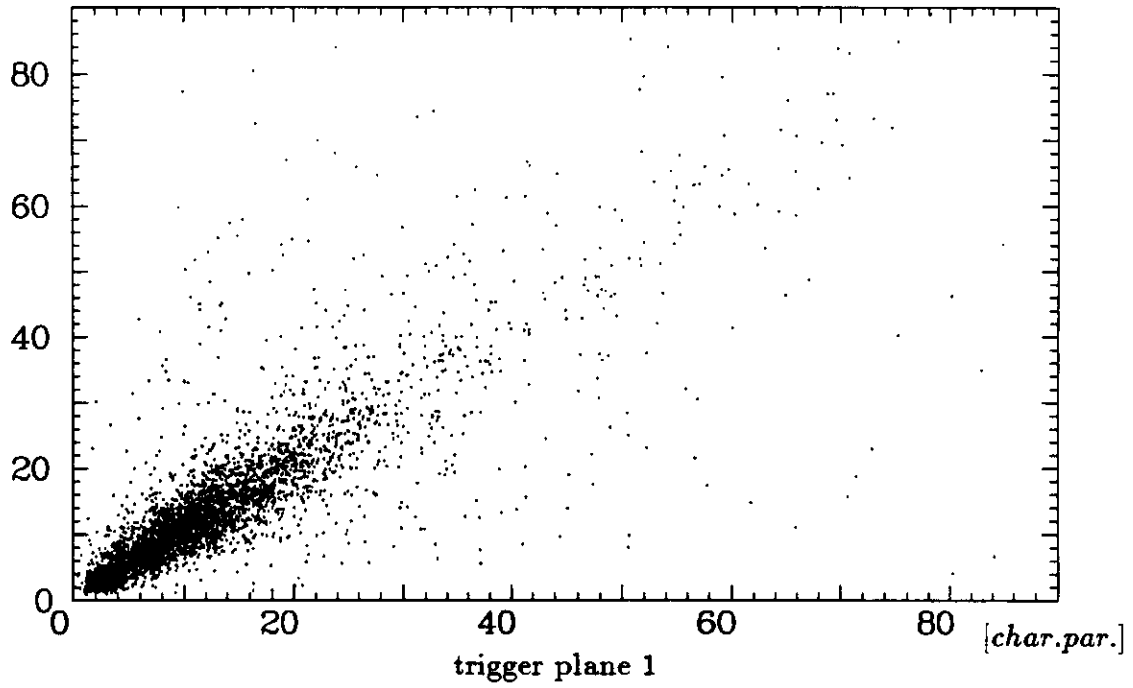
Figure 3.1: Charged multiplicity measured in trigger plane 1 versus plane 2.

entries
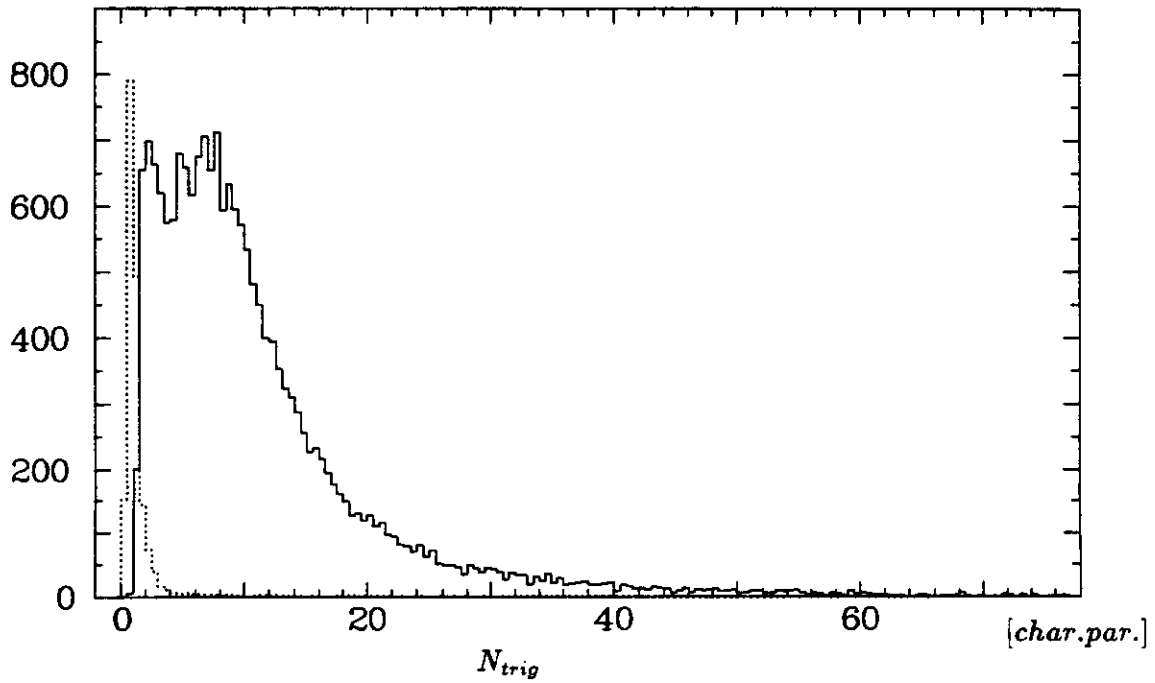
Figure 3.2: Charged multiplicity N_{trig} for jets (solid line) and pions (dotted line)

photons. The energy deposition of these events in the calorimeter is similar to those of pions which do not trigger. These events were rejected by requiring a charged multiplicity N_{trig} larger than four particles. The remaining distribution is due to pions that inelasticly interact in the target. More then 90 % of all events are due to these inelastic interactions.

The mean charged multiplicities $\overline{N}_{trig}$ for different jet energies are presented in table 3.1. The mean charged multiplicity is only slightly dependent on the energy and is in good agreement with a logarithmic behavior $\overline{N}_{trig} \sim \ln s$ where $\sqrt{s}$ is the center of mass (cms) energy of a pion and a nucleon of the beryllium target.

energy [GeV]	$\sqrt{s}$ [GeV]	$\overline{N}_{trig}$ [charged particles]	$\ln s / \overline{N}_{trig}$
50	9.7	11.4 ±.08 (10.4)	0.399 ±.004
75	11.9	12.3 ±.11 (10.6)	0.402 ±.004
100	13.7	13.5 ±.09 (11.7)	0.388 ±.004

Table 3.1: Charge multiplicity N_{trig} for jets. The r.m.s is given in brackets.

In addition to the trigger counters $T_1...T_4$ a fifth counter T_5 was in the trigger logic. The counter T_5 measured the charged multiplicity within a solid angle of 0.15 sr which is only 5 % of that measured by N_{trig}. With increasing charged multiplicity N_{trig} the fraction measured by the counter T_5 is decreasing as shown in fig.3.3. The reason is, that the opening angle of the jet particles increases with increasing multiplicity.
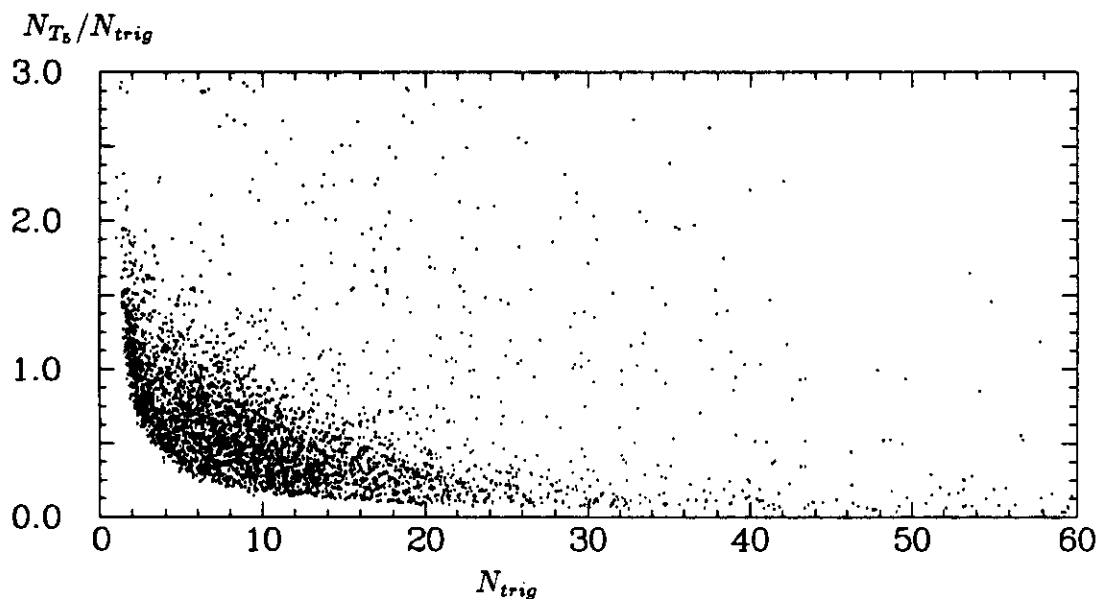
Figure 3.3: Fraction of the charged multiplicity measured in counter T_5

There are several systematic effects which deteriorate the multiplicity measurement:

- the ionization loss of a particle is different from that of a minimum ionizing particle

- nonuniformity of the trigger counter response

- drift of the calibration with time

The ionization loss of non relativistic particles is much larger than that of a minimum ionizing particle. In particular protons released from a beryllium nucleus have kinetic energies less than 0.5 GeV. The ionization loss for such a proton is approximately five times larger than the one of a minimum ionizing particle. This increase is partly compensated by the scintillator saturation effect. The saturation effect suppresses the response i.e. the signal per unit deposited energy. It is due to the strongly non-linear behavior of scintillators in their response to densely ionizing particles.

The jet particles traverse the trigger counter with an angle so the track length is increased. With a largest possible angle of 22° the increase of the mean ionization loss is 7 %. By a Monte Carlo simulation the effects of increasing ionization loss for low energetic particles and increasing track length have been estimated (4.3.1). The measured charged multiplicity N_{trig} is, on the average, about 30 % larger than the number of charged particle tracks traversing the trigger counter.

The nonuniformity of the trigger counters has not been measured, therefore the influence of this effect to the charged multiplicity measurement can not be estimated. Calibration changes are due to a drift of the photo multiplier voltages. A comparison of calibration runs taken at different times shows that the changes are less than 8%.

2) Presampler The presampler covers a solid angle of approximately 3.6 sr, larger by 20% than the trigger counters. In Fig. 3.4 the charged particle distribution for 50 GeV jets and pions are displayed. For pions the distribution is Landau like with a full width half maximum (fwhm) of about 2 particles. The mean charged multiplicity $\overline{N}_{pres}$ for different energies and
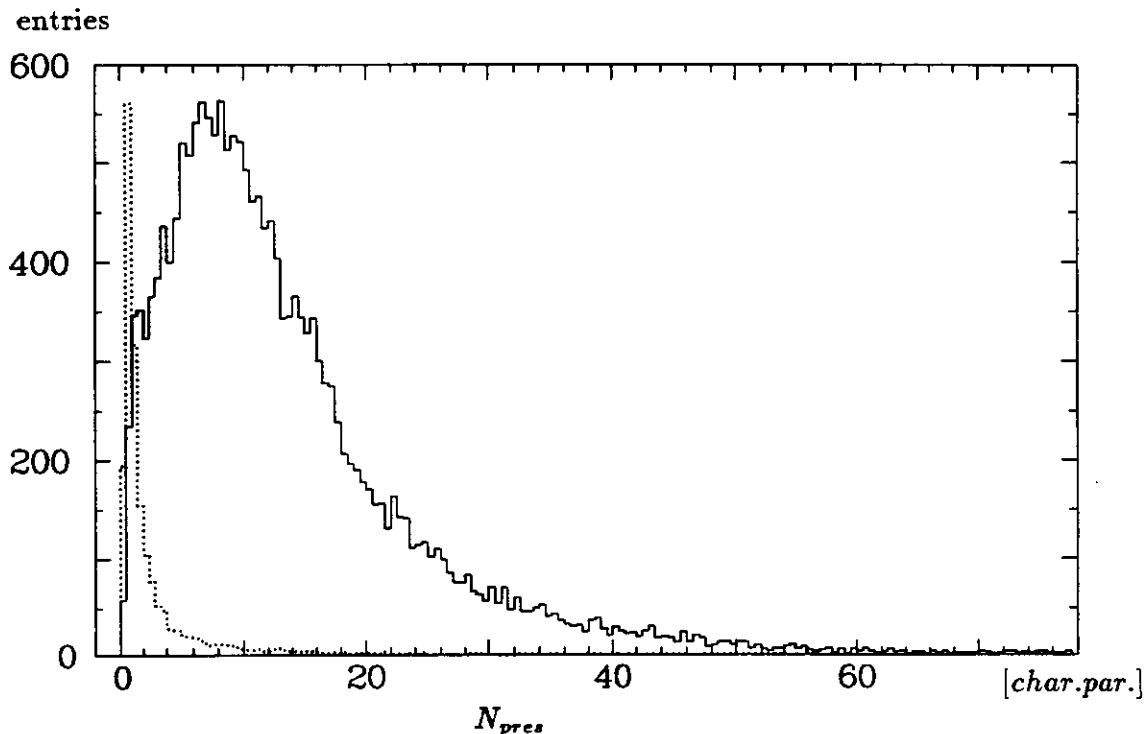
Figure 3.4: Charged multiplicity N_{pres} for jets (solid line) and pions (dotted line).

also for different values of the aluminum thickness in front of the calorimeter are summarized in table 3.2. The mean multiplicities $\overline{N}_{pres}$ are approximately 20 - 25 % larger than the

mean multiplicities measured by the trigger counters. If an aluminum plate is in front of the presampler the mean charged multiplicity increases due to interactions of the jet particles in the aluminum. For 10 cm aluminum the increase is $\approx$ 100 % and for 4 cm the increase is $\approx$ 40 %.

energy [GeV]	N_{pres} [charged particles]			$N_{pres}(d)/N_{pres}(0)$	
	0 cm Al	4 cm Al	10 cm Al	4 cm Al	10 cm Al
50	13.7	19.2	27.3	1.40	1.99
75	15.6	20.7	31.8	1.33	2.04
100	17.0	24.0	36.8	1.41	2.16

Table 3.2: Mean charged multiplicity measured by the presampler N_{pres} with aluminum of different thickness in front of the calorimeter. $\overline{N}_{pres}(d)/\overline{N}_{pres}(0)$ is the ratio of the mean charge multiplicity for 4, 10 cm aluminum plates divided by the mean charged multiplicity without aluminum plates. The statistical error of $\overline{N}_{pres}$ is smaller than 1 %.

The presampler was horizontally segmented into six stripes each 8 cm wide. The fraction of the charged multiplicity measured in each of the stripes is shown in fig.3.5. Approximately 77 % of the particles are detected by the three central counters.

charged multiplicity fraction [%]
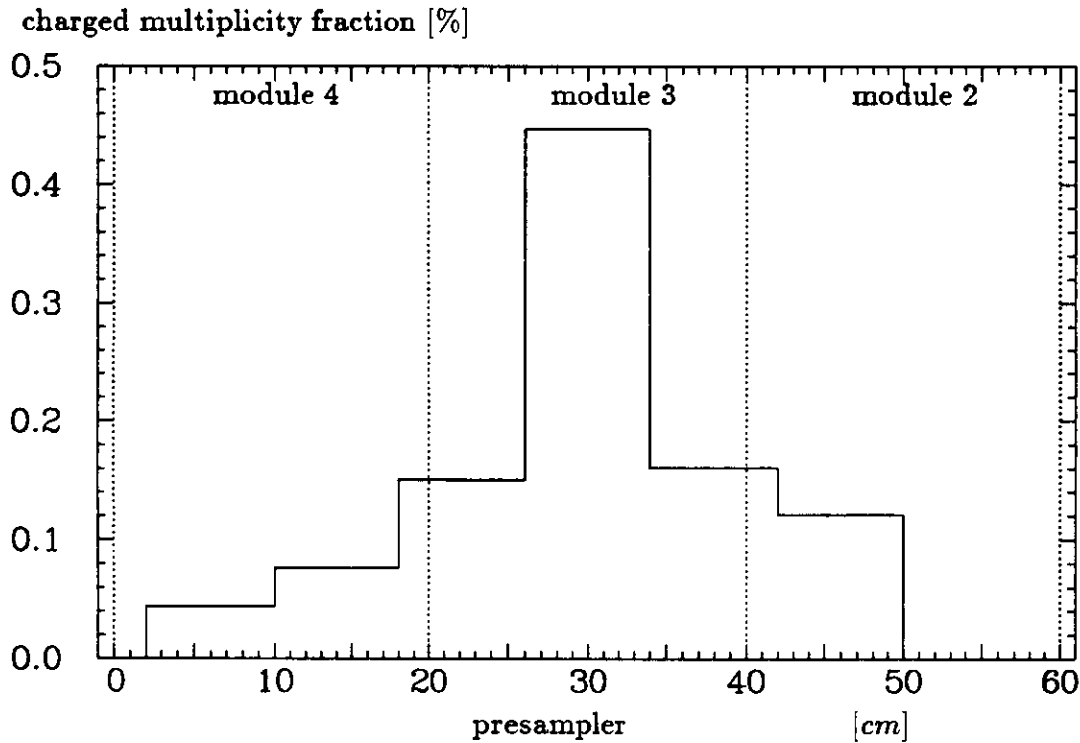
Figure 3.5: Fraction of the charged multiplicity measured in the six presampler stripes for 50 GeV jets. The dotted lines are the positions of the calorimeter modules 4, 3 and 2.

The charged particle measurements by the trigger counter and the presampler are compared in fig.3.6 by plotting their relative difference

$$A = \frac{N_{trig} - N_{pres}}{N_{trig} + N_{pres}}.$$

With increasing presampler multiplicity the relative difference gets more negative which means that the presampler measures more particles than the trigger counter. The distribution of A (fig.3.6) is centered at -0.08 with a r.m.s of 0.3. The difference of the multiplicities are due to the larger angular acceptance of the presampler and are also due to particles which scatter from the vetocounter into the presampler but do not traverse the trigger counters. The r.m.s. value of 0.3 is close to the r.m.s. value for the relative difference between the two planes of the trigger counters (r.m.s. $\simeq 0.4$).
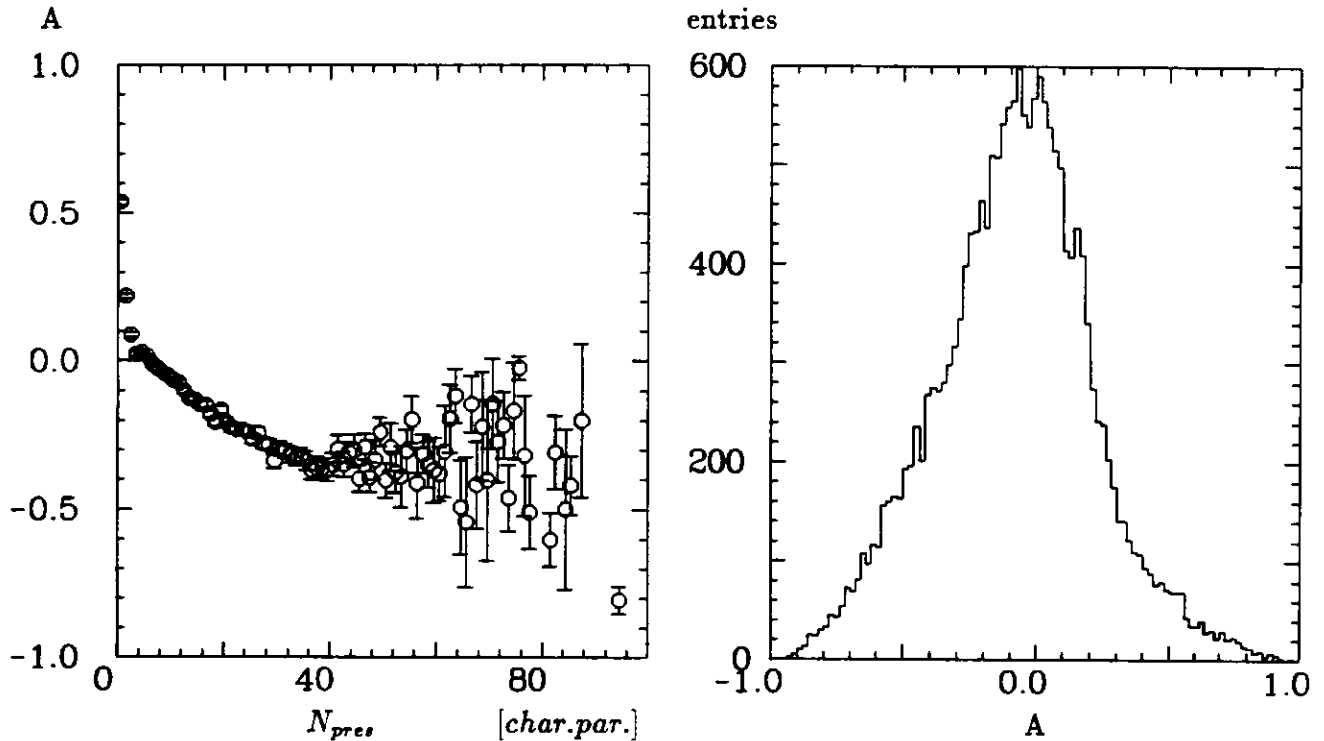
Figure 3.6: A versus N_{pres} (left) and the distribution of A for 50 GeV jets.

3.2   Calorimeter Event Shape

In fig.3.7 the distribution of the measured calorimeter energy is shown for 100 GeV jets. The peak at 4 GeV is due to muons. They can set the trigger by δ-electrons, bremsstrahlung photons and pair production. These events were rejected by requiring $E_{cal} > 40$ GeV. The main peak around 100 GeV is due to jets. This distribution shows a long tail towards low values. This tail is due to jet events where a fraction of the particles does not hit the calorimeter and also due to energy leakage out of the calorimeter sides. The tail will be removed by cuts on the veto counter described in section 3.3.1.

The longitudinal and lateral shower distribution for jets and pions can be compared by looking at the energy deposition in the individual calorimeter cells.

Longitudinal distribution   The longitudinal energy distribution is measured by the energy deposited in the three calorimeter sections. The depth of the EMC section is 1λ and the HAC1 and HAC2 are 3λ deep. In fig.3.8 the mean energy fractions for jets and pions are
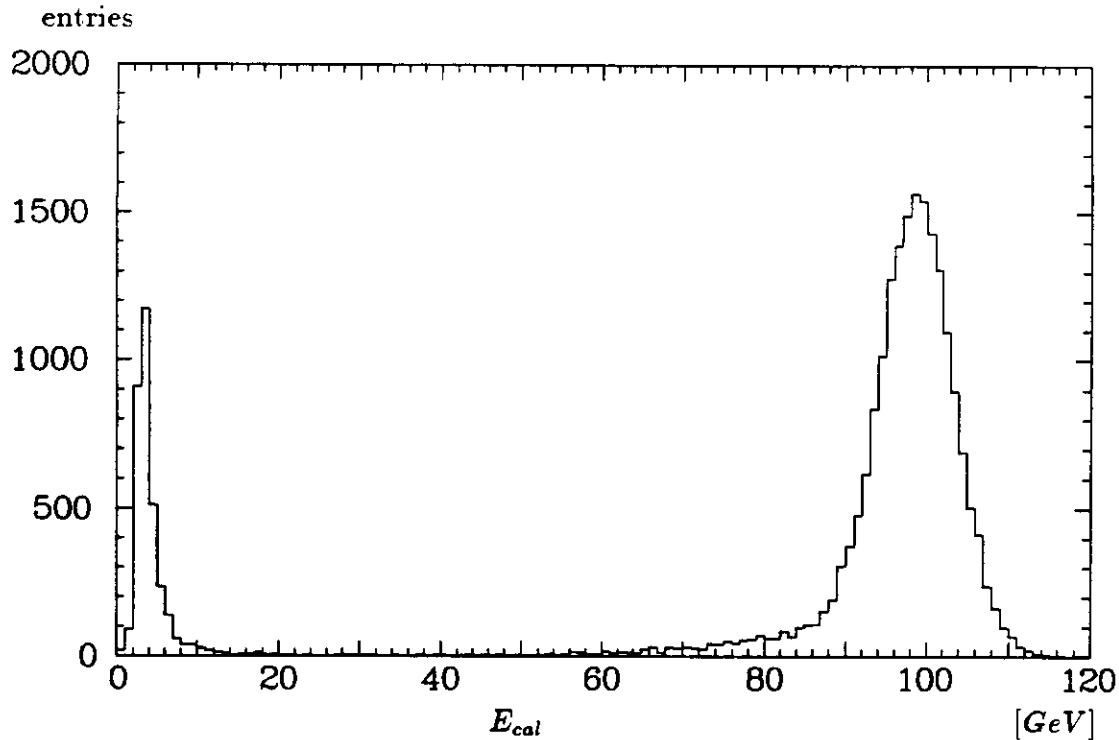
Figure 3.7: Distribution of the calorimeter energy E_{cal} for 100 GeV jets.

shown. For jets more energy is deposited in the EMC compared to pions, which means that the energy center of gravity for jets is shifted towards the calorimeter front face. The energy fraction in the two HAC sections is smaller for jets, therefore the energy leakage to the rear side of the calorimeter is reduced compared to the one for pions. This energy leakage can be estimated by comparing the mean calorimeter energy without and with a cut on the HAC2 energy fraction. If it is required that the HAC2 energy fraction is less than 10 % the mean calorimeter energy for pions increases by 0.3 % at 50 GeV and 0.7 % at 100 GeV. If the cut is even less than 10 % the mean energy is almost constant and the longitudinal energy loss is estimated to be smaller than 0.1 % at 50 GeV and 0.2 % at 100 GeV. The energy leakage for jets can be neglected compared to the one for pions.

In table 3.3 the results for the energy fractions in the three calorimeter sections are summarized for jets with different energies and passive material (aluminum) in front of the calorimeter.

Lateral distribution The lateral energy distribution in the calorimeter is given by the lateral shower evolution of the incident particles and, in the case of jets, by the angular spread of the jet particles. The lateral width is of interest for the estimation of the lateral energy leakage. In table 3.4 the energy fraction deposited in the sixteen calorimeter cells is shown for 50 GeV jets and pions. The events were selected by the selection criteria summarized in Section 3.3.2.

The beam was incident in module 3 tower Nr. 2, and 2.5 cm above the tower center. More then 80 % of the energy is deposited in module 3. In the outer most module the energy fraction is less then 1.3 % and with increasing energy this fraction decreases.

It is not possible to get an exact value for the lateral energy losses for jets respectively
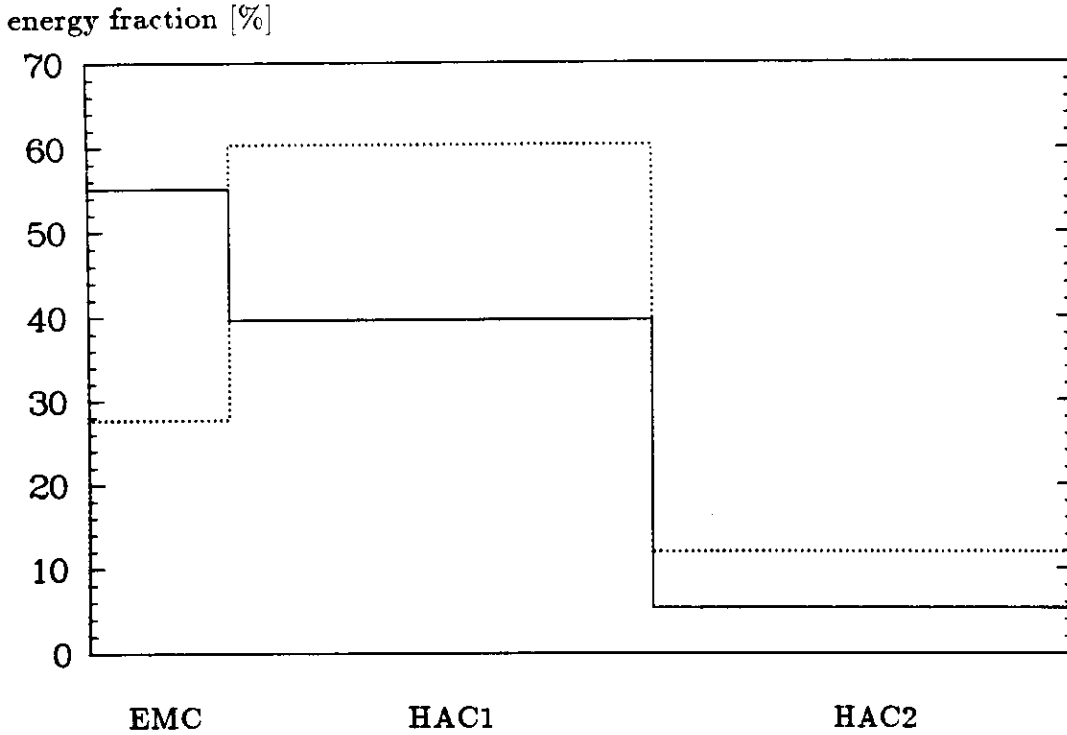
energy fraction [%]

Figure 3.8: Mean energy fraction in the three calorimeter sections. The results are shown for 50 GeV jets (solid) and pions (dotted).

energy [GeV]	Al cm	f_{EMC} %	f_{HAC1} %	f_{HAC2} %
	0	55.1	39.6	5.3
50	4	56.5	38.4	5.1
	10	58.4	36.8	4.8
	0	53.1	40.8	6.2
75	4	54.6	39.6	5.8
	10	57.1	37.4	5.5
	0	51.9	41.5	6.6
100	4	53.1	40.4	6.6
	10	55.3	38.8	5.9

Table 3.3: Energy fractions (%) for jets. The events were selected by the criteria described in Section 3.3.2. The statistical error is less than 0.5 %.

tower	calorimeter module				calorimeter module			
	4	3	2	1	4	3	2	1
4	0.29	0.49	0.22	0.13	0.38	0.61	0.29	0.16
3	1.43	4.89	1.54	0.29	1.99	6.81	2.13	0.38
2	3.19	78.24	3.68	0.40	4.29	71.19	4.98	0.49
1	1.01	2.77	1.16	0.25	1.30	3.22	1.49	0.31

Table 3.4: Energy fraction (in %) measured by the sixteen calorimeter towers for 50 GeV pions (left) and jets (right).

for pions. The shape that describes the energy attenuation with radius is not known. Only a rough estimation is possible by considering the asymmetry of the setup. In fig.3.9 the setup is shown. A fifth module adjacent to module 4 would measure the same energy as module 1. At
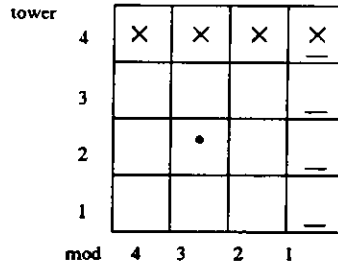
Figure 3.9: Incident position (dot) and prototype numbering. The crosses (bars) are the towers which were summed to calculate f_u (f_1).

least this energy is lost. In the vertical direction the energy loss was estimated by summing over the four upper towers of the four calorimeter modules. It is assumed that this energy would have been measured if additional towers were placed below the calorimeter. As the mean incident position is not in the middle of a tower this energy is somewhat overestimated. In table 3.5 the energy fractions f_1 measured in module 1 and the energy fractions f_u measured in the upper four towers are summarized. In the later analysis the interesting quantity is the ratio R of the mean energy of jets $\overline{E}^{jet}$ and pions $\overline{E}^{pion}$. If the mean energies are corrected by the lateral energy leakage this ratio will change to

$$R = \frac{\overline{E}^{jet}}{\overline{E}^{pion}} \rightarrow R = \frac{\overline{E}^{jet}}{\overline{E}^{pion}} \frac{1 + (f_1^{jet} + f_u^{jet})}{1 + (f_1^{pion} + f_u^{pion})}.$$

In table 3.5 the results for the energy fraction are summarized.

energy	f_1 [%]		f_u [%]		$\dfrac{1 + (f_1^{jet} + f_u^{jet})}{1 + (f_1^{pion} + f_u^{pion})}$
	jets	π^-	jets	π^-	
50	1.3 ±0.08	1.1 ±0.08	1.4 ±0.07	1.14 ±0.07	1.004 ±0.002
75	1.02 ±0.05	0.93 ±0.05	1.3 ±0.05	1.12 ±0.04	1.001 ±0.001
100	0.89 ±0.04	0.88 ±0.04	1.2 ±0.03	1.1 ±0.07	1.001 ±0.001

Table 3.5: Estimated lateral energy loss. f_1 is the energy fraction in module 1, f_u is the energy fraction in the upper four calorimeter towers for jets and pions respectively.

The lateral energy loss, estimated by this method, for jets is about 2.7 % for 50 GeV and decreases to 2.1 % for 100 GeV . As R is larger than 1 more energy is lost for jets than for pions by lateral leakage, although the difference is smaller than 0.4 %. As already mentioned previously this is only a rough estimation and it indicates only the order of the lateral loss.

3.3 Energy Measurement

3.3.1 Determination of the Jet Energy

The calorimeter does not see the full jet energy because jet particles with large polar angles do not hit the calorimeter. Therefore a vetocounter system, described in chapter 2.2.1, detected particles which leave the target with polar angles $> 22°$. Particles which are detected in the vetosystem may pass the calorimeter if their angles are large or they may enter the calorimeter but the incident position at the calorimeter face of such a particle is close to the calorimeter boundaries. Therefore a fraction of the particle energy may be lost by lateral leakage out of the calorimeter.

Two cut parameters N_s^c and N_l^c were introduced for the veto scintillation counter signal N_s and the veto lead glass counter signal N_l. The signals N_s and N_l are the sums of the signals measured in the individual veto scintillation counters and veto lead glass counters respectively. The events were selected by

$$N_s < N_s^c$$

and

$$N_l < N_l^c.$$

The dependence of the mean calorimeter energy of the cut parameter N_s^c and N_l^c is shown in fig.3.10 for 50 GeV jets. The difference of the mean calorimeter energy between a strong selection with the vetocounters ($N_s^c = .5, N_l^c = .5$) and no selection is approximately 1.6 % for 50 GeV - 100 GeV jets.

In the later analysis $N_s^c = 4$ and $N_l^c = 4$ were chosen. Due to the choice of these parameter values the calorimeter mean energy is approximately 0.5 % lower than for the stronger parameter values ($N_s^c = .5, N_l^c = .5$). Thus the energy not seen by the calorimeter and due to the above mentioned effects is about 0.5 % of the measured calorimeter energy. This result has been found for all jet energies measured.

The improvement of the energy resolution σ_E/E is shown in fig.3.11. The energy resolution improves by approximately 7 %. For the chosen cut parameter values the energy resolution is about 4 % worse compared to strong cut parameter values ($N_s^c = .5, N_l^c = .5$).

The number of events is reduced by approximately 55 % if the event selection with $N_s < 4$ and $N_l < 4$ is applied.

The charged multiplicity of a jet is correlated with the jet properties like the energy spectrum, ratio of kinetic to total energy, energy loss in the target etc. and the calorimeter response is sensitive to these properties. The veto counter signal is correlated to the charged multiplicity N_{trig}, shown in fig.3.12, because the angular spread of the jet particles increases with the charged multiplicity. However, for a veto counter signal $N_s < 4$ the correlation with the charged multiplicity is weak and therefore the energy loss detected by the veto system is not correlated to the charged multiplicity and therefore not correlated to energy losses in the target.
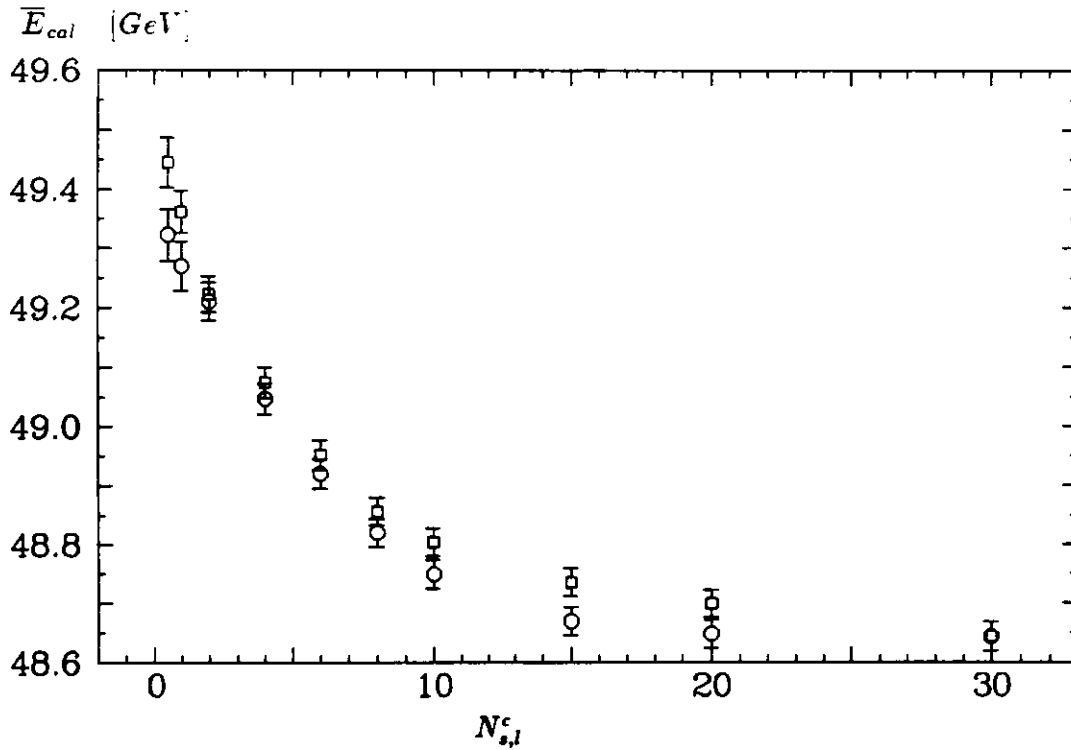
Figure 3.10: Mean calorimeter energy $\overline{E}_{cal}$ versus a selection on the veto counter signal N_s (circles) and N_l (squares) for 50 GeV jets.
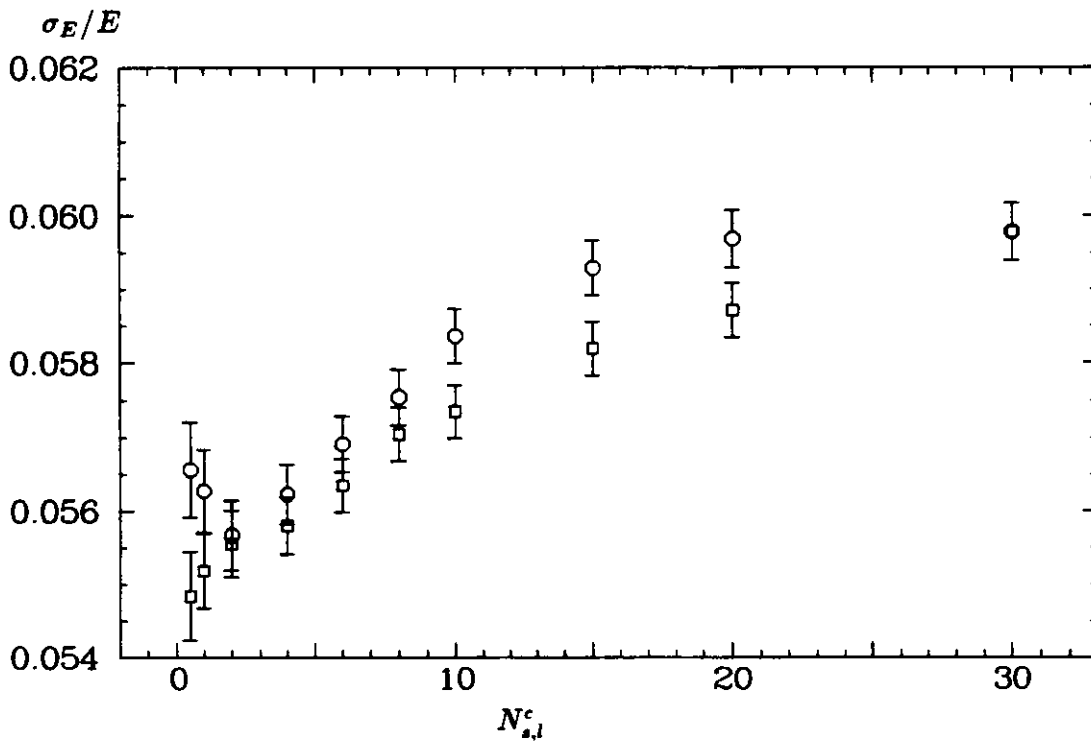
Figure 3.11: Calorimeter energy resolution versus a selection on the veto counter signal N_s (circles) and N_l (squares) for 50 GeV jets.

N_{trig} $[char.particles]$ $\overline{N}_{trig}$ $[char.particles]$
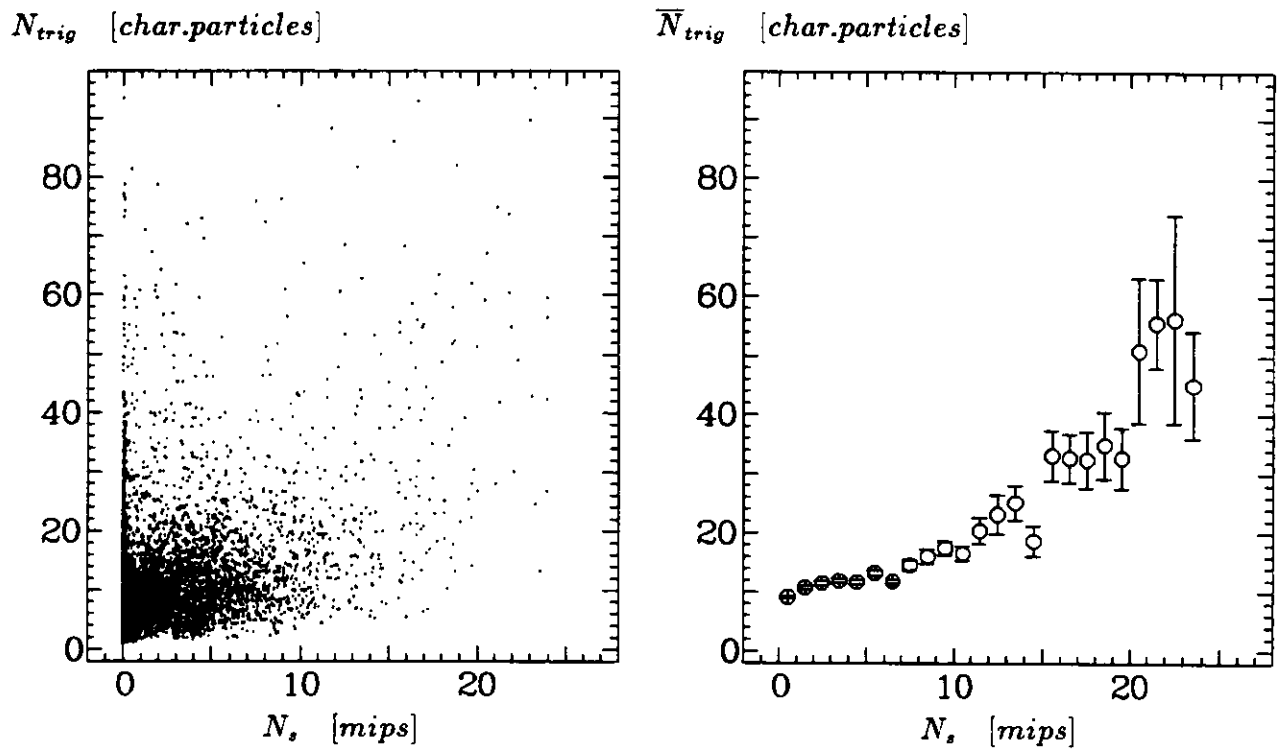
Figure 3.12: Charged multiplicity N_{trig} versus the veto scintillation counter signal N_s for 50 GeV jets.

3.3.2 Summary of Selection Criteria

The selection criteria finally used for the analysis of the energy calibration and energy resolution for jets are summarized here.

Beam muons were rejected by cutting on the calorimeter energy:

$$E_{cal} \geq 20, \quad 40, \quad 60, \quad GeV$$

for 50 GeV , 75 GeV and 100 GeV beam energy.

Longitudinal energy leakage for pions was reduced by requiring:

$$E_{HAC2}/E_{cal} \leq 0.1.$$

The following selections criteria were applied only for jets. The separation of non interacting pions from inelasticly interacting pions within the target was achieved by the charged multiplicity measured in the trigger counters.

$$N_{trig} \geq 4.$$

Energy losses for jets were limited by the veto counters:

$$N_{s} < 4.$$

$$N_{l} < 4.$$

The reduction of the event samples by all of these cut parameter is approximately 55% for jets and 20 - 50% for pions.

3.3.3 Energy Measurement for Jets

The calorimeter response to jets and pions for 50 GeV , 75 GeV and 100 GeV was measured. The events were selected by the criteria described above. In fig.3.13 the energy distributions for jets are shown. They are of gaussian shape and no tails in particular towards low values exist. The mean and standard deviation of the distributions were determined by fitting a gaussian using the method of least squares. The results of these fits for jets are shown in table 3.6, the values for pions are also shown for comparison.

energy [GeV]	type	$\overline{E}$ [GeV]	σ_E [GeV]	$\sigma_E/\sqrt{E}$ [%]	$E_{jet} - E_{pion}$ [GeV]
50	jet	49.20 ±.03	2.72 ±.02	39.3 ±.3	
50	pion	50.50 ±.06	2.83 ±.06	39.6 ±.6	-1.3 ±.1
75	jet	73.47 ±.06	3.56 ±.04	42.0 ±.5	
75	pion	74.95 ±.12	3.83 ±.12	44.2 ±1.2	-1.5 ±.18
100	jet	99.34 ±.05	4.31 ±.03	43.4 ±.3	
100	pion	100.06 ±.19	4.81 ±.14	48.1 ±1.4	-.7 ±.24

Table 3.6: Mean energy, standard deviation σ and energy resolution for jets and pions.

The energy resolution for jets as well as for pions does not achieve the nominal energy resolution (35 % /$\sqrt{E}$) of the calorimeter. This is because the beam momentum spread which
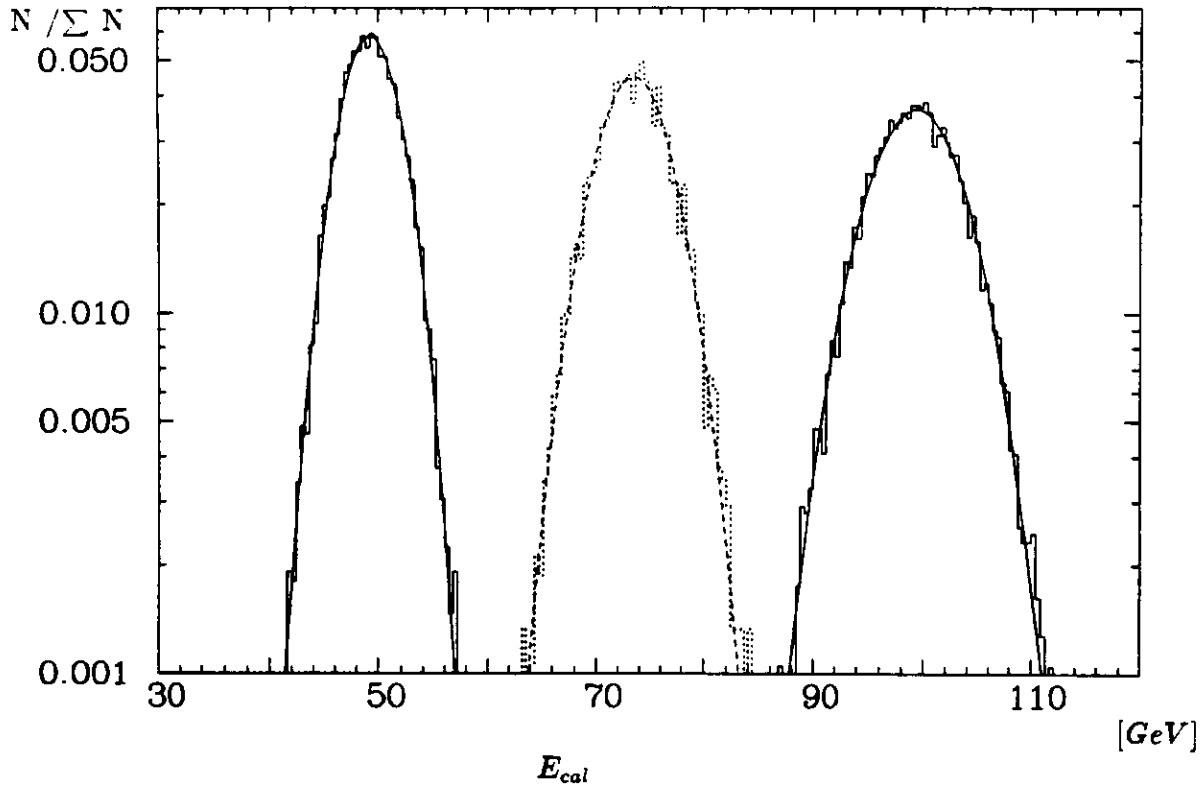
Figure 3.13: Calorimeter energy E_{cal} for jets. The normalized distributions are shown and the selection criteria were applied.

is about 2.5 - 3 % was not quadraticly subtracted. For the runs where the beam spectrometer was available the effect of the beam momentum spread has been verified.

The errors shown in table 3.6 are the statistical errors. Systematic errors for the mean energies have been estimated by runs of the same type taken at different times. The influence of a variation of the calibration constants was tested by using the calibration constants taken before the calibration constants which were used for the analysis. The systematic error of both effects was about 0.5 % and was much larger than the statistical error.

Discussion:

1) Mean energy: Comparing jets and pions of the same energy, table 3.6 shows that the jet signal is smaller than the corresponding pion signal. In fig.3.14 the relative energy difference given by

$$\frac{\overline{E}_{jet} - \overline{E}_{pion}}{\overline{E}_{pion}}$$

is shown. Within the statistical and systematic errors the energy loss $E_{pion} - E_{jet}$ was constant and amounts to 1.2 ±0.2 GeV.

The energy loss mechanism can be divided into two classes. The first class is due to the inherent properties of the calorimeter and the particle and energy composition of the jets. The second class results from energy losses due to the finite size of the calorimeter and energy losses within the target.

The following effects belong to the second class:

- longitudinal energy leakage out of the calorimeter

$$(\overline{E}_{jet} - \overline{E}_\pi)/\overline{E}_\pi$$
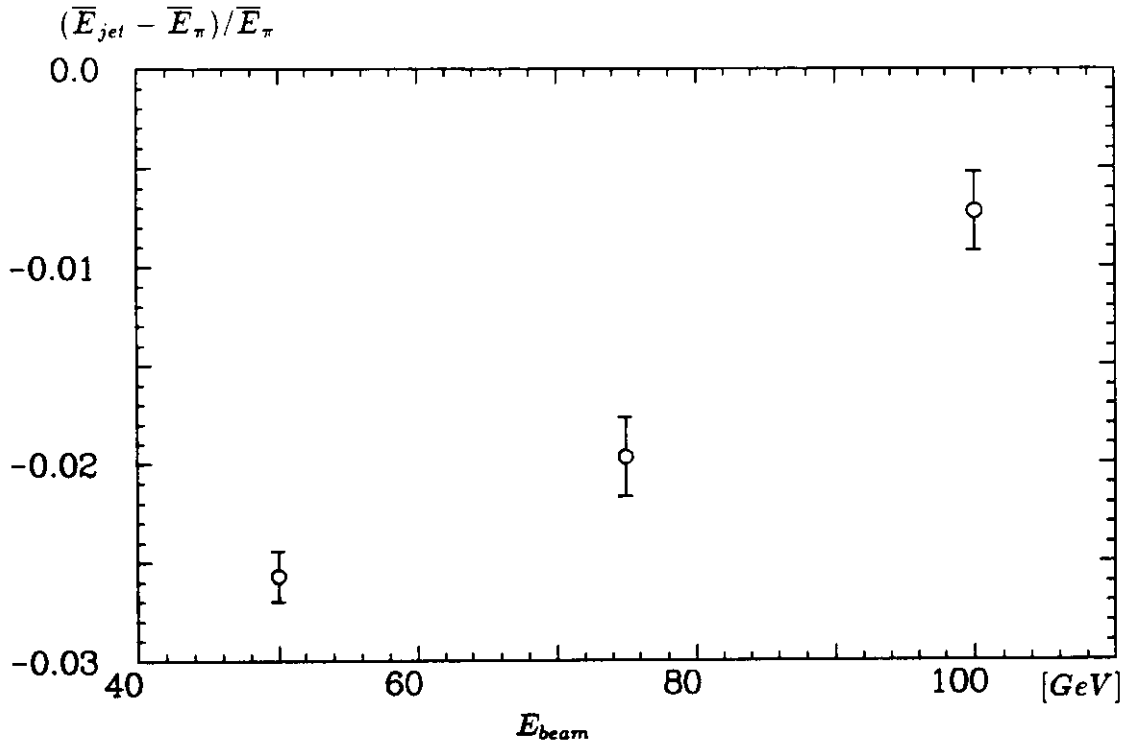
Figure 3.14: Relative energy difference of jets compared to the pion signal.

- lateral energy loss due to the finite size of the calorimeter

- particles which leave the target but do not enter the calorimeter (missing particles)

- energy loss in the target

In the last sections some of these effects have already been discussed. The target energy loss is the difference between the energy of the incident pion which creates a jet and the sum of the kinetic energies of the individual jet particles. This difference has been calculated by a Monte Carlo simulation (for more details see Section 4.3.4). However the energy measured by the calorimeter is not equal to the kinetic energy of the jet. In particular for low energy hadrons ($E_{kin} < 5$ GeV) the calorimeter response is not linear [2] but the measured energy is larger than the one expected for a linear response. Therefore the target loss will be partly compensated.

energy	missing part.	lateral loss	long. loss	expected diff. from Monte Carlo	sum	meausured difference
50	-0.5 ±0.1	-0.4 ±0.2	0.1 ±0.1	-1.7 ±0.22	-2.5 ±0.32	-2.57 ±0.13
75	-0.4 ±0.1	-0.1 ±0.1	0.2 ±0.1	-1.47 ±0.02	-1.77 ±0.27	-1.97 ±0.2
100	-0.5 ±0.1	-0.1 ±0.1	0.2 ±0.1	-1.19 ±0.01	-1.59 ±0.2	-0.72 ±0.2

Table 3.7: Expected energy difference from the Monte Carlo simulation and measured energy difference in %.

In table 3.7 the measured energy difference and the expected energy difference, calculated

by the Monte Carlo simulation, is shown. The expected energy difference [1] includes the effect of the low energy hadrons. From this table it is apparent that the energy difference is dominated by the target losses. The sum of the energy differences is comparable with the measured difference. However, this is only a rough comparison.

2) Energy resolution: The energy resolution for jets relative to those of pions is shown in fig.3.15. The energy resolution for jets is better than the one for pions and with increasing

$(\sigma_E/E)_{jet}/(\sigma_E/E)_\pi$
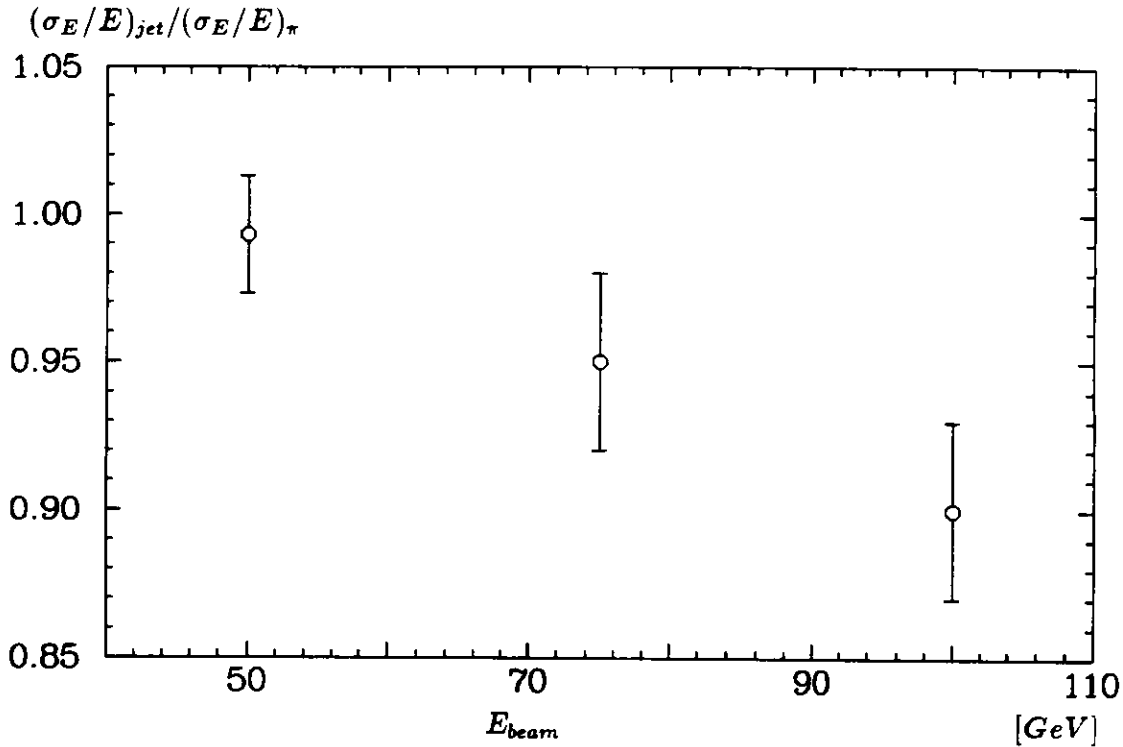
Figure 3.15: Energy resolution for jets relative to those of pions.

energy the resolution improves. The reason for this is not clear because the strength of the different effects that influence the energy resolution is not known.

3.4 Energy Measurement with an Aluminum Absorber

Material in front of the calorimeter will deteriorate the energy measurement because a fraction of the jet energy will be lost in this material. Aluminum plates of 4 cm and 10 cm thickness corresponding to 0.43 X_0 (0.1λ) and 1.07 X_0 (0.25 λ) respectively were placed in front of the calorimeter. In fig. 3.16 the calorimeter energy distribution for 50 GeV jets is shown. The shape of this distributions remains gaussian. In particular no tails towards low values exist with aluminum plates in front of the calorimeter. With increasing aluminum thickness the distribution is shifted to low values and in addition it gets broader. Again the mean and standard deviation were determined by fitting a gaussian and are summarized in table 3.8.

---

[1]This difference was calculated by the difference between the kinetic energy of the beam and the quantity E_{coh}, see 4.3.4
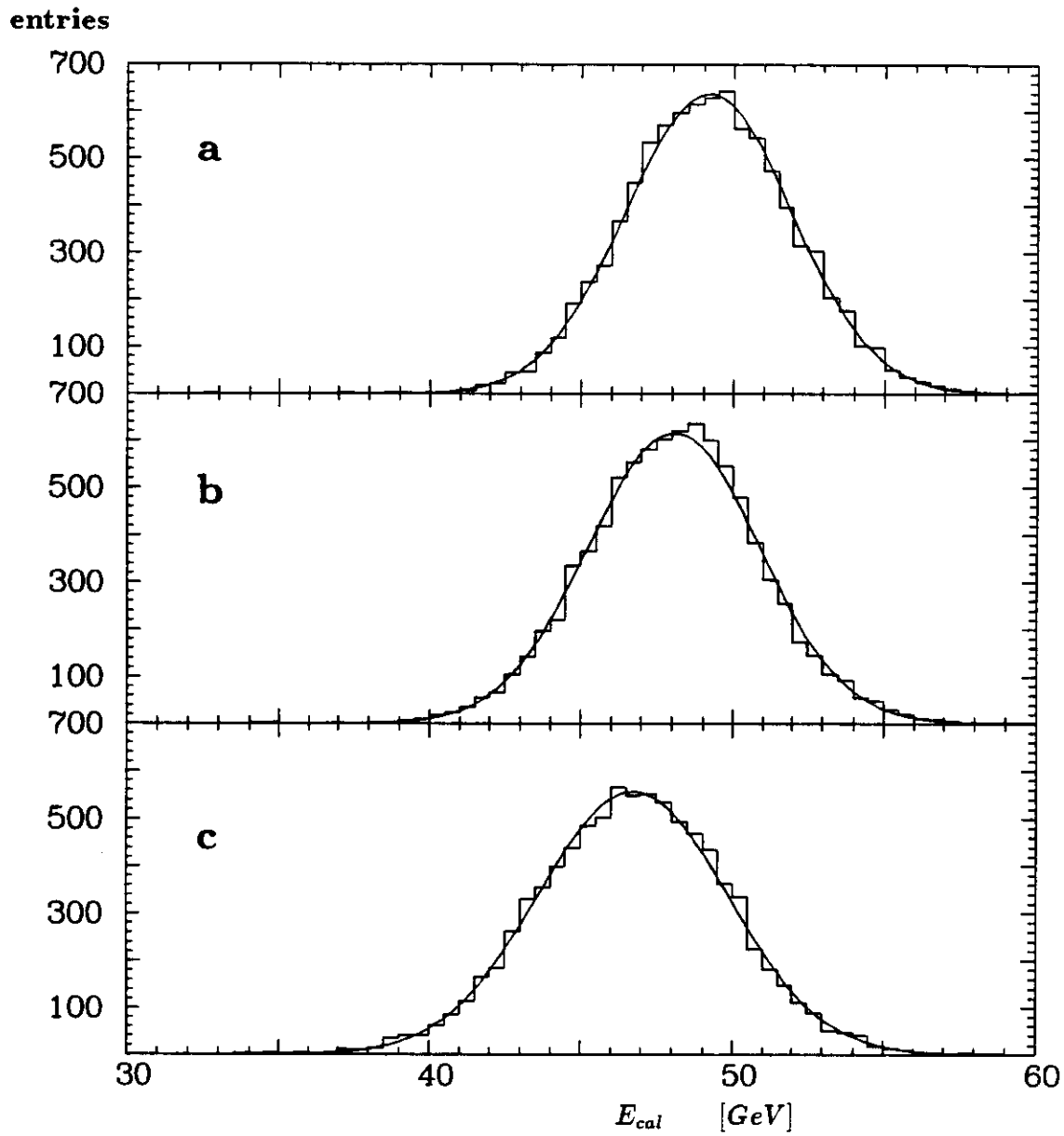
Figure 3.16: Energy distribution for 50 GeV jets with 0 cm (a), 4 cm (b) and 10 cm (c) aluminum absorber in front of the calorimeter.

energy $[GeV]$	Al $[cm]$	$\overline{E}_{cal}$ $[GeV]$	$\sigma_{E_{cal}}$ $[GeV]$	$\sigma_{E_{cal}}/\overline{E}_{cal}$ $[\%]$
50	0	49.19 ±.03	2.73 ±.02	5.56 ±.04
	4	48.07 ±.03	2.83 ±.02	5.89 ±.05
	10	46.71 ±.03	3.12 ±.02	6.68 ±.05
75	0	73.47 ±.06	3.56 ±.04	4.85 ±.06
	4	72.30 ±.04	3.63 ±.03	5.02 ±.04
	10	70.22 ±.03	3.82 ±.03	5.44 ±.04
100	0	99.34 ±.05	4.31 ±.03	4.34 ±.03
	4	98.01 ±.05	4.43 ±.03	4.52 ±.03
	10	95.80 ±.04	4.75 ±.03	4.95 ±.03

Table 3.8: Mean energy $\overline{E}_{cal}$ and resolution $\sigma_{E_{cal}}/\overline{E}_{cal}$ for jets with aluminum in front of the calorimeter.

The relative energy difference $\Delta E/E$ for jets, is given by

$$\frac{\Delta E}{E} = \frac{\overline{E}_{cal}(d) - \overline{E}_{cal}(0)}{\overline{E}_{cal}(0)}$$

where $\overline{E}_{cal}(d)$ is the mean calorimeter energy for 4 cm respectively 10 cm thick aluminum plates in front of the calorimeter and $\overline{E}_{cal}(0)$ is the mean energy with no aluminum absorber in front of the calorimeter. In fig.3.17 the relative energy loss is shown for different values of aluminum thicknesses.

The change in the relative energy resolution is given by

$$\frac{\Delta R}{R} = \frac{(\sigma_E/E)(d) - (\sigma_E/E)(0)}{(\sigma_E/E)(0)}$$

where $\sigma_E/E(d)$ is the energy resolution for 4 cm respectively 10 cm aluminum in front of the calorimeter and $\sigma_E/E(0)$ is the energy resolution with no aluminum absorber in front of the calorimeter. In fig.3.18 the relative energy resolution is shown. For 4 cm aluminum the resolution gets worse by approximately 4 % . For 10 cm aluminum the resolution gets worse by 13% but for 50 GeV the resolution is worse by 20 %.

$(E(d) - E(0))/E(0)$

$(E(d) - E(0))/E(0)$
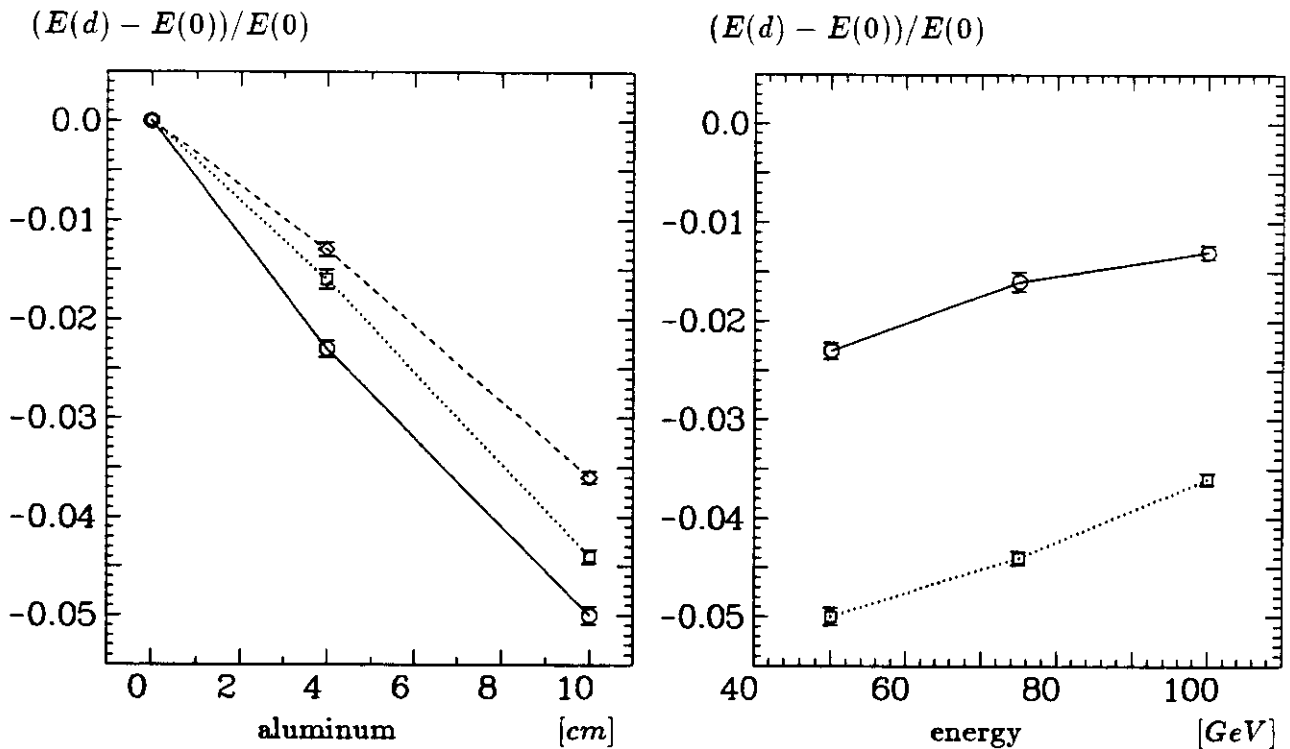
Figure 3.17: Relative energy difference versus Al thickness (left) for 50 GeV (solid), 75 GeV (dotted) and 100 GeV (dashed) jet energy. The right fig. shows the energy loss versus the jet energy for 4 cm (circles) and 10 cm (squares) aluminum plates.

$\Delta R/R$

$\Delta R/R$
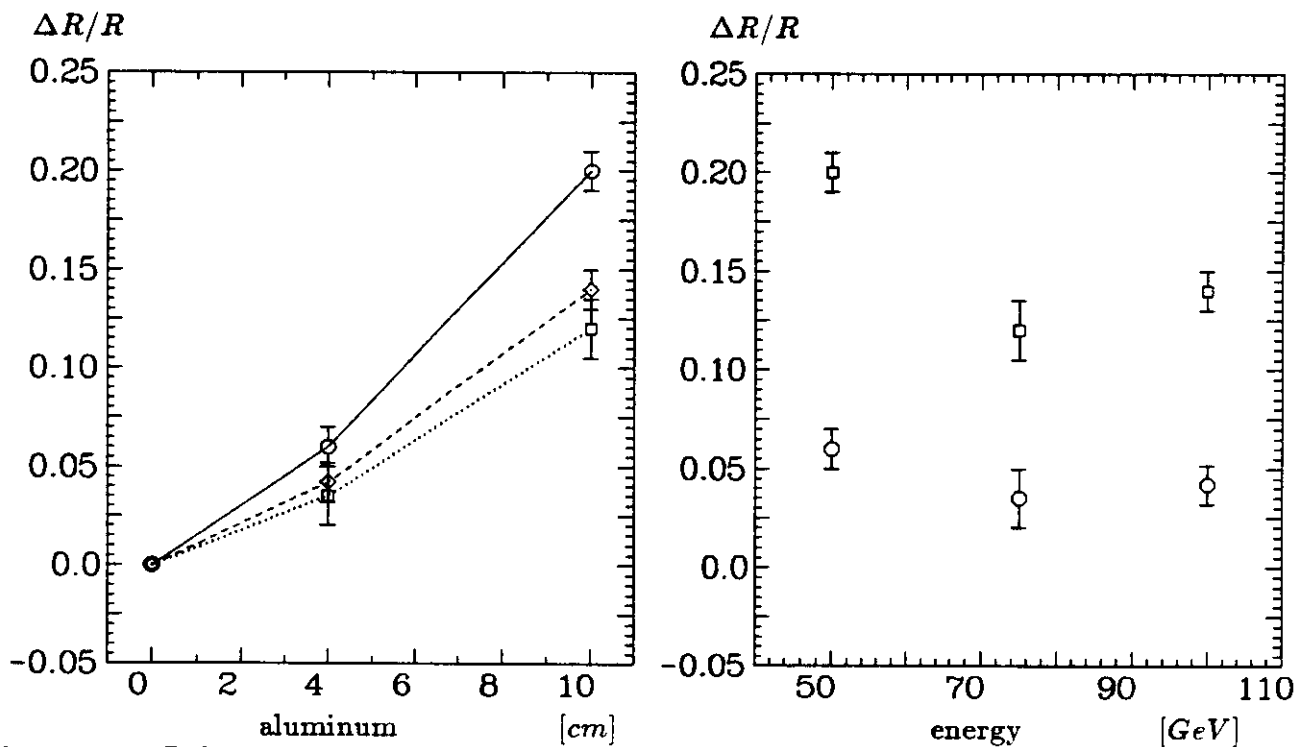
Figure 3.18: Relative energy resolution versus Al thickness (left) for 50 GeV (solid), 75 GeV (dotted) and 100 GeV (dashed). The right figure shows the relative resolution versus the jet energy for 4 cm (circles) and 10 cm aluminum (squares) plates.

3.4.1 Corrections for Energy Loss

From fig.3.17 and 3.18 it is apparent that material in front of the calorimeter leads to a loss of energy in the calorimeter and to a deterioration of the energy resolution. The idea is to correct the energy with the charged multiplicity measured in front and behind the absorber plates. First one has to understand the energy loss mechanisms. The energy loss in the passive material is dominated by the following physical mechanisms.

- ionization loss of charged particles

- inelastic hadronic interaction

The mean ionization loss of a minimum ionizing particle in aluminum is 4.37 MeV/cm [6]. The mean ionization loss of 11 charged pions has been calculated by a Monte Carlo simulation. For 4 (10) cm aluminum plates the energy loss is approximately 0.25 (0.56) GeV. The fluctuations of the energy loss is 0.06 (0.13) GeV for 4 (10) cm aluminum plates.

For energies above the critical energy (51 MeV for aluminum) electrons, positrons and photons will initiate an electromagnetic cascade. The dominant physical processes are bremsstrahlung and pair production. The energy loss of the electromagnetic cascade within the aluminum is due to the ionization loss of the charged particles. Therefore the charged multiplicity behind the aluminum is correlated to the energy loss. The fraction of soft photons produced within the cascade is small because the thickness of the aluminum is less than 1.1 X_0 and the shower is dominated by high energy particles at these evolution stage. Therefore energy losses by compton scattering or photo effect can be neglected.

Hadrons can inelasticly interact with an aluminum nucleus. Part of the energy is lost by nuclear binding energy, excitation and by ionization of charged particles. The energy loss within the aluminum is as in the case of an electromagnetic cascade correlated with the charged multiplicity behind the aluminum. For 0.25λ and 0.1λ thick material the probability for an interaction is 22 % and 10 % respectively. For a mean charged multiplicity of 11 particles the probability for at least one interaction is 95 % for 0.25λ and 30 % for 0.1λ.

The charged multiplicity was measured in front of the aluminum plates by the trigger counter N_{trig} and behind the aluminum plates by the presampler N_{pres}. The increase of the charged multiplicity by the aluminum absorber is given by:

$$\Delta N = N_{pres} - N_{trig}$$

The correlation of N_{trig} and ΔN is shown in fig.3.19. For less than 17 particles the curve is flat and almost 80 % of the events are within this range. For increasing multiplicity the curve is decreasing and ΔN gets negative. This happens because a low energy particle can fake high multiplicity in the trigger counter and is absorbed either in the trigger itself or in the following aluminum.

In fig.3.20 - 3.22 the energy loss versus the charged multiplicity N_{trig}, N_{pres} and ΔN respectively is shown. The energy loss E_{loss} is the difference between the energy $E_{cal}(d)$ of events recorded in the calorimeter and the mean energy for jets $\overline{E}_{cal}(0)$ recorded without aluminum absorber in front of the calorimeter. d is the absorber thickness.

$$E_{loss} = E_{cal}(d) - \overline{E}_{cal}(0)$$

For all the curves shown, the energy loss increases with increasing charge multiplicity. However with increasing charged multiplicity the slope of the curves decreases and converges to
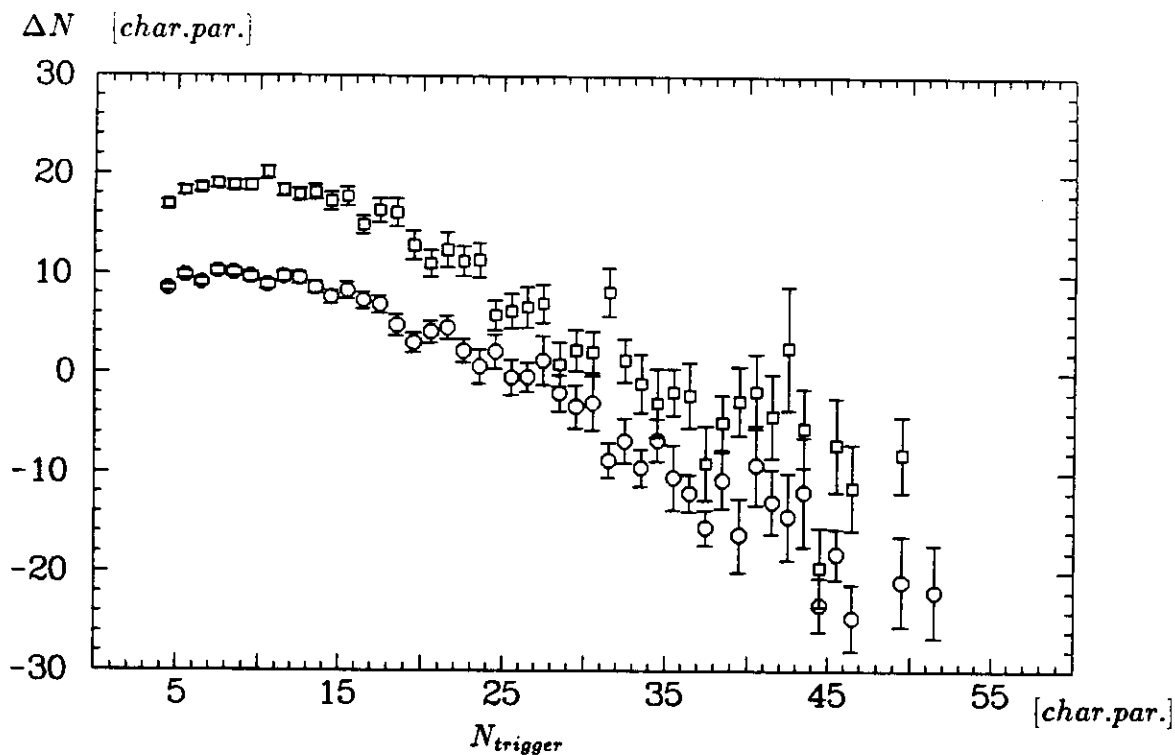
Figure 3.19: Charged multiplicity $N_{trigger}$ versus $\Delta N = N_{pres} - N_{trigger}$ for 50 GeV jets and 4cm (circles) respectively 10cm (squares) aluminum plates in front of the calorimeter.

Figure 3.20: Energy loss versus charged multiplicity N_{trig} for 4 (circles) and 10 (squares) cm aluminum plates, 50 GeV jets.

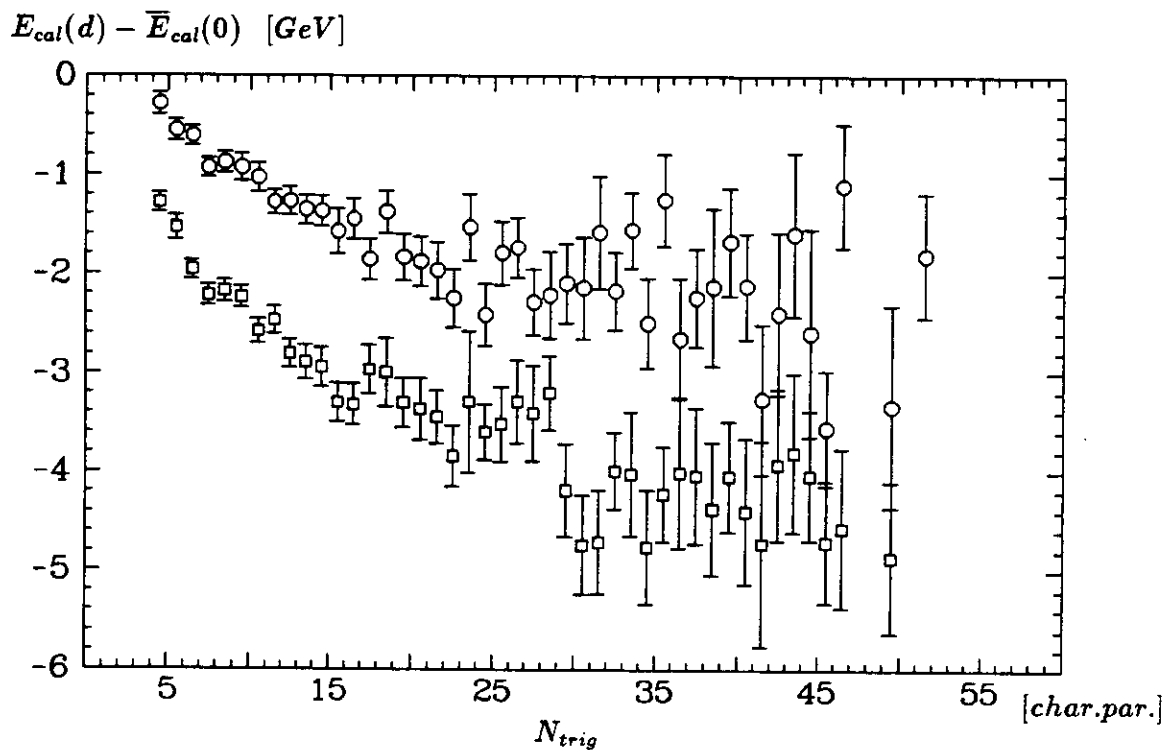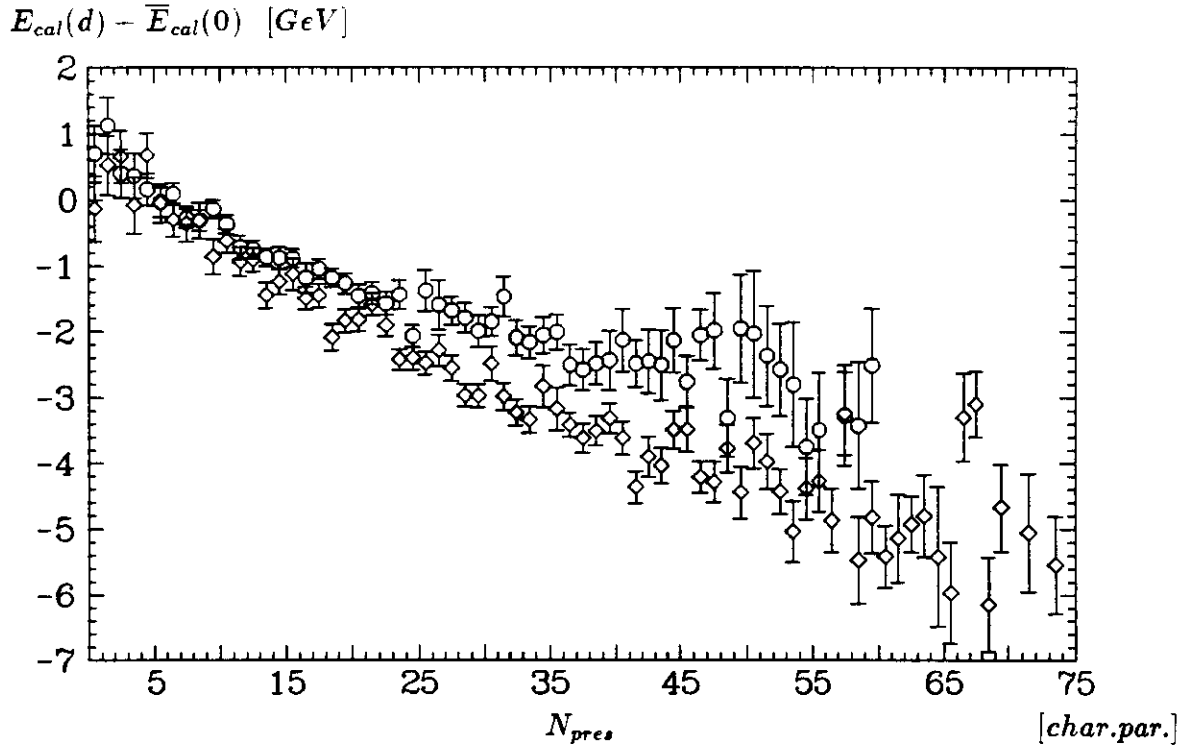Figure 3.21: Energy loss versus charged multiplicity N_{pres} for 4 (circles) and 10 (diamonds) cm aluminum plates, 50 GeV jets.
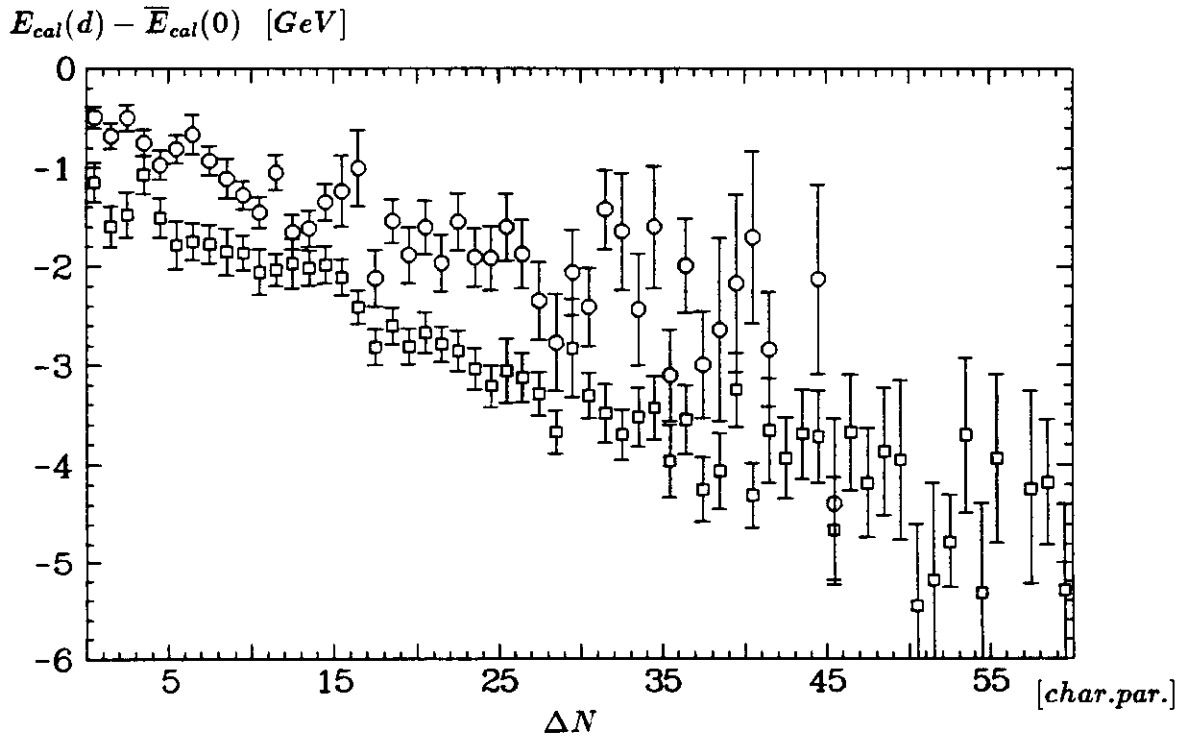

Figure 3.22: Energy loss versus charged multiplicity $\Delta N = N_{pres} - N_{trig}$ for 4 (circles) and 10 (squares) cm aluminum plates, 50 GeV jets.

zero. This effect is most pronounced for the correlation with N_{trig}. For the correlation with N_{pres} it is apparent that the curve shape is independent of the aluminum plate thickness.

The energy correction was done by assuming a linear dependence on the charged multiplicity N_{trig}

$$E^{corr} = E_{cal} + \varepsilon N_{trig} \qquad (3.1)$$

and on N_{pres} respectively.

$$E^{corr} = E_{cal} + \vartheta N_{pres} \qquad (3.2)$$

The parameters ε and ϑ were fixed so that the mean energy response for jets with aluminum equaled those for jets without aluminum in front of the calorimeter.

$$\frac{\overline{E}_{cal}(0)}{\overline{E}_{cal}^{corr}(d)} = 1 \qquad (3.3)$$

In fig.3.23 the results of the correction parameter ε and ϑ are shown and summarized in table 3.9. The errors were calculated so that the ratio (3.3) which determines the correction parameter is not equal one but ± 0.5 % off. This is the order of the systematic errors. The error on the correction parameter is large because the difference of the corrected energy and measured energy is only a few per cent. From equation 3.1 the relative error is

$$\frac{\Delta \varepsilon}{\varepsilon} = \frac{\Delta \overline{E}_{cor}}{\overline{E}_{cor}} \frac{1}{\overline{E}_{cal}/\overline{E}_{cor} - 1}$$

The second factor on the right side ranges from 20 - 100. Therefore the relative error on the correction parameter is 20 - 100 times larger than the relative error on the mean corrected energy. The same result for $\Delta \varepsilon / \varepsilon$ is obtained if the the relative error on the measured calorimeter energy is considered.

para.	AL	energy			mean
	[cm]	50 GeV	75 GeV	100 GeV	[GeV/char.par.]
ε	4	0.089 ±0.020	0.088 ±0.028	0.093 ±0.035	0.090 ±0.028
ε	10	0.202 ±0.021	0.261 ±0.032	0.262 ±0.039	0.242 ±0.031
ϑ	4	0.057 ±0.013	0.054 ±0.017	0.056 ±0.021	0.056 ±0.031
ϑ	10	0.088 ±0.009	0.100 ±0.011	0.096 ±0.013	0.095 ±0.010

Table 3.9: Correction parameters for the correction function $E^{corr} = E_{cal} + \varepsilon N_{trig}$ and $E^{corr} = E_{cal} + \vartheta N_{pres}$ respectively.

The correction parameters ε and ϑ are independent of the energy, except that the data point for 50 GeV and 10 cm aluminum absorber is a little bit to low for both parameters. These two points are not independent because they were determined by the same events. If, for example the calorimeter energy was systematicly measured to large, both correction parameter values are systematicly to small. However within the errors the parameter values agree with those for 75 GeV and 100 GeV jets. The correction parameter ε increases with aluminum thickness by a factor of 2.7 ±0.6. The correction parameter ϑ, for the correction with the charged multiplicity behind the aluminum plates increases by a factor of 1.7 ±0.06, going from 4 to 10 cm aluminum thickness.

The correlation between the energy loss and the charged multiplicity is not perfectly linear. Therefore the correction parameter ε and ϑ may dependent on the charged multiplicity

Figure 3.23: Correction parameter ε (left) and ϑ (right). The circles (squares) are the results for 4 (10) cm aluminum.

N_{trig}. This dependence was tested by selecting events within a given range of the charged multiplicity N_{trig} and calculate ε and ϑ for these events. Fig.3.24 shows the relative deviation $\Delta\varepsilon/\varepsilon$ and $\Delta\vartheta/\vartheta$ where $\Delta\varepsilon$ is the difference between the correction with a selection on N_{trig} and the correction parameter ε where no selection on N_{trig} was applied. The correction parameter ε depends on N_{trig}. This reflects the nonlinearity in particular at low values. In contrary to this the correction parameter ϑ varies only slightly with N_{trig}.

The energy correction uses only one parameter which is fixed by the correct mean response. Therefore the resolution can not independently be maximized. In fig.3.25 the resolution versus ε and ϑ is shown. ε_0 and ϑ_0 are the parameter values where the correct mean response, defined by equation 3.3 is achieved. The correct mean response does not match with the maximum in the resolution for both corrections although for the correction with N_{pre} the maximum is almost achieved.

If the resolution should be maximized at the same time a second parameter has to be introduced. The correction now reads:

$$E^{corr} = E_{cal} + \varrho N_{trig} + \varphi \Delta N \tag{3.4}$$

The two conditions to fix both parameters are now the correct mean response

$$\frac{\overline{E}^{corr}(d)}{\overline{E}_{cal}(0)} = 1 \tag{3.5}$$

and maximization of the energy resolution

$$\frac{\sigma_E}{E} \to minimum.$$
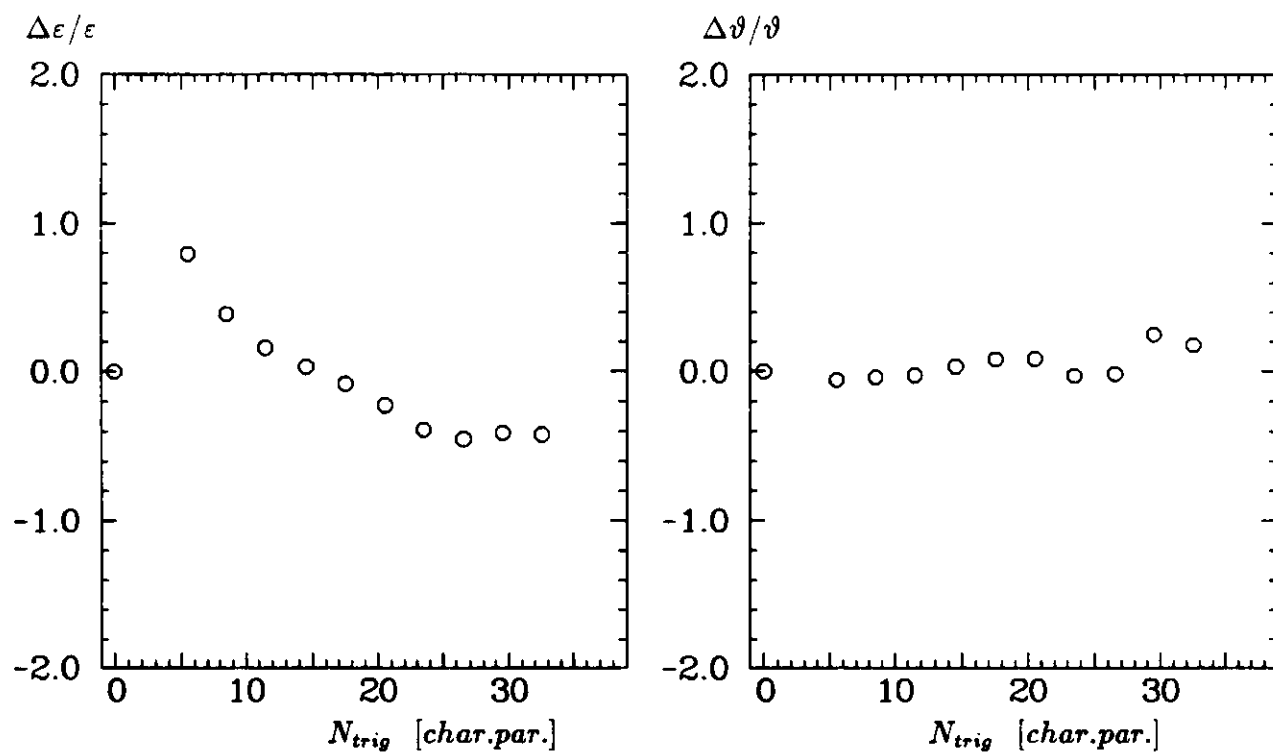
Figure 3.24: Change of ε (left) and ϑ (right) versus N_{trig}.
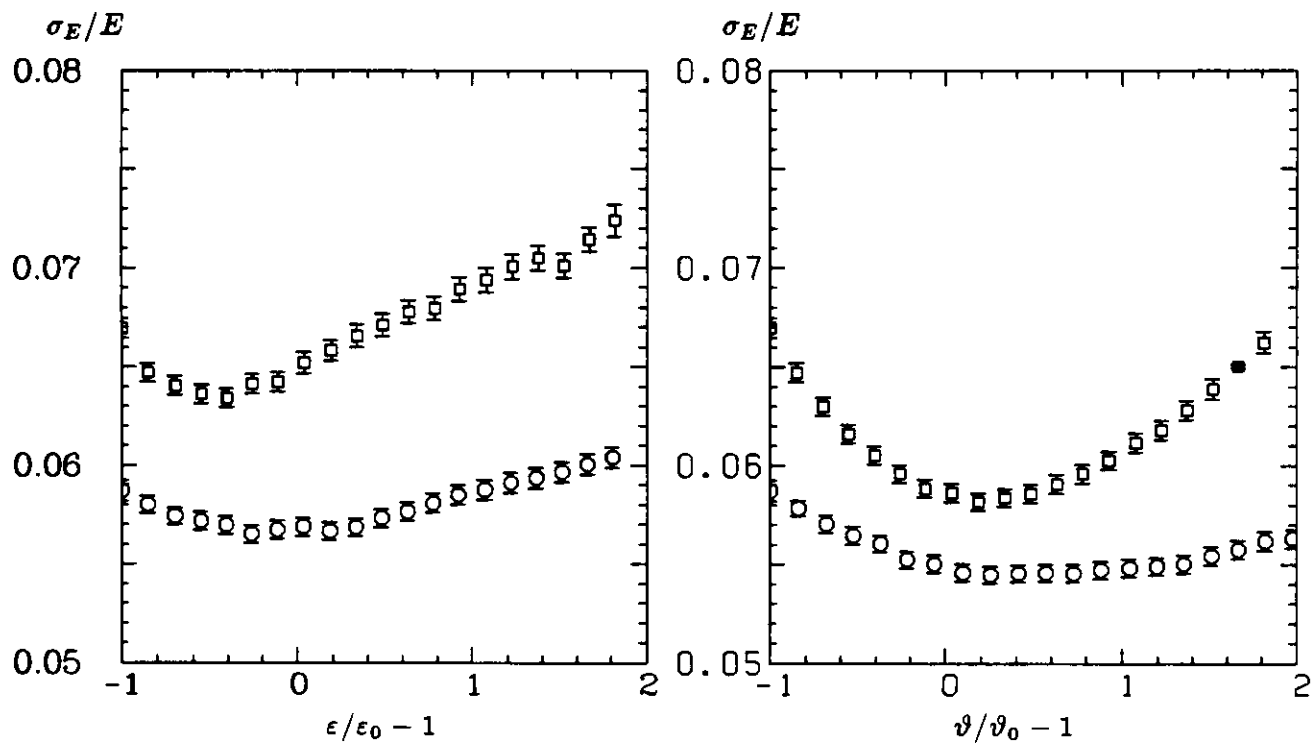
Figure 3.25: Energy resolution σ_E/E versus the correction parameters ε (left) and ϑ (right). The circles (squares) are for 4 (10) cm aluminum plates.

Because the mean energy is fixed by the first condition the second condition is equivalent by minimizing the σ_E value. In fig.3.26 the results for ϱ and φ are shown. The errors are again due to a change of equation 3.5 by ± 0.5 %.

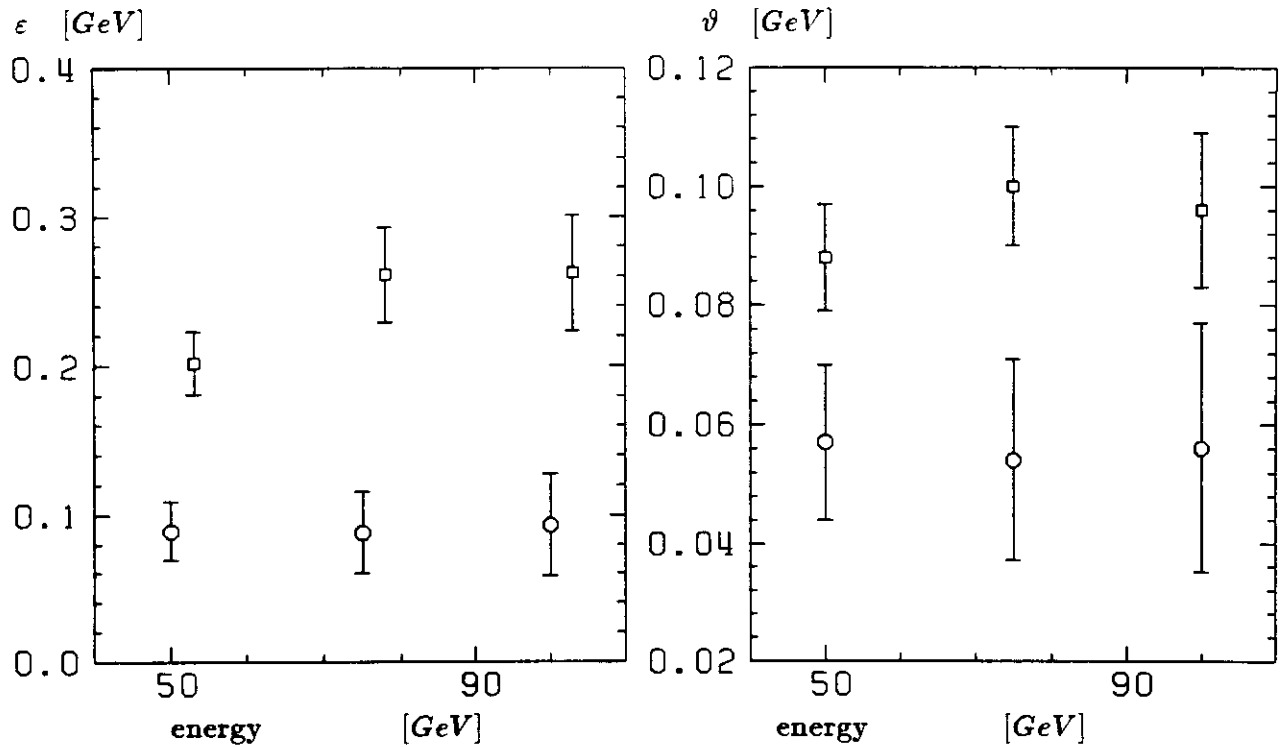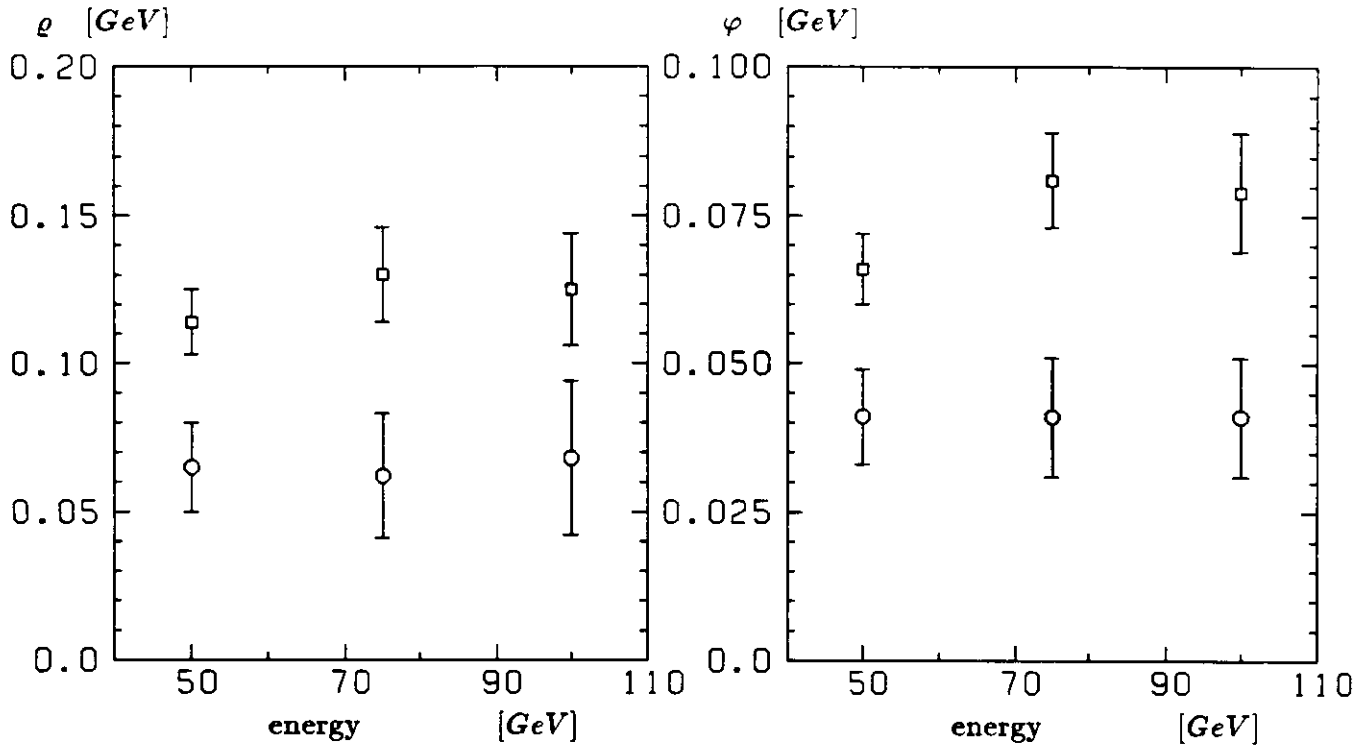
Figure 3.26: Correction parameter ϱ (left) and φ (right). The circles (squares) are the results for 4 (10) cm aluminum.

energy	4 cm Al		10 cm Al	
	ϱ	φ	ϱ	φ
[GeV]	[GeV/charged particles]			
50	0.065 $\pm$0.015	0.041 $\pm$0.008	0.114 $\pm$0.011	0.066 $\pm$0.006
75	0.062 $\pm$0.021	0.041 $\pm$0.010	0.130 $\pm$0.016	0.081 $\pm$0.008
100	0.068 $\pm$0.026	0.041 $\pm$0.010	0.125 $\pm$0.019	0.079 $\pm$0.010
mean	0.065 $\pm$0.021	0.041 $\pm$0.009	0.123 $\pm$0.015	0.075 $\pm$0.008

Table 3.10: Correction parameters for the correction function $E^{corr} = E_{cal} + \varrho N_{trigger} + \varphi \Delta N$

The correction parameters are independent of the initial jet energy. The ratio of the parameter ϱ for 4 and 10 cm aluminum thickness is 1.9 $\pm$0.7. The same ratio for the parameter φ is 1.8 $\pm$0.5.

The variation of the two parameters when events with a certain charged multiplicity N_{trig} are selected is shown in fig.3.27. The variation of the two parameter are in the order of 10 %. They are insensitive to the charged multiplicity which means that the correlation of the energy loss with N_{trig} and ΔN is well described by a linear function.

The resolution achieved with the different correction methods is shown in fig.3.28. The resolution for the measurement with no aluminum in front of the calorimeter has also been corrected with N_{trig}. With the correction function $E^{cor} = E_{cal} + \epsilon N_{trig}$ the parameter ϵ was

$\Delta\varrho/\varrho, \Delta\varphi/\varphi$
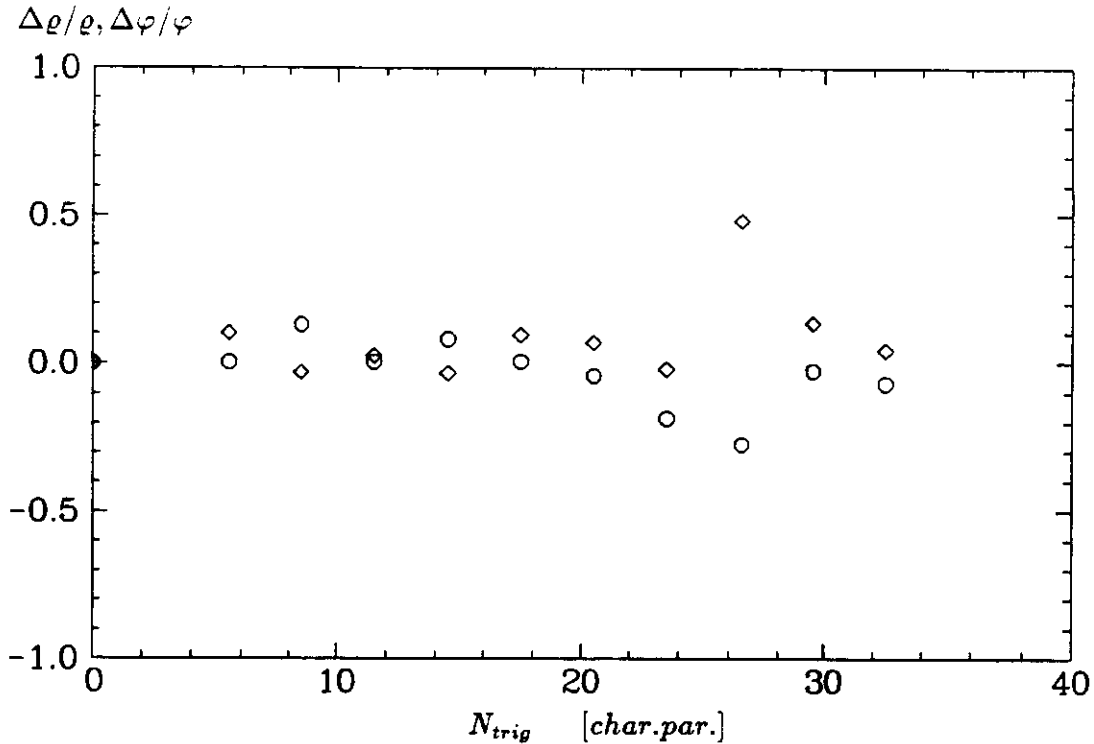
Figure 3.27: Relative change of the correction parameter ϱ (circles) and φ (squares) when the events were selected by $N_{trig} - \Delta N < N_{trig} < N_{trig} + \Delta N$ where ΔN is a small interval. 50 GeV jets 10 cm aluminum absorber.

determined, so that the energy resolution σ_E/E^{corr} is maximized. The resolution improves due to this correction by 2 % which means it is a very small correction.

From fig.3.28 it is apparent that the correction with the charged multiplicity in front of the absorber improves the resolution only slightly about 3 %. On the other hand with the corrections by the charged multiplicity behind the absorber, it is achieved that the resolution improves so that it is close to the resolution without an absorber. It is also apparent that for 50 GeV the improvement is less than that achieved for 75 GeV and 100 GeV jets.

The gain in resolution, if the corrections were done with both multiplicities, is very small compared to resolution achieved with the presampler corrections. Therefore, at least for the jets measured by this experiment, it is not important to measure the charged multiplicity in front of the aluminum.

The improvement in resolution due to the trigger counters corrections is due to the fact that with the trigger counter it is not possible to decide whether an interaction in the absorber has taken place or not. All events with the same value of N_{trig} will be corrected by the same energy loss, independent of the actual energy loss for an event. In contrast to this is the correction with the presampler. If an interaction takes place the charged multiplicity N_{pres} of an event is increased and therefore the energy correction ϑN_{pres} is larger than those without an interaction.

$(\sigma_E/E)/(\sigma_E/E)_0$
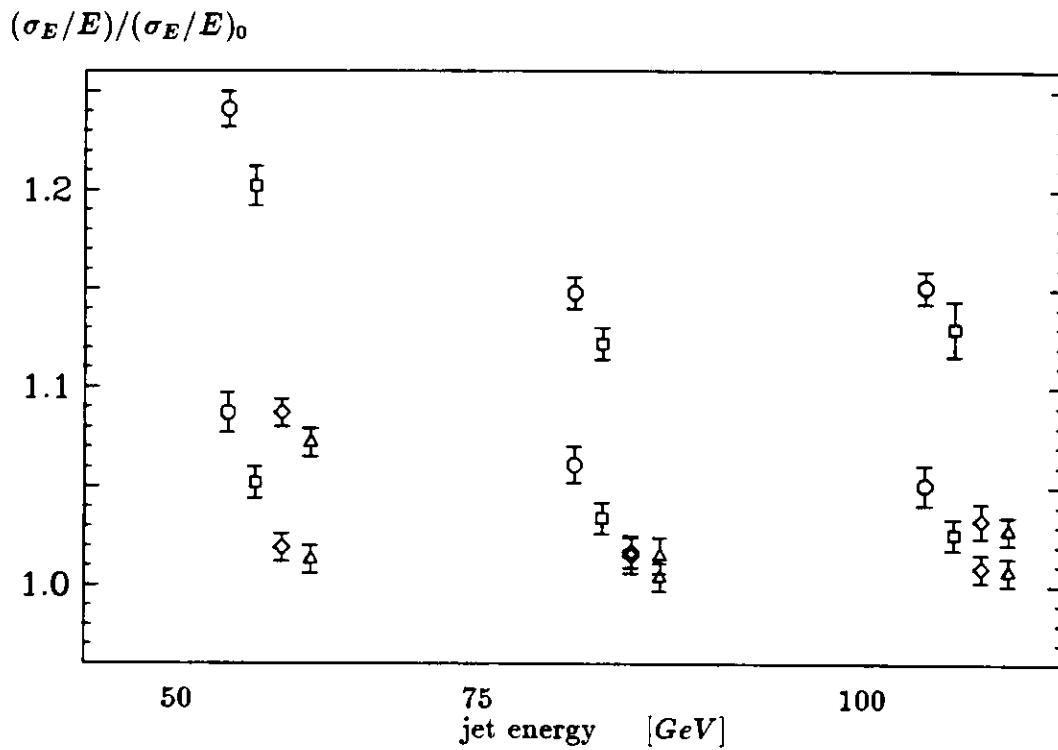
Figure 3.28: Resolution σ_E/E, normalized by the resolution $(\sigma_E/E)_0$ without an aluminum absorber, for different correction methods: No correction (circles), by N_{trig} (squares), by N_{pre} (diamonds) and by both counters (triangle). The lower (higher) values are for 4 (10) cm aluminum plates.

Chapter 4

Monte Carlo Calculations

Monte Carlo calculations were performed on the one hand to get a better understanding of the experimental test results and on the other hand to test the Monte Carlo simulation of the ZEUS calorimeter. The measured results in particular the energy loss corrections can not simply be applied to the jets measured in ZEUS. Therefore the Monte Carlo has to provide the correction factors. They will be much more reliable if the Monte Carlo simulation reproduces the test beam results.

The Monte Carlo was performed in two steps. In the first step (INT-MC) the interaction trigger consisting of the trigger counters, veto counters, target and the pion-target interaction was simulated. The particle tracks created in this simulation were the input for the second step (T2-MC), the simulation of the calorimeter, presampler and the passive material in front of the calorimeter.

4.1 Interaction Trigger Simulation INT-MC

4.1.1 GEANT

The GEANT program package [11] version 3.11 has been used for the simulation of the interaction trigger setup. In GEANT a detector geometry is described by volumes filled with the different materials of the detector. The event simulation is done by tracking particles through the different volumes. Tracking a particle means, that the spatial coordinates and the momentum are calculated for successive steps, defining the trajectory of a particle. The step size and the energy loss for a particle depends on the physical process which takes place. The program distinguishes continuous (ionization loss, multiple scattering) and discrete processes (decay, electromagnetic or hadronic interaction). The probability of a particular process is determined by its cross-section and is evaluated at the begining of a step. Hadronic interactions are simulated by the GEISHA package [9]. Secondary particles created in interactions are stored and later on they are also tracked.

After each tracking step the user has access to the information of the step. The information of the energy loss, number of secondary particles generated, if the particle is leaving the volume and much more information can be obtained and stored for further applications.

4.1.2 INT-MC

The geometrical description of the interaction trigger is a realistic description of the experimental setup.

The trigger- and veto scintillation counters were modelled according to the geometrical dimensions used in the experiment and described in Chapter 2.2.1. For the lead glass counters a simplified description was used. The three trapezoidal counters forming the upper plane (L_1, L_2, L_3) were described by one counter with a box shape and dimensions of $30 \times 10 \times 30$ cm^3. A corresponding simplification was used for the three counters forming the upper plane (L_6, L_7, L_8). The two lead glass counters (L_4, L_5) which are between the two planes were modelled by a box shape of $10 \times 10 \times 30$ cm^3. The positions of the counters and target corresponds to those in the experimental set up.

The ionization loss in the trigger and veto counters was recorded during the tracking of the particles. The ionization loss was summed for each event and normalized by the mean ionization loss of a 100 GeV pion. The mean ionization loss of a 100 GeV pion was determined by a Monte Carlo simulation for 2 mm, 4 mm thick scintillator plates and for lead glass plates of 10 cm thickness. The mean was determined by summing over all events (≈ 5000). After an event was tracked it was stored on disk, if the following trigger conditions were fulfilled:

$$N_{T_i} \leq 0.33$$

$$N_{T_5} \leq 2.0$$

where i stands for the four trigger counters. The mean ionization loss of a pion is equal to one. These trigger conditions correspond to the conditions used in the experiment. Neither noise nor nonuniformities of the individual counters were considered.

If an event sets the trigger, the particle tracks which left the interaction trigger setup were stored. For each event global informations were recorded like the signal in the five trigger counters, the signal of the veto scintillation and lead glass counters, the number of tracks leaving the setup and the energy loss in the target. For each particle track the particle type, absolute momentum, energy, position before leaving the setup, and the polar and azimuthal angle were recorded.

4.2 Calorimeter Monte Carlo T2

The simulation of the calorimeter was done with the ZEUS trigger Monte Carlo version T2 [12]. It is based on the GEANT program package version 3.13. In addition ZEUS specific simulation routines are implemented. The T2 Monte Carlo is a full description of the components of the ZEUS detector. The individual components can be switched on or off via data cards. If a component is switched off it is neither read out nor is its material simulated.

For the calorimeter simulation different options for the tracking medium and the simulation of the physical processes are possible. One option for the tracking medium of the calorimeter is a detailed description of the alternating scintillator and uranium plates. Moreover the uranium plates are clad with steel foil. Due to the frequent change of the tracking medium this description is computing time consuming. A second option for the tracking medium is the porridge structure of the calorimeter. It consists of only one material, a mixture of scintillator, uranium and steel with the corresponding weights. This option was chosen for the simulation.

Another choice concerns the simulation of the physical processes. So called shower terminators are used to reduce the computing time spent for the tracking of low energy particles from electromagnetic cascades and low energy neutrons mainly from evaporation processes. The idea for the electromagnetic shower terminator is that only a fraction of the low energy particles are tracked. The energy deposition of the tracked particles are weighted by the energy of the not tracked particles. The idea of the neutron shower terminator is that neutrons with $E_{kin} < 50$ MeV are not tracked but their energy is uniformly distributed at the creation point of a neutron. The advantage of the shower terminators is the significantly reduced computing time. A detailed description of the trigger Monte Carlo and the shower terminators can be found in [12,13].

The T2 Monte Carlo has been tuned with the results of test beam data from 1 - 100 GeV electrons and pions respectively. The mean response and energy resolution is well described by the Monte Carlo. In particular the deviation of the e/h-ratio from 1 for hadron energies less than 5 GeV is described correctly. Differences are found in the lateral and longitudinal shower dimension. The Monte Carlo underestimates the width and length of a shower. The nonuniformities occuring close to the crack between two adjacent modules and the gap between two sections within the same module are also not correctly described.

In the T2 Monte Carlo the complete forward calorimeter of ZEUS is simulated. It consists of 23 modules in the horizontal direction of which the 11 central modules are 23 towers high. Module 12 tower Nr. 12 corresponds to the beam pipe and is not filled with the calorimeter material. The incident beam position was chosen to be in module 12, tower 15 and 2.5 cm above the tower center. In fig.4.1 a view of the overall calorimeter and the matrix which corresponds to the prototype calorimeter size is shown. This 4 × 4 matrix corresponds to tower 13 - 16 of module 11 - 14.
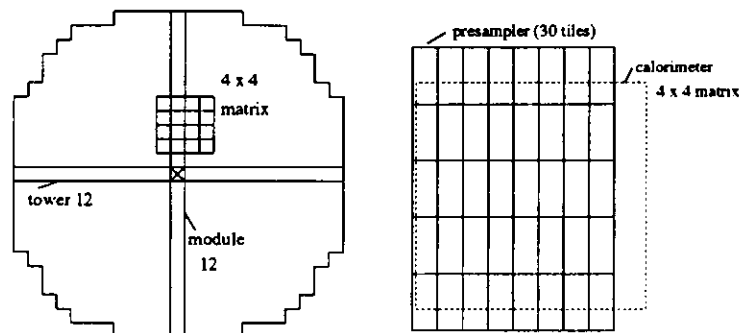
Figure 4.1: Position of the prototype calorimeter modules in the FCAL-calorimeter (left). Position of the presampler counters in the simulation is indicated on the right.

In the later analysis E_{cal} is the energy deposited in this 4 × 4 tower matrix. The energy which is deposited outside of this matrix is called E_{out}. The front face of the calorimeter is at z = 220 cm. The Be-target is placed at x=0.0 cm, y=62.5 cm and z=178 cm thus 42 cm in front of the calorimeter.

The passive material and the presampler were implemented in the T2 Monte Carlo. Aluminum was used as passive material. The lateral dimension of the aluminum was 30 × 50 cm². The rear side of the aluminum plate was 2 cm in front of the calorimeter. The simula-

tion was performed with aluminum plates of 4 and 10 cm thickness, thus the same thickness as used for the test beam measurements.

The presampler was divided into 30 tiles each $8 \times 20 \times 0.6$ cm^3. These plates were arranged into a 6×5 matrix corresponding to 48×100 cm^2(the presampler used for the measurements was 48×80 cm^2). The position of the presampler relative to the calorimeter is shown in figure 4.1. The ionization loss in each of the tiles was summed over an event and normalized by the mean ionization loss of a 100 GeV pion. The total presampler signal was the sum of the signals in all 30 tiles. No nonuniformities and attenuation of the scintillation light traveling towards the PMT were considered.

4.3   Jet Properties

In the following sections properties of the jet events are presented. The results of the INT-MC for the multiplicity, energy spectrum and jet energy are discussed.

4.3.1   Multiplicities

In fig.4.2 the number of particle tracks per event leaving the interaction trigger setup is shown. The mean number of tracks is 43.9 for 50 GeV and increases to 50.0 at 100 GeV. The r.m.s.
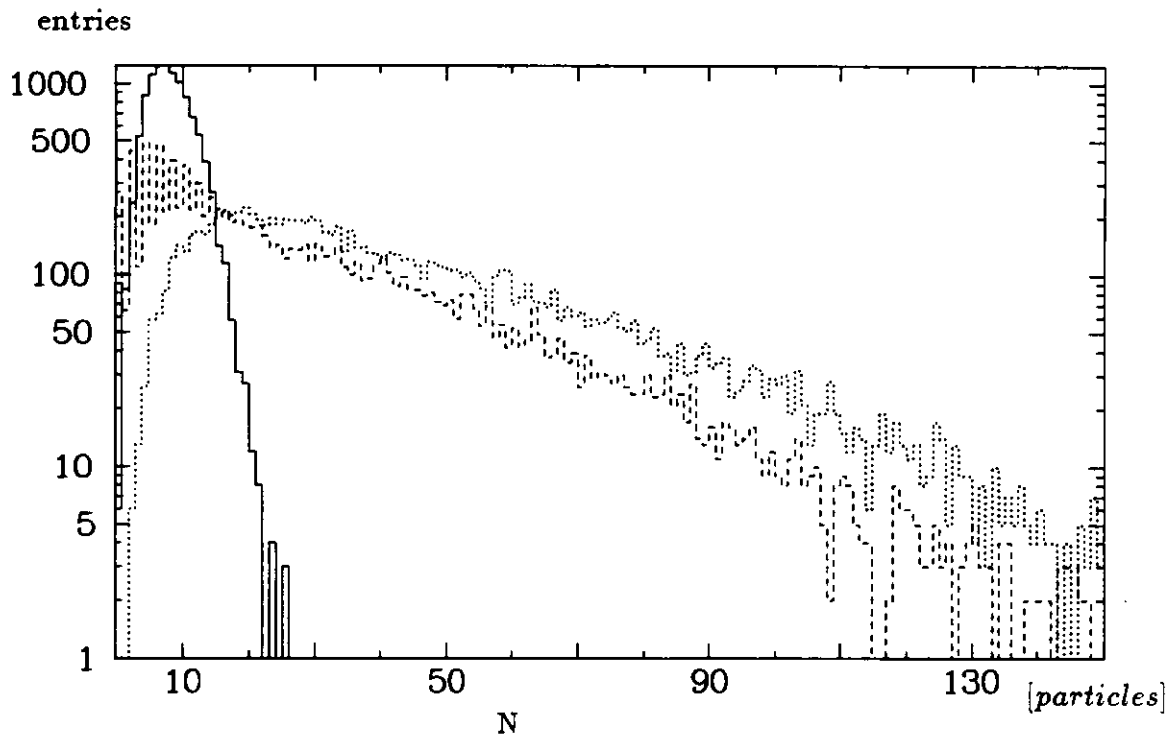
Figure 4.2: Multiplicity distribution for 50 GeV jets. Results for all particles (dotted), for photons (dashed) and for charged pions (solid). Calculated by INT-MC .

of these distributions is 30.9 particles for 50 GeV and 32.8 particles for 100 GeV respectively. Almost 63 % of the track vertices are located within the target. The remaining 37 % are located in the trigger counter T_5 (28 %) and in the veto system (9 %).

The average multiplicities of the different particle types is shown in table 4.1. Photons are

particle type	N [$particles$] $E_{beam} = 50\text{GeV}$	75GeV	100GeV
γ	28.5 (26.5)	33.5 (29.0)	32.3 (27.8)
$e^{\pm}$	2.0 (2.5)	2.3 (2.7)	2.2 (2.7)
$\pi^{\pm}$	7.9 (3.4)	9.4 (4.1)	9.4 (4.0)
n	2.5 (1.8)	2.8 (2.0)	2.7 (2.0)
p	1.5 (1.3)	1.7 (1.5)	1.6 (1.4)
ν	1.2 (2.0)	1.4 (2.2)	1.2 (2.0)
$\mu^{\pm}$	0.1 (0.2)	0.1 (0.3)	0.1 (0.2)
rest	0.4 (0.7)	0.5 (0.7)	0.5 (0.8)

Table 4.1: Mean multiplicity $\overline{N}$ per event. In brackets the r.m.s. is shown.

abundant. Most of these photons are released by nuclei excited by the nuclear interactions. The energy of these photons is soft ranging from a few MeV up to a few hundred MeV. Photons are also produced by decays of neutral pions. As the mean multiplicity for neutral pions is approximately one third of those for charged pions, about 7.9 photons are produced due to the decays of π^0 per event. The energy of these photons is up to a few tens of GeV.

On the average 7.9 charged pions are produced corresponding to 17 % of all particles. The pions are created by the spallation process due to the interaction of the incident beam pion with the beryllium nucleus.

Four nucleons, on the average, were released from a nucleus and left the target. The particles called 'rest' are heavy mesons. About 1.5 neutrinos are created per event. The energy of a neutrino is lost because it does not interact in the calorimeter. However the energy carried by these tracks is less than 0.2 % and can be neglected.

The charged multiplicity is measured by the trigger counters. The signal in the trigger counter N_{trig} is due to the ionization loss of charged particles. The energy loss of photons can be neglected. The energy loss of neutrons is very small, except for ≈ 0.9 % of the events where a signal up to 24 times the signal of a mip was observed.

The charged multiplicity N_{trig} is measured by the energy deposited in the trigger counters and normalizied by the mean energy deposited by a 100 GeV charged pion. For a jet event a fraction of the charged particles are non relativistic and these particles deposit more energy in the trigger counters than high energy charged pions. Therefore the measured charged multiplicity N_{trig} is, on the average, larger than the number of charged particles N_{char} that actually traverses the trigger counters. The ratio

$$N_{ratio} = \frac{N_{trig}}{N_{char}}$$

is shown in fig.4.3.

The mean value for N_{ratio} is 1.32 with a standard deviation of 1. A tail towards high values is observed. The ratio N_{ratio} increases with increasing N_{trig}, because the mean particle energy is decreasing and the ionization loss is increasing.

The charged multiplicity measurement by N_{trig} for the Monte Carlo simulation and the experimental result are shown in fig.4.4 for 50 GeV jets. The agreement is quite good except at low values ($N_{trig} \leq 4$) where more events are recorded in the experiment than in the simulation. Noise in the trigger counters and a not correct treatment of δ-electrons are the explanation for this difference.
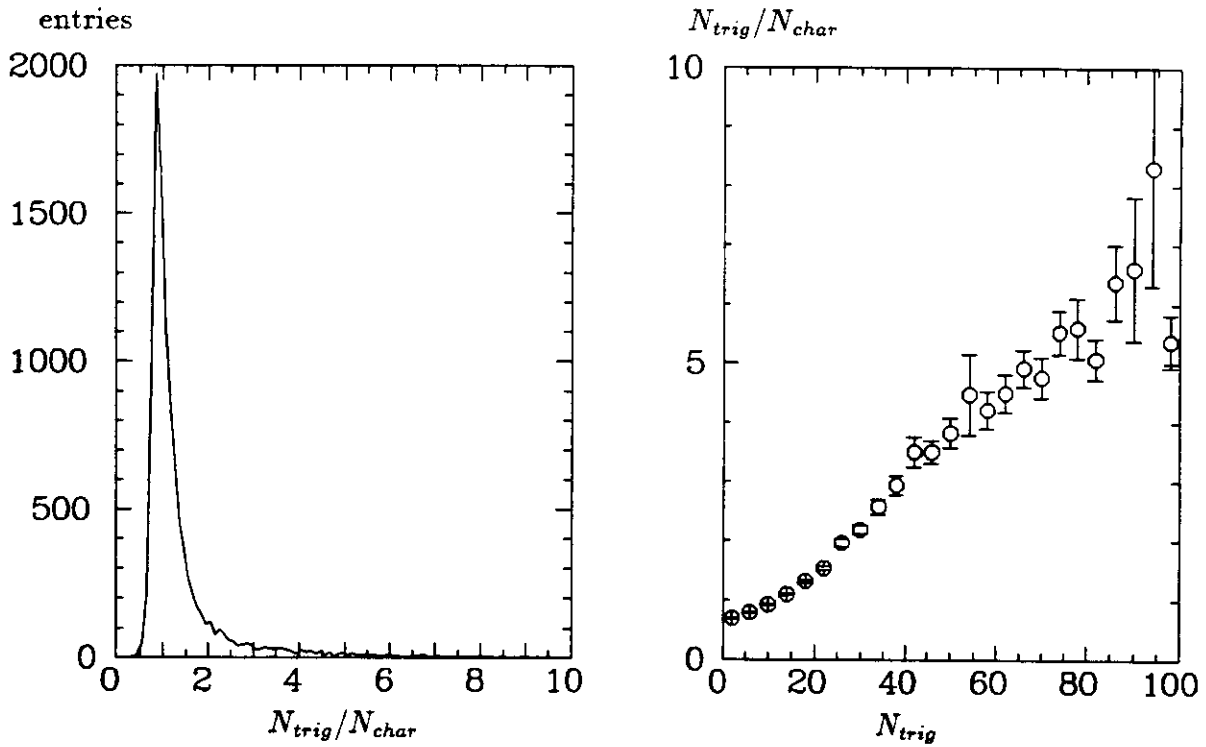
Figure 4.3: Ratio of trigger counter signal N_{trig} and charged tracks N_{char} for 50 GeV jets.
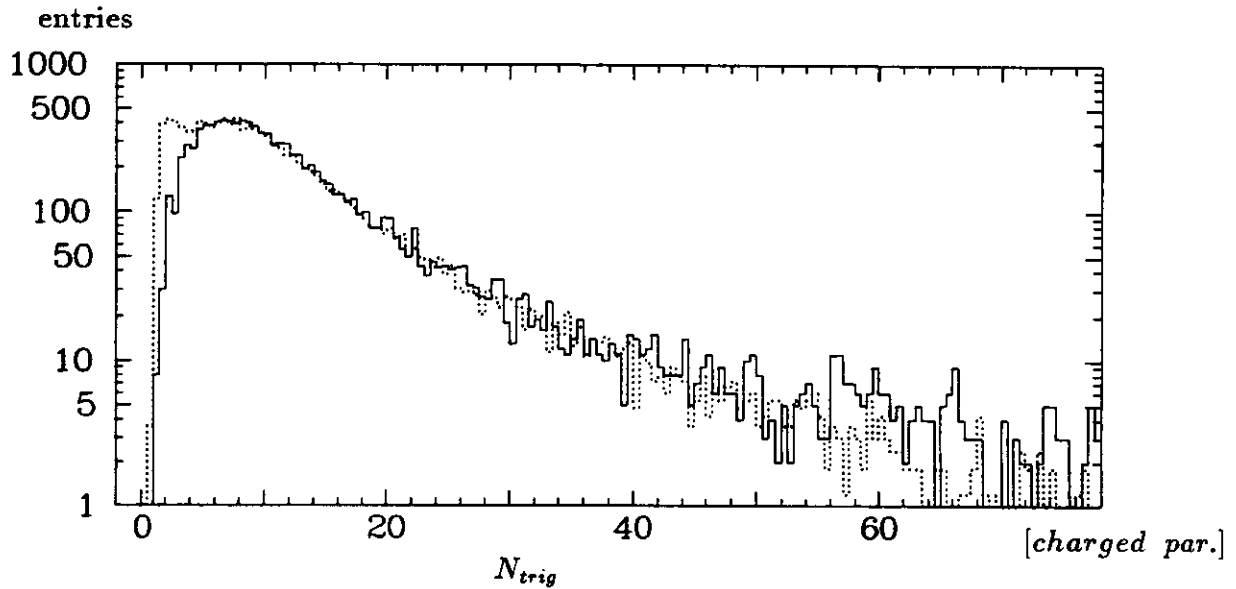

Figure 4.4: Charged multiplicity N_{trig} for 50 GeV jets. Monte Carlo data (solid), experimental data (dotted).

4.3.2 Lateral Energy Flow

The incident points of the jet particles are spread over the calorimeter front face. The mean energy fraction f_{sq} that enters the calorimeter front face within a certain region is given by

$$f_{sq} = \frac{\sum_l E_{kin}}{\sum_{all} E_{kin}}$$

where $\sum_{all} E_{kin}$ is the kinetic energy sum of all jet particles and $\sum_l E_{kin}$ is the sum of all particles for which the position at the calorimeter face is located within a square. The square is centered on the beam and the edge length is $2 \cdot l$, thus a calorimeter tower corresponds to $l = 10$ cm. In fig.4.5 the energy fraction f_{sq} versus l is shown. For 50 GeV jets about 90 % of the energy enters the central calorimeter tower, for 100 GeV jets this number increases to 94 %.
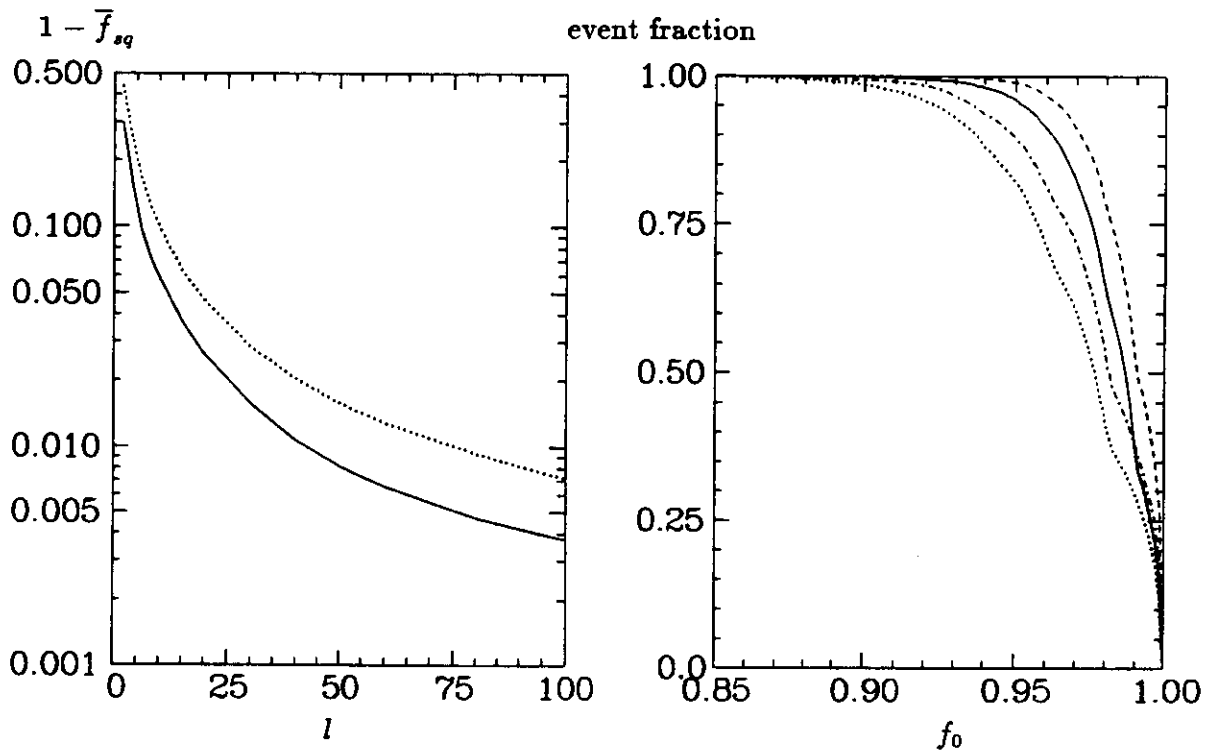
Figure 4.5: Left: Energy fraction f_{sq} which is carried by particles with an incident postion within a square of half edge length l. For 100 GeV (solid) and 50 GeV (dotted) jets. Right: The fraction of events where the energy flow of the jet particles at the calorimeter face of the 4 × 4 tower matrix is larger than f_0. The solid (dotted) and dashed (dashed-dotted) lines are the results without and with a selection on the veto counters. The jet energy is 100 GeV (50 GeV).

The 4 × 4 calorimeter tower matrix, corresponding to the dimensions of the prototype calorimeter, has a finite lateral dimension. Therefore part of the jet particles are not detected and their energy is lost. The fraction of events for which the energy flow fraction through the calorimeter face (4 × 4 matrix) is larger than f_0 is shown in fig.4.5. $f_0 = 99\%$ is fulfilled by 30 - 40 % of the events. If the events are preselected by the vetocounter (see Section 4.4) this fraction increases.

4.3.3   Energy Spectrum

The energy fraction $f(E_{kin}) \cdot \Delta E_{kin}$ carried by jet particles with an kinetic energy between E_{kin} and $E_{kin} + \Delta E_{kin}$ is:

$$f(E_{kin})\Delta E_{kin} = \frac{E_{kin}}{\sum_{jet} E_{kin}} \frac{dN}{dE_{kin}} \Delta E_{kin}$$

where dN/dE_{kin} is the event number density, and $\sum_{jet} E_{kin}$ is kinetic energy sum of all jet particles. The integrated spectrum F i.e. the energy fraction that is carried by jet particles with an energy less than E_{kin} is:

$$F(E_{kin}) = \int_{E=0}^{E_{kin}} f(E)dE.$$

In fig.4.6 the energy spectrum f and the integrated spectrum F averaged over all events are shown.
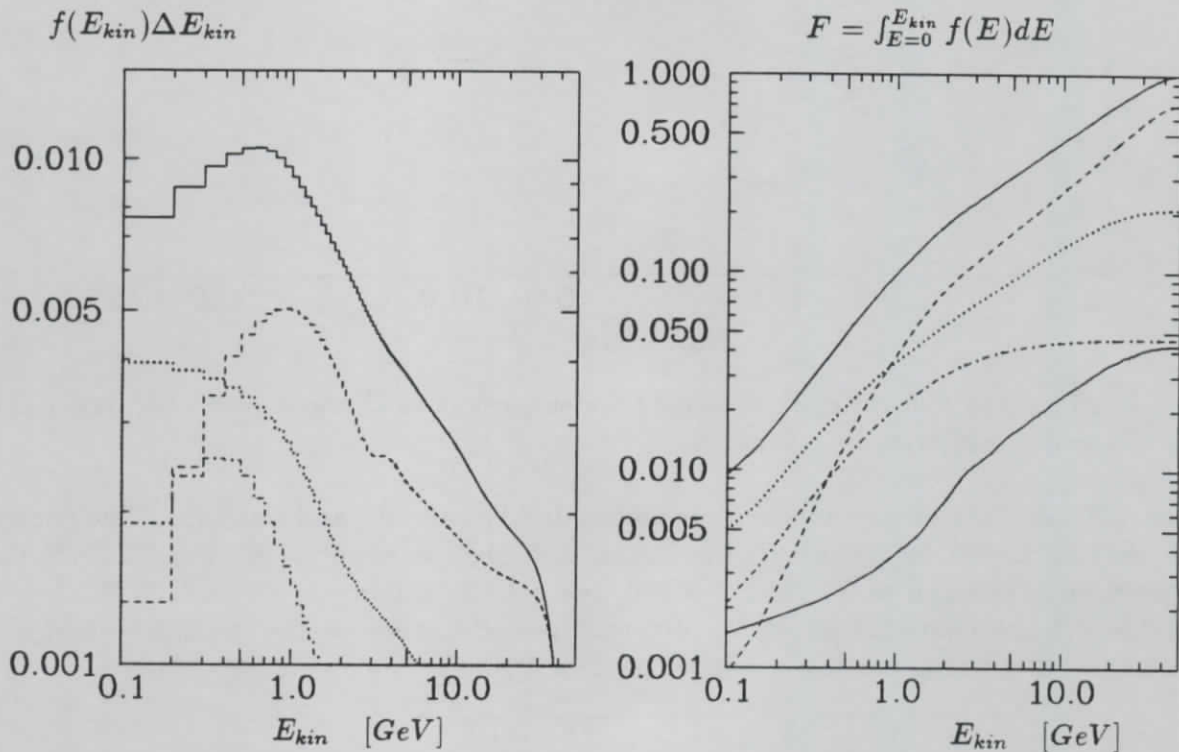
Figure 4.6: Energy fraction $f \cdot \Delta E_{kin}$ and integrated spectrum F for 50 GeV jets. It is shown for different particle types: all jet particles (solid), charged pions (dashed), photons (dotted), nucleons (dash-dotted) and the remaining particles (solid). The energy interval ΔE_{kin} is 100 MeV.

The distributions for beam energies larger than 50 GeV are similar to those shown if the energy axis is scaled by the beam energy. The main difference is that the total energy fraction carried by protons and neutrons is decreasing with increasing energy. Going from 50 GeV to 100 GeV the total energy fraction decreases from 4.6 % to 3.6 %. The decrease of the nucleon energy fraction is compensated by an increase in the energy fraction of photons.

About 70 % of the overall kinetic energy is carried by particles with $E_{kin} > 5$ GeV. This energy region is dominated by charged pions (≈ 77 %) and photons (≈ 17%).

Almost 18 % of the energy is carried by charged pions and protons with $E_{kin} < 5$ GeV. For these hadron energies the e/h-ratio is less than 1. In fig.4.7 the measured e/h-ratio is shown for protons and charged pions. As e/h < 1 the calorimeter signal for hadrons is increased compared to electrons with the same energy.
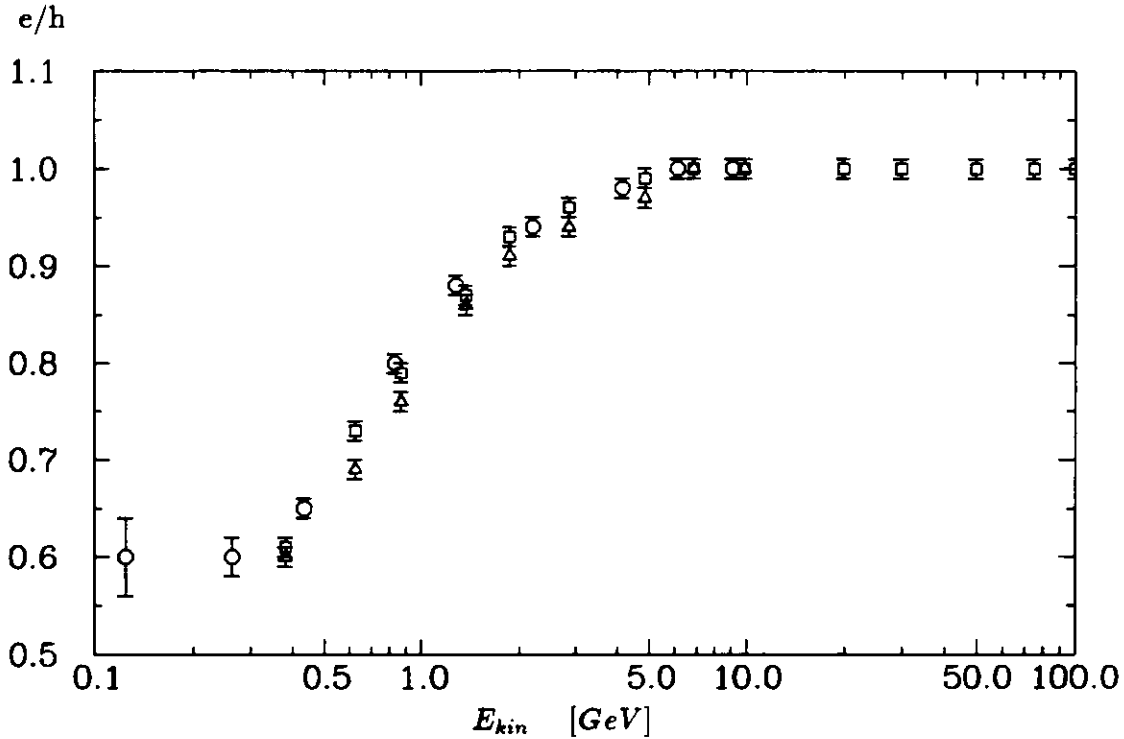
Figure 4.7: Measured e/h ratio for protons (circles), negative charged pions (squares) and positive charged pions (triangle). From [3].

Below 900 MeV the energy spectrum is dominated by photons and nucleons. The energy fraction that is carried by particles with $E_{kin} < 100$ MeV is about 1 %. For 10 MeV the energy fraction is as small as 0.1 %. For a 100 GeV jet this fraction is about 0.05 %.

In table 4.2 the contribution of the different particle types to the total jet energy is summarized. The leading particle is the jet particle with the highest energy. It is a π^- and

| particle | $E\,[GeV]$ | | |
type	$E_{beam}=$ 50GeV	= 75GeV	= 100GeV
γ	9.7 (10.2)	15.3 (15.8)	20.9 (21.8)
$e^{\pm}$	0.6 (2.4)	0.8 (3.6)	1.0 (4.7)
$\pi^{\pm}$	33.5 (11.5)	50.6 (17.4)	68.3 (23.9)
n	1.2(1.6)	1.6 (2.4)	1.9 (3.2)
p	1.0 (1.6)	1.2 (2.0)	1.4 (2.8)
rest	1.7 (4.8)	2.6 (7.0)	3.6 (9.5)
leading part.	22.2 (8.9)	33.6 (13.6)	46.6 (18.6)

Table 4.2: Mean contribution $\bar{E}$ (in GeV) off the different particle types. The values in the brackets are the r.m.s.

its direction is close to the beam direction. On the average about 45 % of the total jet energy

is carried by the leading particle. About 67 - 78 % of the total energy is carried by charged pions. The contribution of photons and electrons is 21 - 22 %.

As mentioned before neutrinos and also muons are produced and no energy or only a small fraction of the energy is deposited in the calorimeter. The energy carried by these particles relative to the beam momentum is 0.14 % - 0.08 % and therefore can be neglected.

4.3.4 Jet Energy and Energy Resolution

There are different possibilities to define the overall energy of a jet. The distributions for the sums of the kinetic energies and the total energies of all jet particles is shown in fig.4.8.
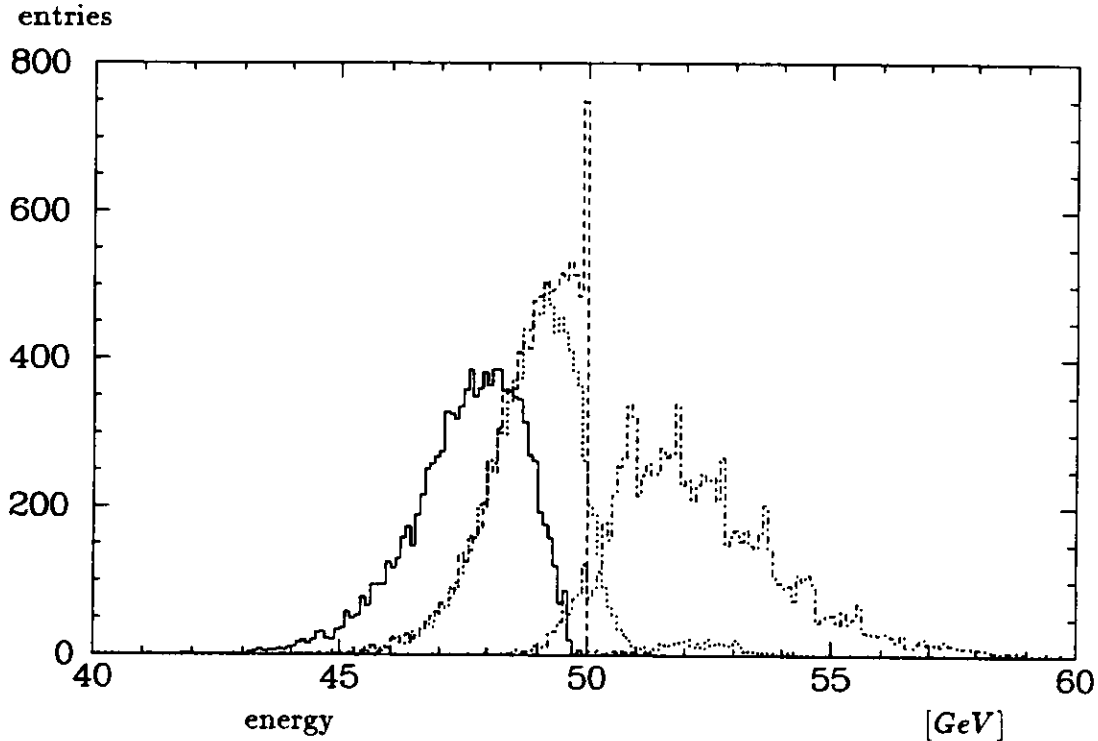
Figure 4.8: Energy distribution for different energy sums. For 50 GeV Monte Carlo interactions. Kinetic energy (solid), total energy (dashed dotted), reduced energy E_{red} (dashed) and expected energy E_{eoh} (dotted).

In addition the energy sums E_{red} and E_{eoh} are introduced. The reduced energy E_{red} is:

$$E_{red} = \sum E_{tot} + \sum_{p,n,\alpha} E_{kin}$$

The sum $\sum E_{tot}$ is the sum of the total energy of all particles excluding nucleons and heavier nuclear fragments. For these particles the kinetic energy is summed ($\sum_{p,n,\alpha} E_{kin}$). Nucleons and nuclear fragments are released from a nucleus by an interaction and no energy of the primary pion is transfered to the production of their rest masses.

E_{eoh} is the expected calorimeter response. It has been calculated by summing over the expected calorimeter response which was calculated under the following assumptions: For photons, electrons, positrons and also neutrons the calorimeter response is proportional to the kinetic energy of a particle. A muon traversing the calorimeter deposits on the average

4 GeV. The response for hadrons is proportional to the kinetic energy divided by the e/h ratio which is less than one for kinetic energies less than 5 GeV. A parameterisation of the experimental determined e/h-ratio $\gamma_{eh} = \gamma_{eh}(E_{kin})$ was used.

$$E_{eoh} = \sum_{e^{\pm},\gamma,n} E_{kin} + \sum_{hadrons} E_{kin}/\gamma_{eh} + 4\text{GeV} \cdot \text{N}_{muon}$$

In table 4.3 the mean and standard deviation for the different energy sums are shown.

energy	$\overline{E}_{tot}$	$\overline{E}_{kin}$	$\overline{E}_{red}$	$\overline{E}_{eoh}$	$\overline{P}$
50	52.35 (1.81)	47.56 (1.15)	48.85 (0.89)	49.00 (1.13)	50.56 (0.92)
75	77.61 (1.97)	72.11 (1.33)	73.69 (1.02)	73.76 (1.34)	75.60 (1.00)
100	102.50 (1.92)	97.13 (1.32)	98.69 (1.01)	98.67 (1.26)	100.61 (1.00)

Table 4.3: Mean energies for jets. E_{tot} is the energy summed over all jet particles. E_{kin} is the sum over the kinetic energies, E_{red} is the energy of the primary particle that is transfered to the energy of the jet particles and E_{eoh} is the expected calorimeter signal (see also in the text). P is the sum over the absolut momenta of the jet particles. In brackets the r.m.s. are shown. Only tracks with $\theta < \pi/2$ were considered.

The energy loss in the target and in the counters of the interaction trigger is the difference of the kinetic energy of the initial pion E_π and the energy E_{red} of the outgoing particles. For 50 GeV jets the energy loss is 1.01 GeV and for 100 GeV jets 1.17 GeV.

About 1.3 GeV for 50 GeV and 1.6 GeV for 100 GeV interactions is spent in the production of charged pion masses and masses of heavier hadrons (except nucleons). This energy loss is partly compensated by the non-linear response of low energy hadrons (e/h<1). The difference between $\overline{E}_{eoh} - \overline{E}_{kin}$ is the signal increase due to this effect which is about 1.5 GeV.

The mean signal loss of jets relative to the beam particles is 2 (4.9) % at 50 GeV , 1.7 (3.9) % at 75 GeV and 1.3 (2.9) % at 100 GeV . The signal loss was calculated by the difference between the jet energy E_{eoh} (E_{kin}) and the energy of the beam particle.

Energy resolution   The energy resolution for jets is determined by:

- the fluctuations of the incoming jet energy

- the mean response of different particle types in a jet (e, hadrons, n..)

- the inherent calorimeter resolution for the individual jet particles

The calorimeter signal fluctuation σ for the measurement of N jet events is given by:

$$\sigma^2 = \frac{1}{N}\sum_{i=1}^{N}(E_i - \overline{E})^2 + \frac{1}{N}\sum_{i=1}^{N}\sigma_i^2 \qquad (4.1)$$

E_i is the mean calorimeter signal for event i and $\overline{E}$ is the calorimeter signal averaged over all jet events i:

$$\overline{E} = \frac{1}{N}\sum_{i=1}^{N}E_i.$$

σ_i is the r.m.s. of the calorimeter signal for the jet event i if this event has been measured many times.

The first sum in eq. 4.1 describes the calorimeter fluctuations due to the fluctuations of the incoming jet energy but also the fluctuations due to the mean response of different particle types in a jet. This means that the mean calorimeter signal can be different for jets with the same energy because the calorimeter response depends on the type and energy of a particle. In particular the change of the e/h-ratio for low energy hadrons is important.

The second sum in eq. 4.1 describes the inherent calorimeter fluctuations. The signal fluctuation σ_i for a jet event is given by the signal fluctuations of the individual jet particles.

$$\sigma_i^2 = \sum_{i=1}^{l} \sigma_k^2 \tag{4.2}$$

where σ_k is the fluctuation for a single particle. The sum runs over all particles l that belong to a jet. The fluctuation σ_k for a single particle was calculated by two methods. The first method uses the following values.

$$\sigma_k = 0.18\sqrt{E_{kin}} \quad \text{for} \quad \gamma, e^{\pm}$$

$$\sigma_k = 0.35\sqrt{E_{kin}} \quad \text{for hadrons}$$

For the ZEUS calorimeter it has been shown [10] that the energy resolution for hadrons with $E_{kin} < 5\text{GeV}$ improves. This improvement has been taken into consideration by the second method. The fluctuation for an electromagnetic interacting particles was calculated as in method 1. In table 4.4 the results for the different resolutions are summarized. For the determination of the sum $\sum_{i=1}^{N}(E_i - \overline{E})^2$ the calculated E_{eoh} value of a jet event was used. Cuts on the veto scintillation and lead glass counters as well on the trigger counters were applied (see next section).

	50 GeV	75 GeV	100 GeV
$(\frac{\sigma_{eve}}{E}\sqrt{E})_1$	31.55	31.61	31.7
$(\frac{\sigma_{eve}}{E}\sqrt{E})_2$	30.46	30.79	31.09
$\frac{\sigma_{tar}}{E}\sqrt{E}$	11.72	10.14	8.87
$(\frac{\sigma}{E}\sqrt{E})_1$	33.65	33.2	32.9
$(\frac{\sigma}{E}\sqrt{E})_2$	32.63	32.4	32.34

Table 4.4: Estimated energy resolution for jets. For index 2 (1) the improved energy resolution for low energy hadrons is (is not) taken into account. σ_{eve} are the fluctuations due to the inherent calorimeter resolution and σ_{tar} are the fluctuations due the mean response of different particle types in a jet and fluctuations in the incoming jet energy. σ is the quadratic sum of σ_{eve} and σ_{tar}.

The fluctuations due to the incoming jet energy σ_{tar} are much smaller than the fluctuations due to the inherent calorimeter resolution. The inherent calorimeter resolution $(\sigma_{eve}/E)_1$ is about 13 % smaller than the calorimeter resolution for single pions ($0.35/\sqrt{E}$). This is due to the photon and electron contribution to the jet energy, and the better energy resolution for these particles. Also the calculated total resolution $\sigma/E \approx 0.33\sqrt{E}$ is smaller for jets than for pions. This shows that the energy fluctuations in Be interactions are smaller than for interactions in Uranium. The improvement of the energy resolution due to the low energy hadrons is small, < 3 %.

The mean hadronic energy fraction f_{had} of a jet is about 77 %. The energy resolution which is expected is calculated by eq. 4.3 and is in a good agreement with the energy resolution $(\sigma_{eve}/E)\sqrt{E}$ of 31.5 - 31.7 % from table 4.4.

$$\frac{\sigma}{E}\sqrt{E} = \sqrt{0.35^2 f_{had} + 0.18^2(1 - f_{had})} \approx 31.9\% \qquad (4.3)$$

4.4 Calorimeter Energy

In this section the calculation of the energy measurement for jets and pions are discussed and compared with the experimental measurements.

4.4.1 Energy Losses

Before the energy measurement for jets and pions are compared the energy, which misses the 4 × 4 tower matrix of the calorimeter is calculated and compared to the measured energy loss.

Vetocounters The mean calorimeter signal $\overline{E}_{cal}$ increases when the vetocounter cuts N_s^c and N_l^c decrease. The selection criteria for the veto scintillation counter is $N_s < N_s^c$ and respectively $N_l < N_l^c$ for the lead glass counters. The calculated difference of the mean calorimeter signal between a strong selection ($N_s^c = .5, N_l^c = .5$) and no selection is 1.6 % for 100 GeV jets and 2.1 % for 50 GeV jets. This is larger than the measured increase of 1.0 % for 100 GeV jets and 1.4 % for 50 GeV jets. This indicates that the angular spread of the jet particles is wider in the simulation than in the experiment.

For the Monte Carlo simulation the values for N_s^c and N_l^c were determined so that the mean calorimeter signal without cuts is 0.5 % less than the mean signal with the cuts N_s^c and N_l^c. The cuts are:

$$N_s^c = 4 \qquad N_l^c = 1.5$$

The difference of 0.5 % was chosen because this is the measured difference described in section 3.3.1.

Lateral energy deposition The lateral energy deposition in the calorimeter is wider in the simulation than in the experiment. In table 4.5 the energy fractions recorded in the four calorimeter modules are shown.

energy		f_{mod1}	f_{mod2}	f_{mod3}	f_{mod4}
50	MC	1.19 (0.53)	9.95 (6.00)	79.03 (87.2)	9.52 (6.02)
50	EX	1.33 (1.06)	8.83 (6.56)	81.93 (86.5)	7.91(5.88)
100	MC	0.96 (0.49)	7.81 (5.45)	82.95 (88.3)	7.93 (5.52)
100	EX	0.90 (0.91)	6.60 (5.46)	85.9 (88.2)	6.6 (5.48)

Table 4.5: Energy fraction (%) in the four calorimeter modules for the simulation (MC) and experimental data (EX). The values for jets and pions (in parenthesis) are given. The relative statistical error is less than 2 % excluding f_{mod1} with a relative error of about 6 %.

In the simulation there is less energy in module 3, where most of the energy is deposited. The energy fraction in the outer modules is smaller in the simulation than in the experiment.

The calculated energy recorded outside the calorimeter (4 × 4 matrix) is $f_{out} \approx 3.1$ % for 100 GeV jets and $f_{out} \approx 4.2$ % for 50 GeV jets. This energy loss is correlated with the energy fraction f_1 deposited in calorimeter module 1 and f_u deposited in the four tower 4 of the four modules.

$$\frac{f_{out}}{f_1 + f_u} \approx 1.49$$

The energy loss determined by $f_1 + f_u$ is underestimated by approximately 50 %. However this result yields only a rough estimation for the experiment because of the different lateral energy distribution profile of the simulation and experiment.

4.4.2 Calorimeter Response for Single Particles

The energy response for the individual jet particles was simulated for the tracks of the 50 GeV jets. In total 80.000 tracks were simulated corresponding to 1820 jet events.

For almost 50 % of the simulated particles the calorimeter signal E_{cal} is zero. The kinetic energy of such a particle, most of them are photons, is typically less than 10 MeV. The mean energy fraction that these particles contribute to the total kinetic energy of a jet event is less than 0.5 % and they are not taken into consideration for the following analyses.

In fig.4.9 the difference ΔE of the signal recorded in the calorimeter and the kinetic energy of the corresponding particle is shown. The difference was normalized by the standard deviation σ which was calculated by $\sigma = a \cdot \sqrt{E_{kin}}$ where a=0.18 for electromagnetic interacting particles and a=0.35 for all other particles.

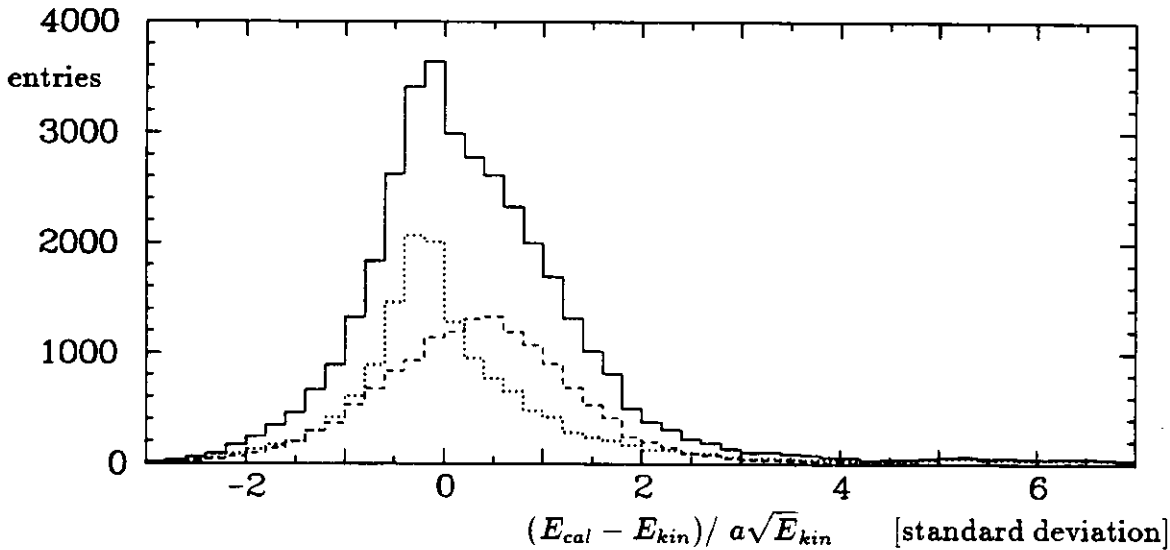$$\Delta E = \frac{E_{cal} - E_{kin}}{a\sqrt{E_{kin}}}$$

Figure 4.9: Difference between the calorimeter signal and the kinetic energy of the incoming particle. The difference was normalized by the expected standard deviation (a=0.18 for $\gamma, e^{\pm}$, a=0.35 for all other particles). It is shown for all particles (solid), photons (dotted) and charged pions (dashed).

The distribution of ΔE is not symmetric around zero. This is because the calorimeter response is nonlinear in particular for low energy particles and therefore $E_{cal} - E_{kin}$ is not zero on the average.

The calorimeter response for photons, charged pions, protons and neutrons versus their kinetic energy is shown in fig.4.10. The relative difference $\Delta E/E$ is:

$$\frac{\Delta E}{E} = \frac{E_{cal}}{E_{kin}} - 1$$

where E_{cal} is the calorimeter signal and E_{kin} the kinetic energy of a particle. The response for photons is linear for energies > 200 MeV. For photon energies less than 100 MeV the calorimeter response is 4 times larger than the kinetic energy of the photon. This peculiar behavior may be related to the fact that the calorimeter starts with a aluminum-scintillator layer and not with a uranium-scintillator layer.
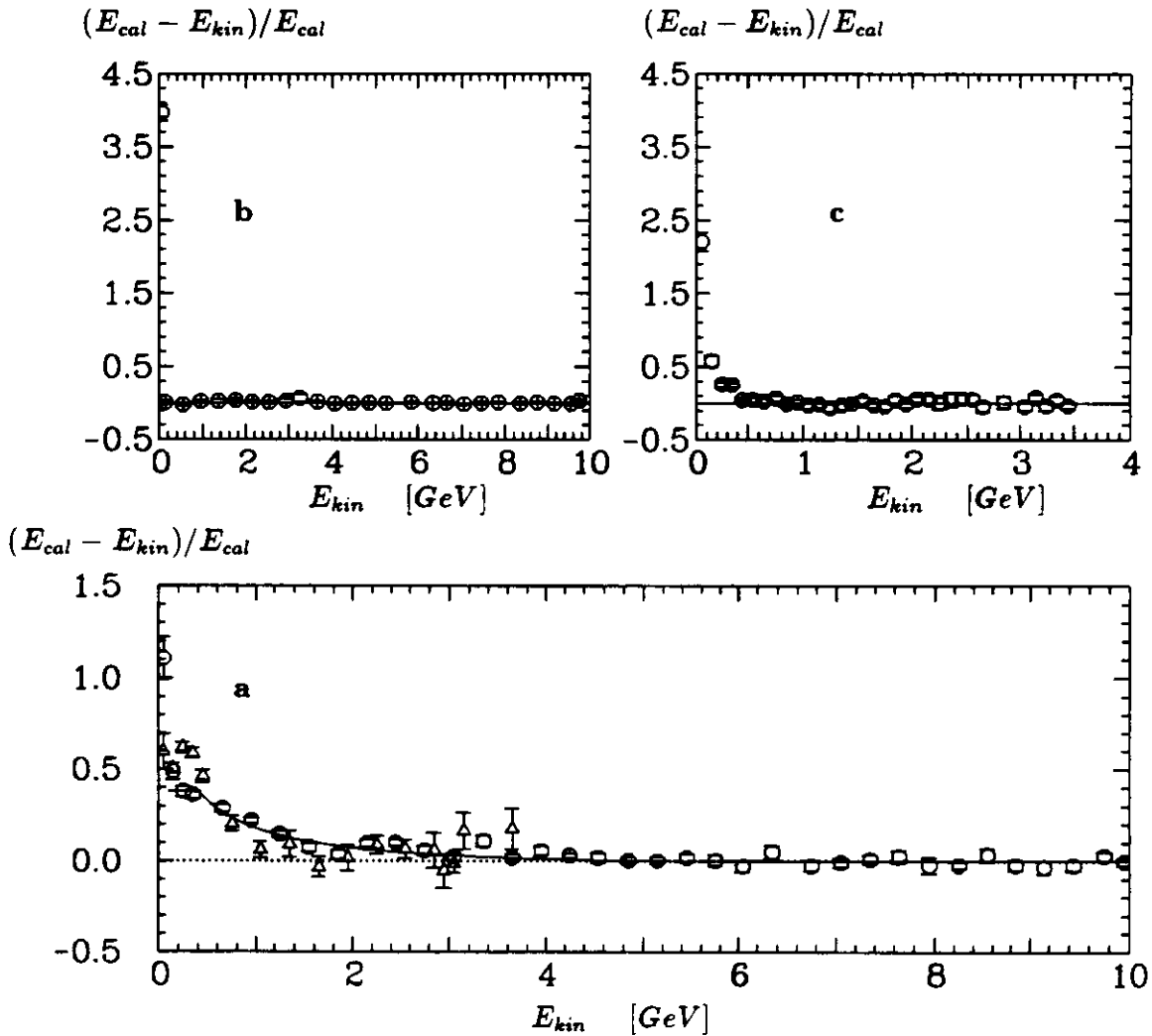

Figure 4.10: Calculation of the ratio of the signal measured by the calorimeter and the kinetic energy of the corresponding particle. This ratio is shown versus the kinetic energy of a particle. It is shown for photons (b), and neutrons (c). In (a) it is shown for pions (circles) and protons (triangles). The solid line in (a) shows the expected curve due to the e/h-ratio.

For charged pions with $E_{kin} > 7$ GeV the calorimeter signal is systematically lower than the kinetic energy of the incident particle, on the average - 1.3 %. If the mean calorimeter

signal was determined by fitting a gaussian instead of calculating the mean the nonlinearity decreases (-0.3 %) because the mean value is less sensitive to tails in the signal distribution. The increase of the curve for pion energies below 5 GeV corresponds to the decrease of the e/h-ratio of the calorimeter. The curve for protons is similar to those for pions. Nevertheless below 200 MeV the proton response is constant whereas the pion curve is still increasing. It is not clear if this difference is real because it can not be compared to measured results. The e/h-ratio for pions was measured for kinetic energies > 380 MeV. The e/h-ratio for protons were measured for $E_{kin} > 124$ MeV and is in good agreement with the calculated curve shown in fig.4.10.

4.4.3   Calorimeter Response for Jets

In this section the calorimeter response for jets is discussed and compared to the response for charged pions. The results obtained from the Monte Carlo simulation are compared with those obtained from the experiment. The jet events were selected by cuts on the signal of the vetocounters and the charged multiplicity in the trigger counters. The cuts for the simulations were the same as used in the experiment.

The calculated mean calorimeter signal for jets relative to that of pions has been determined by two different methods. The first method uses the mean energy deposited in the 4 × 4 towers. The second method calculates the mean energy from the whole calorimeter. In fig.4.11 the relative energy difference

$$\frac{\Delta E}{E} = \frac{E_{jet} - E_{pion}}{E_{pion}}$$

is shown. The experimental results are also shown for comparison. If the calorimeter energy
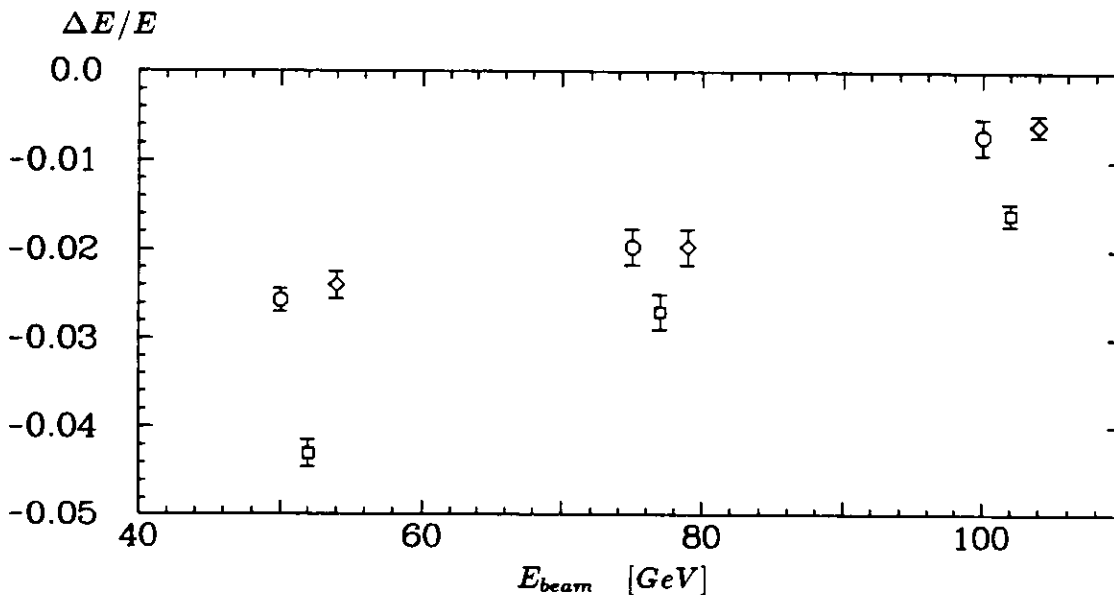

Figure 4.11: Relative energy difference $\Delta E/E$. The circles are the experimental data. For the Monte Carlo simulation the results are shown for the 4 × 4 tower matrix (squares) and for the whole calorimeter (diamonds).

was calculated by the 4 × 4 tower matrix the energy loss for jets is 1 - 2.5 % larger than the

experimental result. For 50 GeV the difference is larger than for the higher energies. This is explained by the energy leakage out of the calorimeter which is larger at low energies. If the energy loss $\Delta E/E$ is calculated from the whole calorimeter the simulation and experimental results agree quite well. In addition a difference may also occur due to a not correct simulation of the pion-target interaction. However it is not known how big these effects are.

In fig.4.12 the relative resolution

$$R = \frac{(\sigma_E/E)_{jet}}{(\sigma_E/E)_{pion}}$$

is shown. The results from the simulation indicates a slightly better energy resolution for jets and the improvement is independent of the energy. The slight improvement of the measured resolution with increasing energy is not reproduced by the simulation.
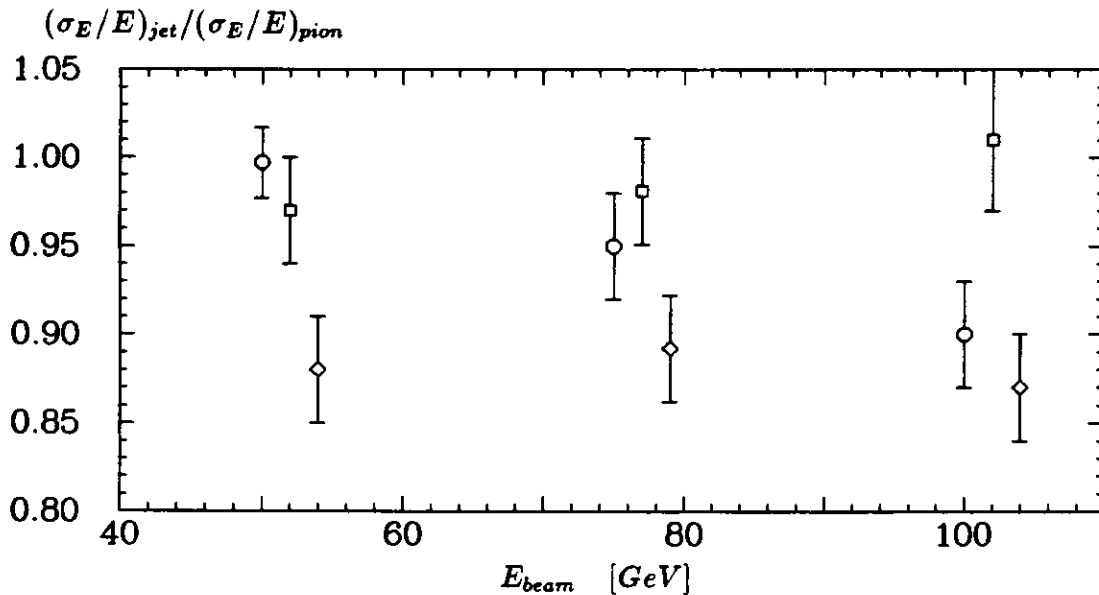

Figure 4.12: Relative energy resolution R. The circles are the experimental data. For the Monte Carlo simulation the results are shown for the 4×4 tower matrix (squares) and for the whole calorimeter (diamonds).

4.5 Influence of Passive Material

The influence of passive material was investigated by aluminum plates of 4 and 10 cm thickness placed in front of the calorimeter. The events were selected as described before. In fig.4.13 the relative signal difference due to the aluminum absorber is shown. For the Monte Carlo simulation the signal difference was calculated by the 4×4 tower matrix and the whole calorimeter respectively. Both methods yield almost the same result.

The energy difference from the Monte Carlo simulation is systematically 0.5 - 1 % less than the one obtained from the experiment.

The change of the energy resolution due to the aluminum absorber is shown in fig.4.14. The agreement between experiment and Monte Carlo calculation is satisfactory for the data with 4 cm thick aluminum plates but there are differences for the 10 cm 50 GeV data points.
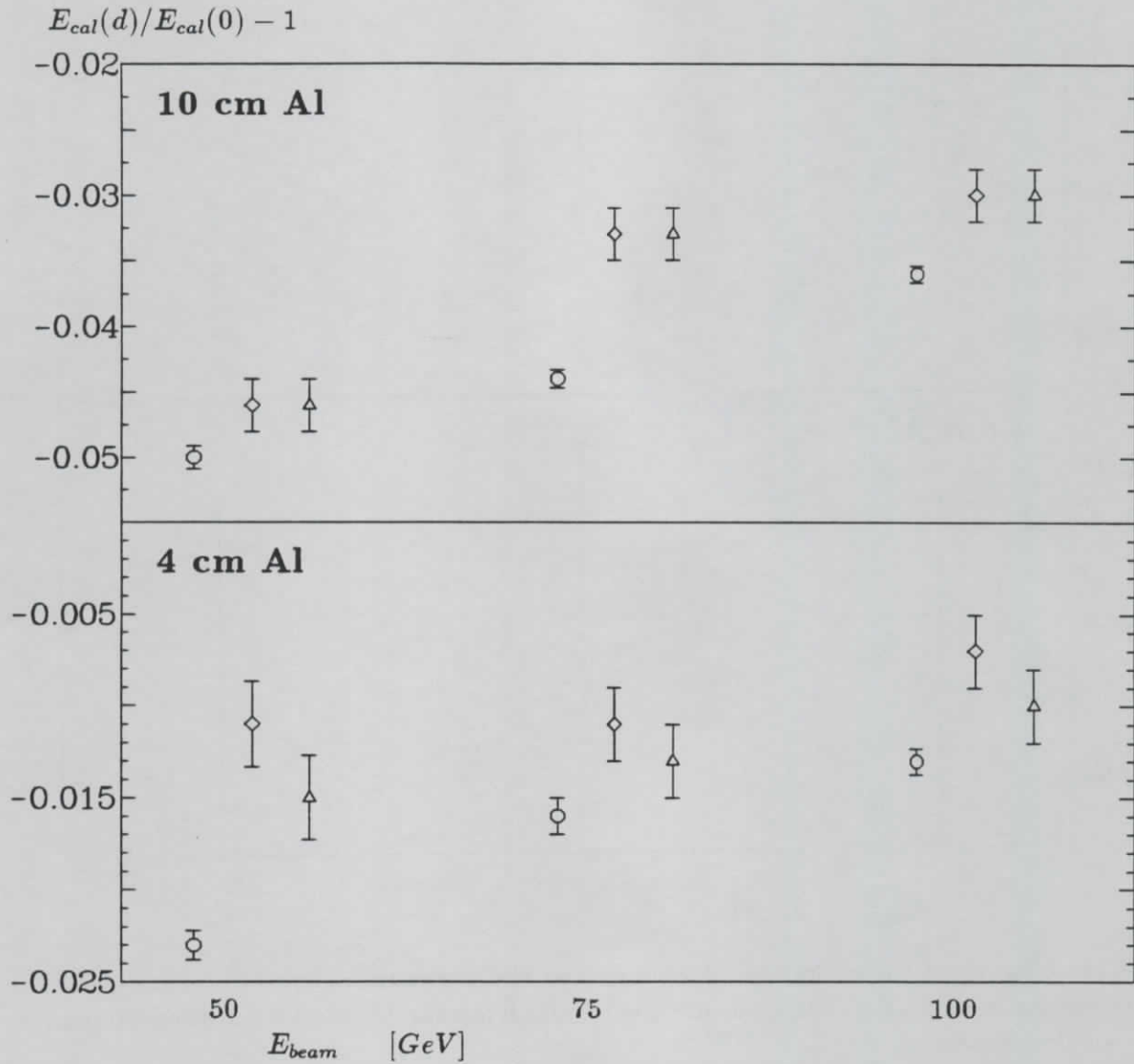
Figure 4.13: Relative energy difference for jets with an aluminum absorber in front of the calorimeter. The circles are the experimental results, the diamonds (triangles) are the results from the Monte Carlo simulation using the 4 × 4 (whole) calorimeter.

In particular the calculated resolution for the 50 GeV and 75 GeV data points are too large compared to the measured data. However within 2σ the results agree. The large error of the Monte Carlo simulation is due to the small number of events.

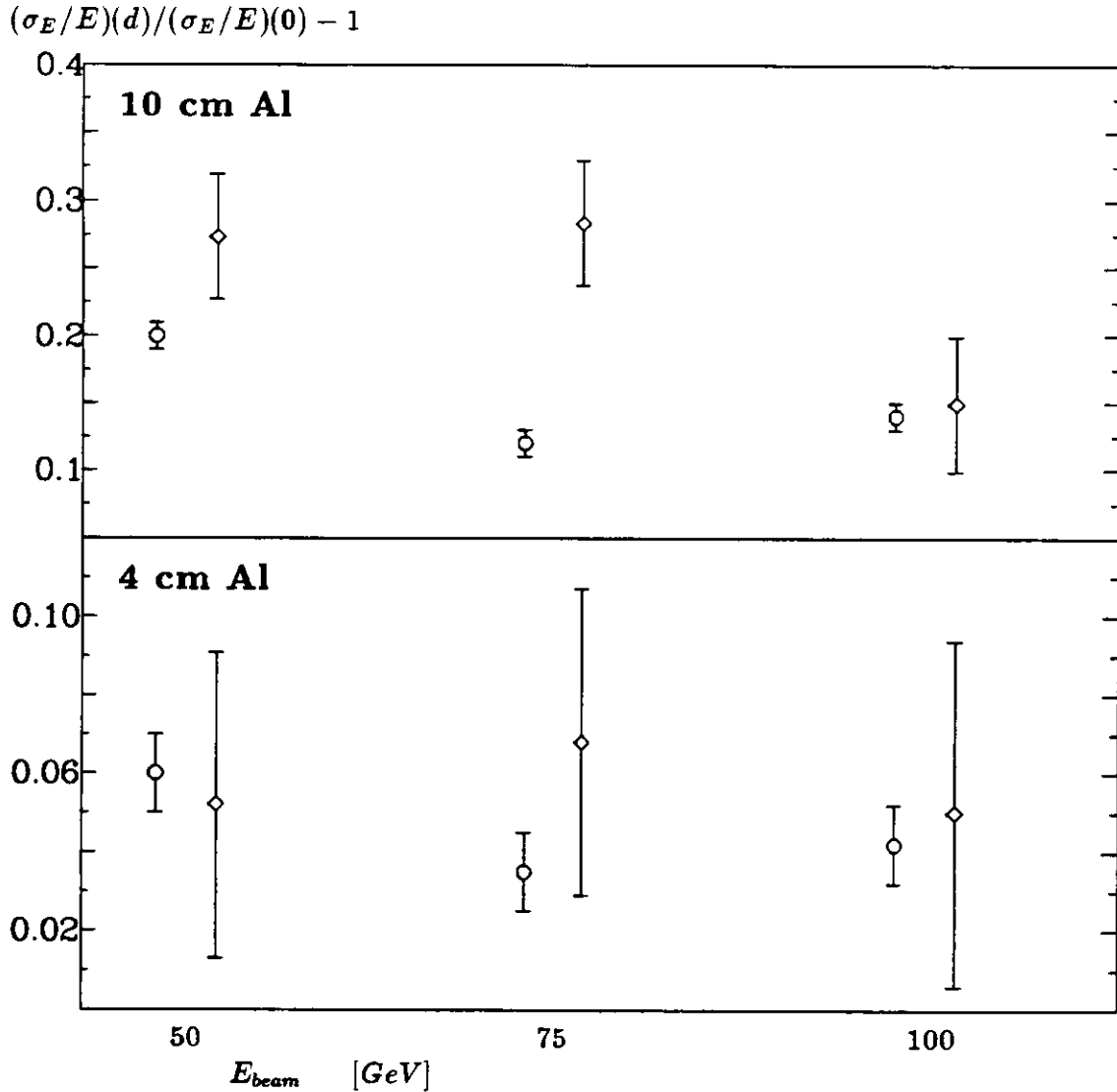$$(\sigma_E/E)(d)/(\sigma_E/E)(0) - 1$$

Figure 4.14: Change of the energy resolution due to the aluminum absorber. The circles are the experimental results, the diamonds are the results from the Monte Carlo simulation using the 4 × 4 calorimeter.

4.5.1 Energy Loss Corrections

In fig.4.15 the energy difference ΔE versus the charged multiplicity in front of the aluminum absorber N_{trig} and behind the absorber N_{pres} obtained by the experiment and by the simulation are compared. The energy difference ΔE is calculated by:

$$\Delta E = E_{cal}(d) - \overline{E}_{cal}(0)$$

where $E_{cal}(d)$ is the calorimeter energy for a jet event with an aluminum absorber of thickness d in front of the calorimeter and $\overline{E}_{cal}(0)$ is the mean energy without an absorber. The results

are shown for 50 GeV jets and 10 cm aluminum absorber in front of the calorimeter. The shapes of the curves obtained from the simulation are in good agreement with those from the experiment. However the signal loss is somewhat less for the simulated data than for the experiment. As already shown in the last section the mean signal difference between the calorimeter energy with and without an absorber is 0.5 - 1 % smaller in the Monte Carlo simulation. The correlation between the charged multiplicity N_{trig} and the difference $\Delta N = N_{pres} - N_{trig}$ is shown in fig.4.15. The difference of both curves is less than a few percent which is a good agreement.
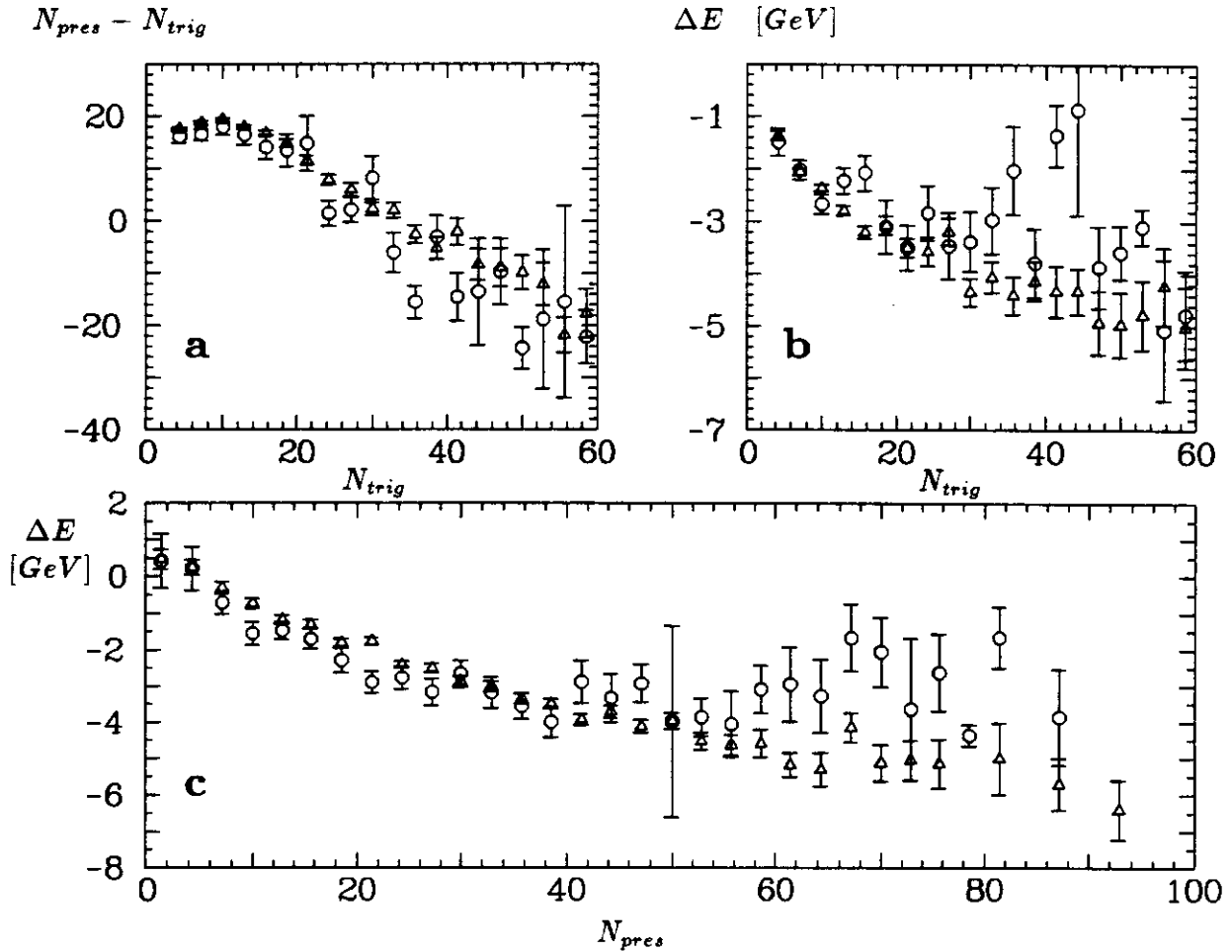

Figure 4.15: Energy loss ΔE versus N_{trig} (b) and N_{pres} (c). Fig, (a) shows the correlation $N_{pres} - N_{trig}$ versus N_{trig}. The triangles are the results from the Monte Carlo simulation and the circles are the experimental data. 10 cm aluminum.

The energy correction for the energy loss in the aluminum absorber has been done in the same way for the simulation as for the experiment. If the charged multiplicity N_{trig} and respectively N_{pres} was used the correction is:

$$E^{corr} = E_{cal} + \varepsilon N_{trig} \qquad (4.4)$$

respectively:

$$E^{corr} = E_{cal} + \vartheta N_{pres} \qquad (4.5)$$

And if both charged multiplicities were used it read:

$$E^{corr} = E_{cal} + \varrho N_{trig} + \varphi \Delta N \tag{4.6}$$

The correction parameters were determined by requiring that the mean energy after the correction is equal to the mean energy for jets without aluminum plates in front of the calorimeter. For equation 4.6 as second condition it was optimum energy resolution required. In fig.4.16 the results are shown. The parameter values from the experiment are shown for comparison. The parameter values obtained from the Monte Carlo simulation are smaller than
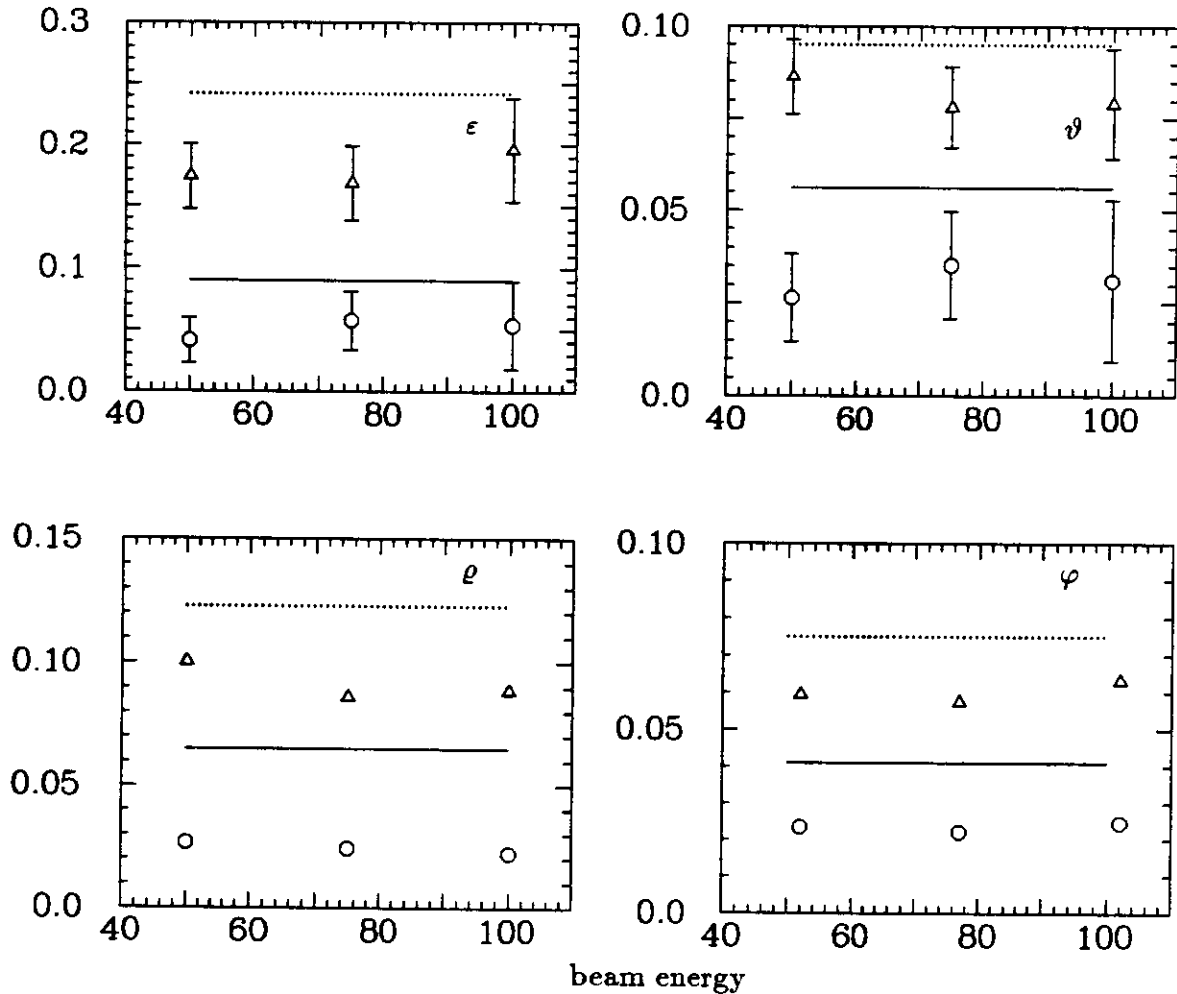

Figure 4.16: Energy correction parameter versus the beam energy. Circles (triangles) are the results for 4 (10) cm aluminum in front of the calorimeter. The lines are the experimental correction parameters for 4 cm (solid) and 10 cm (dashed) aluminum absorber.

those obtained from the experiment. This is because the energy loss due to the aluminum absorber is smaller in the simulation and therefore the correction parameter are also smaller. The largest differences are observed for 4 cm aluminum plates, the simulated results are smaller by a factor of 2. The relative error of a correction parameter is

$$\frac{\Delta \varepsilon}{\varepsilon} = \frac{\Delta \overline{E}_{cal}}{\overline{E}_{cal}} \frac{1}{\frac{\overline{E}_{cor}}{\overline{E}_{cal}} - 1}$$

The second factor on the right side is in the range of 20 - 100 and therefore a small relative error in the calorimeter energy will result in a larger relative error for the correction parameter. On the other hand a large relative error for the correction parameter gives only a small error for the corrected energy E_{cor}.

The correction parameter are also almost energy independent as it has been found in the experiment.

The observed energy loss, which depends on the charged multiplicity N_{trig} and N_{pres} is caused by two effects:

- energy losses in the aluminum absorber, ΔE_{Al}.

- energy losses in the target, veto and trigger counters, ΔE_{ta}.

In the Monte Carlo simulation the influence of aluminum plates of 0, 4 and 10 cm thickness was simulated for each jet event. Therefore the contribution of the two different energy losses can be calculated. The energy loss ΔE_{Al} in the aluminum absorber is the difference between the calorimeter energy $E_{cal}(0)$, recorded without aluminum absorber, and the energy $E_{cal}(d)$, recorded with aluminum absorber of thickness d, for the same event.

$$\Delta E_{Al} = E_{cal}(0) - E_{cal}(d)$$

The energy loss ΔE_{ta} in the target and the counters surrounding the target ΔE_{ta} is the difference between the energy of the beam particle and the signal recorded by the calorimeter without an aluminum absorber. This energy loss is independent of the aluminum thickness.

$$\Delta E_{ta} = E_{beam} - E_{cal}(0)$$

The total energy loss ΔE of an event i.e. the difference between the calorimeter energy and the energy of the beam particle is the sum:

$$\Delta E = \Delta E_{Al} + \Delta E_{ta}.$$

In fig.4.17 the correlation between the three different energy losses and the charged multiplicity N_{trig} is shown. The important result of this figure is that the correlation i.e. the slope, between the energy loss in the target and N_{trig} is comparable with the correlation between the energy loss in the aluminum absorber and N_{trig}.

In fig.4.18 the correlation between the energy losses ΔE_{Al} and ΔE_{ta} and the charged multiplicity N_{pres} are shown. The correlation for ΔE_{ta} versus N_{pres} is much weaker than those between ΔE_{Al} and N_{pres}. By fitting a straight line the slope for the curve ΔE_{Al} is about 4 times larger than the slope for the curve ΔE_{ta}.

The aim of the energy loss correction is to correct for the energy loss in the aluminum absorber ΔE_{Al} but not to correct for the energy loss in the target ΔE_{ta}. The request that only the aluminum loss is corrected is identical with the condition:

$$\Delta E_{Al} - \epsilon N = 0$$

where ϵ is the correction parameter and N is the charged multiplicity which is used for the correction. In particular the correlation between this difference and the charged multiplicity N should be a constant line with a value of 0. In fig.4.19 this correlation is shown for the energy correction with N_{trig} and N_{pres} respectively. In this figure the energy difference was normalized by the mean calorimeter signal with no aluminum absorber.
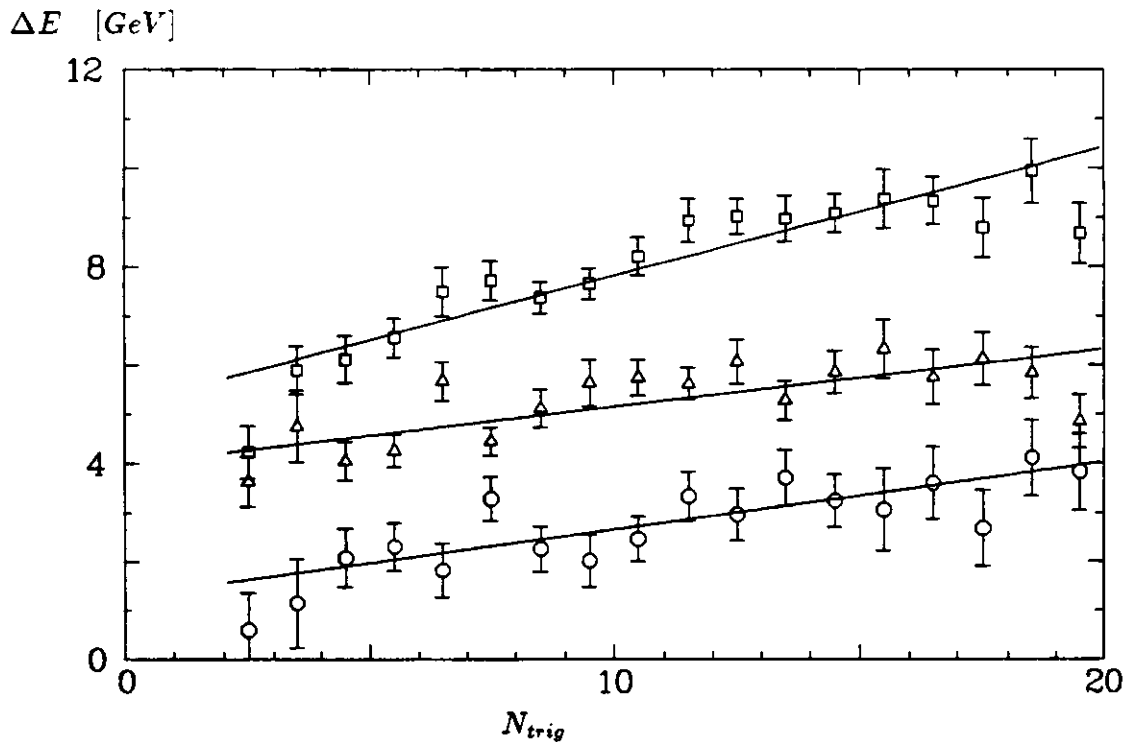
ΔE $[GeV]$

Figure 4.17: Energy loss ΔE_{Al} (circles), ΔE_{ta} (triangles) and ΔE (squares) versus the charged multiplicity N_{trig}. Monte Carlo simulation. Shown for 50 GeV jets, 10 cm aluminum absorber and 0.03 λ thick target.
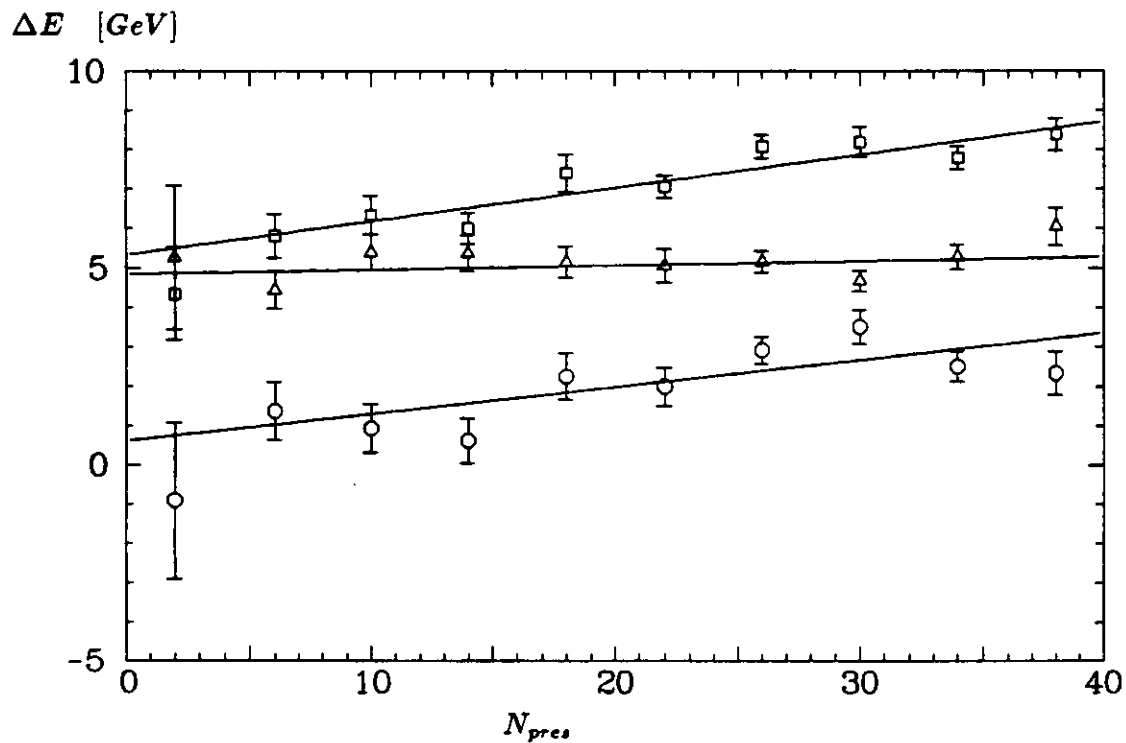
ΔE $[GeV]$

Figure 4.18: Energy loss ΔE_{Al} (circles), ΔE_{ta} (triangles) and ΔE (squares) versus the charged multiplicity N_{pres}. Monte Carlo simulation. Shown for 50 GeV jets, 10 cm aluminum absorber and 0.03 λ thick target.
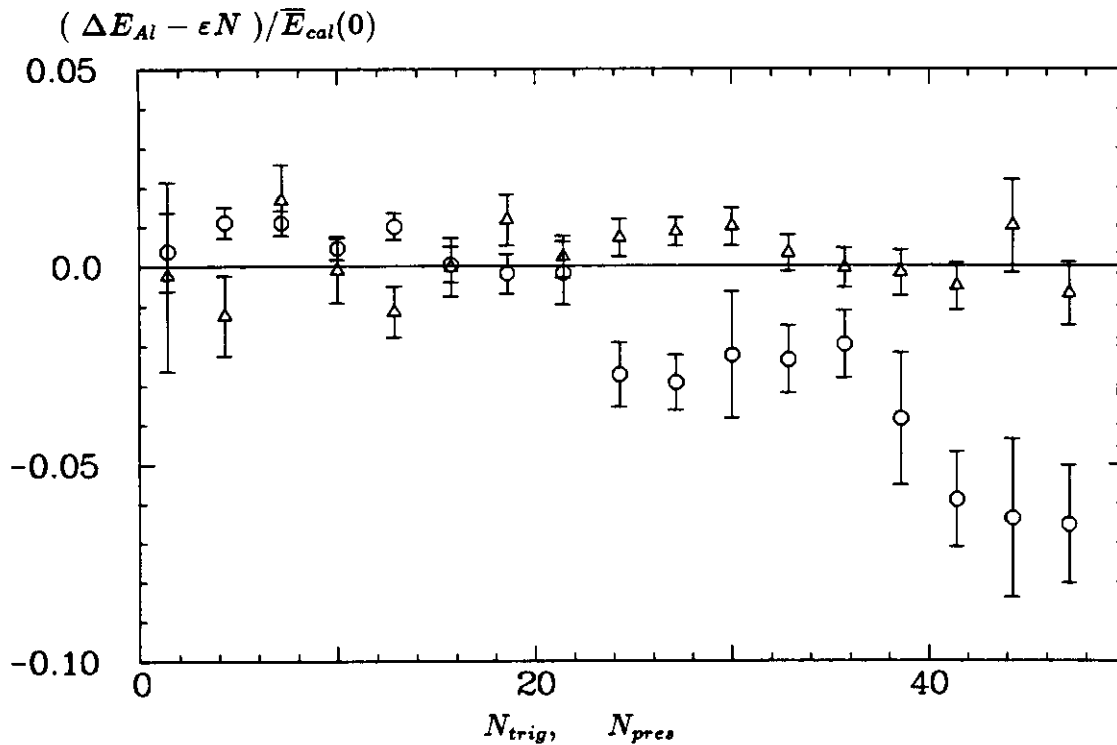
Figure 4.19: Energy difference between the energy loss in the the aluminum absorber ΔE_{Al} and the energy loss calculated by the energy correction ϵN. The correlation is shown for $N = N_{trig}$ (circles) and for $N = N_{pres}$ (triangle).

The difference $\Delta E_{Al} - \epsilon N$ for the correction with the presampler is in good agreement with 0. At large multiplicities $N_{pres} > 40$ the difference gets negative because the energy loss in the absorber is not described by a linear function. However, less than 5 % of the events are found within this region. For higher beam energies the curves are similar, but the deviation from the zero line starts at higher multiplicities.

The difference $\Delta E_{Al} - \epsilon N$ for the correction with the trigger counter shows deviations from zero. In particular for $N_{trig} > 20$ large deviations are observed. The deviations for $N_{trig} > 20$ are due to the fact that the energy loss in the aluminum absorber is almost independent of the measured charged multiplicity N_{trig}. In this region the linear behavior is not an adequate description. However only a few per cent of the events are within this region.

The effect of the energy corrections on the energy resolution is shown in fig.4.20. It is apparent that the correction with the presampler improves the resolution more than the correction with the trigger counter. The biggest improvement of the resolution is achieved if both charged multiplicities (N_{trig}, N_{pres}) were used for the correction. However the difference between the correction with N_{pres} and N_{trig}, N_{pres} is small. These results are similar to the ones obtained from the experiment. A difference between the simulation and the experiment is found in the strength of the improvement of the energy resolution. The improvement is bigger for the experimental data than for the simulation. The reason for this difference is that the energy resolution for jets with an absorber in front of the calorimeter is not correctly simulated, as has been shown in fig.4.14.
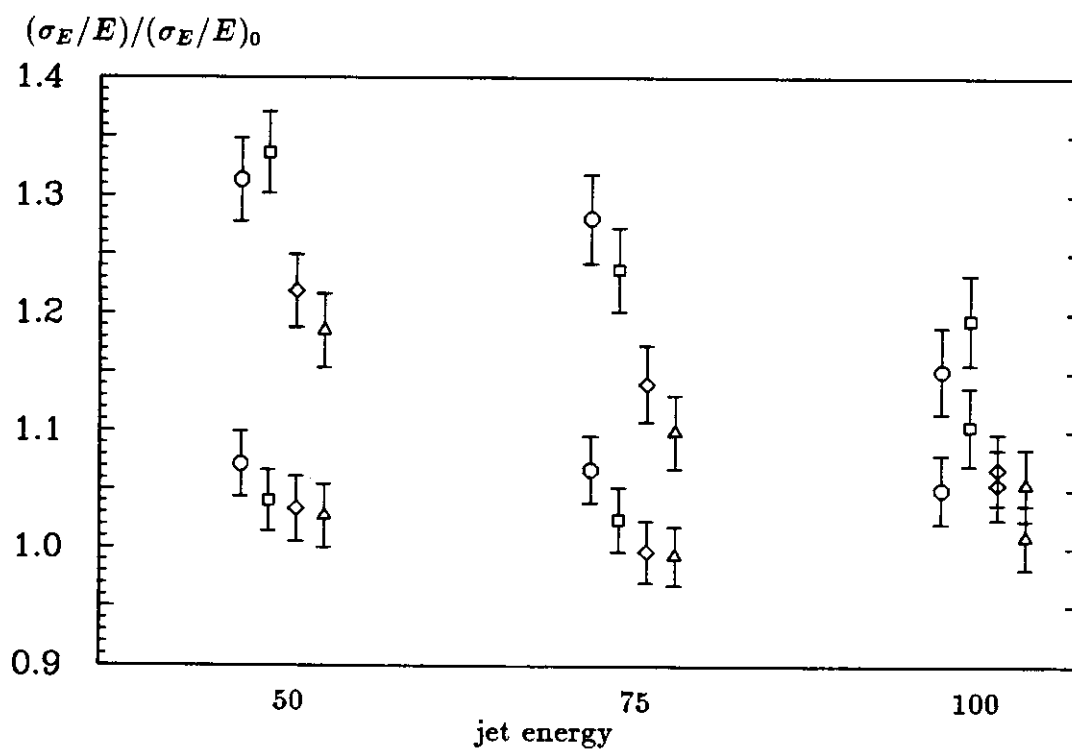
Figure 4.20: Resolution σ_E/E, normalized by the resolution $(\sigma_E/E)_0$ without an aluminum absorber, for different correction methods: No correction (circles), by N_{trig} (squares), by N_{pre} (diamonds) and by both counters (triangle). The lower (higher) values are for 4 (10) cm aluminum plates.

Chapter 5

Summary

The response of the ZEUS prototype calorimeter to jets was measured for 50, 75 and 100 GeV jet energies. Jets were created by inelastic pion interactions in a Be target with an interaction trigger. The target was surrounded by different counters in order to select interaction from non interaction and to measure particles which leave the target under large angles.

The calorimeter response of jets and single pions was compared. The jet signal is smaller than the pion signal.

	50 GeV	75 GeV	100 GeV	stat. error
Energy difference:	2.6 %	2.0 %	0.7%	±0.2 %

It was found that the energy resolution for jets is comparable or even better than the one for single hadrons.

The influence of a 4 cm and a 10 cm thick aluminum absorber in front of the calorimeter was measured for jets. The relative difference $(E(d) - E(0))/E(0)$ between the mean calorimeter energy with and without an absorber is for the 3 jet energies:

	50 GeV	75 GeV	100 GeV	stat. error
4 cm Al:	-2.3 %	-1.6 %	-1.3%	±0.1 %
10 cm Al:	-5.0 %	-4.4 %	-3.6%	±0.1 %

The energy resolution with an absorber in front is larger compared to the one with no aluminum absorber. The relative increase of the relative energy resolution is:

	50 GeV	75 GeV	100 GeV	stat. error
4 cm Al:	5.7 %	3.5 %	4.5 %	±1 %
10 cm Al:	20.0 %	12.0 %	14.0 %	±1 %

The energy loss in the aluminum absorber was corrected using the charged multiplicity measured in front and behind the absorber. For the correction function a linear dependence on the charged multiplicity was assumed. The correction parameter was determined so that the mean energy after the correction is equal to the mean energy without aluminum. The results are:

- Correction with the charged multiplicity in front of aluminum improves the resolution only slightly, by a few percent.

- Correction with the charged multiplicity behind the aluminum improves the resolution significantly. After the correction the resolution is close to the resolution without aluminum absorber. For lower jet energies (50 GeV) this improvement is not as good as for high energies (75 GeV , 100 GeV).

- The improvement of the energy resolution if both charged multiplicities in front and behind the aluminum absorber were used is comparable with the improvement if only the the charged multiplicity behind the absorber is used for the correction.

The series of experiments were simulated by a Monte Carlo calculation. The ZEUS trigger Monte Carlo T2 was used to simulate the calorimeter response. There are small discrepancies between the experimental results and the Monte Carlo results. The difference between the mean calorimeter signal for the simulation and experiment is less than 1.5 %. A larger relative difference is observed for the energy resolution which is up to 10 %.

Bibliography

[1] Andresen, A. et al.; Construction and beam test of the ZEUS forward and rear calorimeter, Nucl. Instr. and Meth. **A309** 101(1991)

[2] Andresen, A. et al.; Response of a uranium scintillator calorimeter to electrons, pions and protons in the momentum range 0.5 - 10 GeV/c, Nucl. Instr. and Meth. **A290** 95(1990)

[3] Behrens, U. et al.; Test of the ZEUS forward calorimeter prototype, Nucl. Instr. and Meth. **A289** 115(1990)

[4] Bentvelsen, S. et al.; Reconstruction of (x, Q^2) and extraction of structure function in neutral current scattering at HERA, in Proceedings of the HERA Workshop Vol.1, DESY 1991

[5] Bijnens, J.; Leptoquarks and Leptogluons at HERA, in Proceedings of the HERA Workshop Vol.1, DESY 1987

[6] Review of Particle Properties, Phys.Let.B **204** (1988)

[7] Bernstein, A., Caldwell A.; Beam study of calorimeter electronics, ZEUS-note (1988) 88-048

Caldwell, A. et al.; Test of calorimeter electronics and other results obtained at the CERN PS, ZEUS-note (1989) 89-045

[8] Feltesse, J.; Measurment of inclusive differential cross sections, in Proceedings of the HERA Workshop Vol.1, DESY 1987

[9] Fesefeldt, H.; The simulation of hadronic showers: physics and applications, Aachen (1985), PITHA-82/02

[10] Furtjes, A.; Verhalten des ZEUS Uran-Szintillator

Kalorimeters für niederenergetische Teilchen mit Energien von 0.2 - 10.0 GeV, Diploma thesis, University of Hamburg, internal report (1990) DESY-F35-90-02

[11] GEANT3 manual, (1987) CERN DD/EE/84-1

[12] Hartner, G.F.; Iga, Y.; ZEUS trigger MC Program status, internal report (1990) DESY F35-90-084

[13] Hartner, G.F.; Monte Carlo Shower Terminators for ZEUS inside GEANT311, internal report (1988) DESY F35-88-049

[14] HERA Proposal; DESY HERA 81-10 (1981)

[15] HERA Workshop; Proceeding of the HERA Workshop, Vol1+2; DESY, Hamburg 1987

[16] HERA Workshop; Proceeding of the HERA Workshop, Vol1-3; DESY, Hamburg 1991

[17] Klein, M.; On the Q^2, x range at HERA, in Proceedings of the HERA Workshop Vol.1, DESY 1991

[18] Krüger, J.; The uranium scintillator calorimeter for the ZEUS detector at the electron proton collider HERA, internal report (1992) DESY F35-92-02

[19] Ruckl, R.; Physics at HERA; DESY report 87-021 (1987)

[20] Straver, j.; Design, Construction and beam tests of the high resolution uranium scintillator calorimeter for ZEUS, Ph.D. thesis, NIKHEF, Amsterdam, Ph.D. Thesis, 1991

[21] Wigmans, R.; Proc. ICFA School on Instrumentation in Elementary Particle Physics, Trieste 1987, eds. C.W. Fabjan and J.E. Pilcher, Singapore: World Scientific

[22] Wiik, B.H.; HERA status, in Proceedings of the HERA Workshop Vol.1, DESY 1991

[23] ZEUS Collaboration; Status Report DESY-Hamburg (1989)
     ZEUS Collaboration; Status Report DESY-Hamburg (1987)

Acknowledgements